Electronic properties of single quantum dot junctions

Clemens Winkelmann

▶ **To cite this version:**

Clemens Winkelmann. Electronic properties of single quantum dot junctions. Mesoscopic Systems and Quantum Hall Effect [cond-mat.mes-hall]. Université Grenoble Alpes, 2018. tel-02099295

HAL Id: tel-02099295
https://theses.hal.science/tel-02099295

Submitted on 14 Apr 2019

HAL is a multi-disciplinary open access archive for the deposit and dissemination of scientific research documents, whether they are published or not. The documents may come from teaching and research institutions in France or abroad, or from public or private research centers.

L'archive ouverte pluridisciplinaire **HAL**, est destinée au dépôt et à la diffusion de documents scientifiques de niveau recherche, publiés ou non, émanant des établissements d'enseignement et de recherche français ou étrangers, des laboratoires publics ou privés.

UNIVERSITÉ DE GRENOBLE

Mémoire

D'HABILITATION À DIRIGER DES RECHERCHES

de l'**Ecole Doctorale de Physique de Grenoble**

Spécialité : **Physique / Nanophysique**

Clemens B. Winkelmann

Université Grenoble Alpes
& Institut Néel

Electronic properties of single quantum dot junctions

soutenu publiquement le **26 septembre 2018**, devant le jury composé de :

Julia Meyer
Professeure, Université Grenoble Alpes, Présidente
Elke Scheer
Professeure, Université de Constance, Rapporteure
Dimitri Roditchev
Professeur, ESPCI, Rapporteur
Frédéric Pierre
Directeur de Recherche, C2N/CNRS, Rapporteur
Thierry Ouisse
Professeur, Grenoble INP, Examinateur
Sergey Kubatkin
Professeur, Université de Chalmers, Examinateur

Introduction

This *Habilitation* thesis covers most of my research activities since 2008. Because my PhD thesis was on a rather unrelated subject (superfluid ^{3}He) to the physics described here, writing another manuscript about my last ten years' research turned out to be a satisfactory exercise, and definitely useful at least for myself. It is structured in three chapters, which summarize mostly published results along what I identified as three main axes, that is, (i) the physics of superconductor - quantum dot junctions, (ii) thermal effects in quantum nanoelectronic devices, and (iii) scanning probe microscopy studies at very low temperatures, - mostly on graphene. The first axis is a direct continuation of the work I began while a postdoc in the Nanospin team at Institut Néel, together with Nicolas Roch, Franck Balestro, Vincent Bouchiat and Wolfgang Wernsdorfer. The second axis is about thermal and more recently thermoelectric effects. This line derives from previous research interests of Hervé Courtois, with who I have been working together since my recruitment in 2008. From electronic cooling or overheating in quantum devices, we have recently moved to thermoelectric effects, a topic that is still little explored in quantum dot junctions. Finally, the interest in scanning probe microscopy techniques for investigating local quantum mesoscopic effects is a result of my first postdoctoral work at the University of Tokyo. Here too, Hervé Courtois and I found a fertile ground for collaborating on this shared interest.

While a postdoc with Wolfgang Wernsdorfer, my then-boss and I had a discussion one day about my professional future. His recommendation was, in essence: whatever subject you chose, what really matters is to have a vision, that is, an ultimate goal that all your efforts are in one way or the other converging to. Back in 2008, this goal was in Wolfgang Wernsdorfer's case measuring the reversal of a single quantum spin. Which he has achieved since.

Looking over the first three chapters of this manuscript, I have to recognize that I completely failed in following this advice. Indeed, both the instrumental techniques and the subjects presented here go into quite divergent directions. The situation is even worse when considering my PhD. To some extent, the main guideline of this work is probably the coupling between a single quantum level and the many-body effects induced by an electron reservoir. This can be probed by a variety of experimental tools, mostly related to tunneling spectroscopies in this case. The *tour de force* of the last (Prospective) chapter of this manuscript is to try to leave hope for a possible happy end in the form of a kind of convergence of topics and techniques.

I am deeply indebted to many people for the pleasure it has been to work at Institut Néel, in particular to my team-mate Hervé Courtois, but also to Vincent Bouchiat, Wolfgang Wernsdorfer, Nicolas Roch, Franck Balestro, Benjamin Sacépé, Johann Coraux, Denis Basko, Serge Florens, just to name a few colleagues in Grenoble. To these add many collaborators and friends from all around the world: Katharina Franke, Jukka Pekola, Anjan Gupta, Shaffique Adam, Claire Berger, ... Perhaps most importantly, I want to thank the students and postdocs, who really did the work presented here: Sylvain Martin, Sayanti Samaddar, David van Zanten, Aurélien Fay, Alessandro De Cecco, Bivas Dutta, Alvaro García Corral, Danial Majidi, David Wander, Efe Gümüs and Rini Ganguly.

*

Contents

Chapter 1

Superconductor - quantum dot junctions

The interplay of superconductivity with a quantum dot (QD) has generated a vast experimental and theoretical activity since the mid 90's. This chapter focusses on the device aspects of S-QD hybrids [1], rather than on the STM point of view discussed in a later chapter. From a fundamental perspective, one of the main interests of this topic is associated to the fact that superconductivity is a many-body effect best defined for an open system with a large number of particles and a well-defined phase, whereas the physics of QDs is dealing with the opposite limit. The above antagonism is readily visible from the commutation relation of the quantum phase and charge operators, $\left[\hat{Q}, \hat{\varphi}\right] = i\hbar$, and the ensuing Heisenberg relation between both quantities.

In a superconductor-quantum dot-superconductor (SQS) junction, the competing basic energy scales involved are the magnitude of the superconducting order parameter Δ, the temperature $k_B T$, the QD charging energy U, and the tunnel coupling energies γ_i to each lead i. Another effective energy scale, $k_B T_K$ associated to the Kondo effect, emerges in some cases from the above. A large physical variety of regimes is thus observed depending on the hierarchy of the above energy scales.

1.1 Electromigration and fabrication of single quantum dot devices

The devices described in this section were obtained by the electromigration technique [2, 3], a detailed description of which can be found in the theses of Nicolas Roch and David van Zanten [4,5]. A constriction, of section $\sim 15{\times}150$ nm^2, is lithographically prepared in a metallic wire, on top of a local backgate. Usually, the wire is covered with a suspension of the molecules or nanoparticles to be connected. By ramping up the bias voltage across the wire, the combination of local heating and momentum transfer between the electron flow and the ions can lead to the opening of a nanometer-wide crack in the wire, a well-known failure mechanism in conventional electronics. A fast reduction of the bias voltage as soon as the local resistance increases allows avoiding a thermal avalanche and creating such nano-cracks in a rather controlled fashion. The little miracle here is that, probably under the influence of local thermal activation, and perhaps of the local electric field, the molecules/nanoparticles have a tendency to "fall" into the crack, bridging thereby electrically the leads.

Just to get this straight: electromigration is an exploratory, poorly controlled, and low-yield fabrication technique for connecting QDs, with no direct mid-term applications in nanoelectronics.

After the successful implementation of single-molecule electromigration junctions between gold leads

in the Nanospin group at Néel by N. Roch, V. Bouchiat, W. Wernsdorfer and F. Balestro [6, 7], I extended Nicolas Roch's work to superconducting leads in 2007/08 while a postdoc. Because we were unsure wether electromigration could actually work in aluminum, we started with electromigration in short gold constrictions connected to nearby ($\sim$ 100 nm) bulkier Al leads, thereby inducing superconductivity by the proximity effect (an approach later also used in [8]). The results we obtained in such junctions can be summarized as follows: (i) electromigration works smoothly, as expected in gold, (ii) the tunnel coupling to the QDs (fullerenes at that time) is rather strong, (iii) the spectral gap in the proximity superconducting leads is smeared, and (iv) the gold-aluminum interface degradates quickly (due to the so-called *purple plague*, resulting from intermixing of both compounds), if not cooled down within less than 12 hours after fabrication.

In 2008, we moved to aluminum-only junctions. While the final number of successful devices is insufficient for establishing reliable statistics, the following device characteristics emerge: (i) electromigration is slightly more difficult, although still possible, (ii) the tunnel coupling to the QD is generically weaker, (iii) the leads' density of states (DOS) has a hard gap, and (iv) prior to electromigration samples can be stored for more than a week under ambient conditions before showing signs of degradation (mainly a gradual increase in resistance due to oxidation).

A few years later, in the PhD work of David van Zanten, we came back to electromigration devices, using this time colloidal gold nanoparticles rather than fullerenes [9]. David van Zanten came to the conclusion that both the nanoparticle size and the ligands play a crucial role in the device yield [5]. Eventually, most electronic transport features were very similar to the fullerene-based junctions from my postdoc.

More recently, Bivas Dutta started electromigration in noble metal constrictions in our group, for the studies described in section 4.2. Bivas has tried several approaches beyond the drop-casting technique. A few trials based on dielectrophoresis for trapping the nanoparticles from a suspension between the leads [10] were not conclusive, but would deserve to be deepened. Following an idea from D. Ralph's group [11], Bivas Dutta has eventually focussed on evaporating an extremely thin ($<$ 1.5 nm) gold layer on top of the constrictions (made of gold or platinum). The dewetting of the thin gold layer naturally produces nanoparticles. Clearly, the surface contaminants on the leads play a crucial role in this dewetting process. The gold nanoparticles can even be deposited before electromigration. The success rate of such junctions is strongly enhanced with respect to the drop-casted QDs. However, because of the large number of electrostatically floating nanoislands in the vicinity of the junction, the electrostatic environment is often subject to severe switches. Further, the QD spectroscopy does not yield as clearly resolved quantum levels as in colloidal or molecular QDs.

All these difficulties said, one might wonder why bother with this low-yield technique. The reason for this lies in a range of original features of the single-molecule or -nanoparticle based superconducting hybrids presented here, with respect to earlier and widely studied hybrids based on two-dimensional electron gases (2DEGs), carbon nanotubes (CNTs) or semiconducting nanowires, which are listed below:

- **A well separated hierarchy of energy scales.** The charging energy U exceeds usually several tens of meV. The orbital level spacing δE is easily resolved ($>$ 1 meV), larger than the superconducting gap of aluminum Δ, which is 180 μeV in the bulk and reaches frequently 250 μeV in nanostructured electrodes. This allows generally to reduce the QD to a single orbital quantum level. The tunnel coupling γ to gold nanoparticles in all aluminum devices is the smallest parameter, usually $\sim$ 1 μeV in the turnstile devices, but can be occasionally larger (see section 1.3.3).

- The quantum confining potential well is defined by the physical edge of the nanoparticle and thus very sharp and gate voltage insensitive. This is in strong contrast with the tunable but shallow tunneling barriers, prone to cross-talk, of many other QD devices.

- There is no interface material between the QD and the leads and the contact is point like. For comparison, in CNT-based or similar SQS junctions, an interface material is often used, which reduces

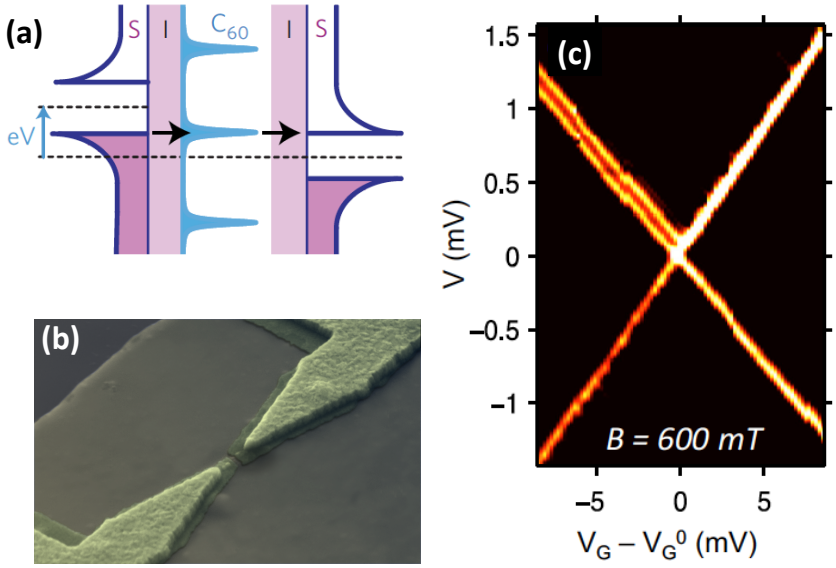

Figure 1.1: **(a)** Example of a transport diagram involving two tunnel junctions. The vertical axis allows for comparing the chemical potentials of the different elements (leads and QD). The horizontal axis represents the density of states. The respective band structures of both leads can be offset by applying a bias voltage V_b. μ^N_{QD} depends linearly on the gate voltage V_g. **(b)** SEM image of an all-aluminum electromigrated constriction on top of a local backgate. **(c)** $\partial I/\partial V$ differential conductance map of an asymmetric device in the normal state, near its sole experimentally accessible degeneracy point. The conductance ranges from about 0 (black) to 1.6 μS (bright) (T = 100 mK, B = 600 mT. Due to coupling asymmetry, the Zeeman splitting is visible only at a single Coulomb diamond edge (see text). The left Coulomb diamond corresponds to an *even* electron occupation number.

the gap magnitude and smears the gap edge [12]. This is particularly important for the discussion in section 4.1.1.

1.2 Normal state transport properties of quantum dot devices

Before presenting the effect of superconductivity in the leads for transport through a QD, this section briefly reviews a few normal state transport properties. Rather than presenting an extensive lecture on Coulomb blockade here, I will put forward a selection of N-Q-N transport properties that non-experts in the field might ignore. I recommend the very nice paper by E. Bonet *et al.* while at Cornell [13] for further details.

- The vertical axis in a transport diagram (such as in Fig. 1.1) represents the chemical potential, and not the energy. This is necessary because - as opposed to the case of optical spectroscopies in which electrons are promoted and not added - in a tunneling process the charge state (and thus the charging energy) of a QD is changing.

- The electron spin degree of freedom strongly affects the relative probabilities of tunneling in and out a quantum dot. Assume an empty spin-degenerate orbital level with symmetric tunnel coupling to both leads. For tunneling into the QD, both spin species in the lead can contribute. But once an electron is in the QD, its spin is fixed and thus it can only couple to a single spin-band in the other lead. Therefore tunneling out is the bottleneck here, even if the junction transparency is the same

to both sides. Consider now a spin-degenerate level occupied by one electron in its ground state, to which a second one is added. An analogue reasoning shows that now tunneling in is two times less likely than tunneling out.

- From this effect, one cannot determine the parity of the dot occupation number N from simple conductance measurements, because there is an ambiguity on what the tunnel couplings per spin channel are, within a factor 2. When several Coulomb diamonds are visible, the occupation number parity can be guessed from the shell superstructure of the Coulomb diamond pattern. When the coupling is a bit stronger, the parity of N can also be inferred from the observation of a Kondo resonance in oddly occupied Coulomb diamonds. Alternatively, parity can be determined from Zeeman splitting of the quantum dot levels under an applied magnetic field. If the edge of a Coulomb diamond with occupation number N splits, the first excitation (to state $N \pm 1$) is Zeeman split, thus $N \pm 1$ is odd and N is even.

- If under magnetic field only one edge of a given Coulomb diamond splits, while the edge at opposite bias voltage doesn't (as shown in Fig. 1.1), this is due to asymmetric tunnel coupling. Consider highly asymmetric tunnel couplings to the leads and a Zeeman-split orbital level. When the orbital level is lowered towards the Fermi level of the strongly coupled lead, having a single or both spin levels accessible hardly affects the current because the bottleneck is on the other side. The opposite is true when the orbital level approaches the Fermi level of the weakly coupled lead: the current increases in two approximately equal steps.

1.3 Electron transport in SQS devices

1.3.1 The Anderson impurity model

The most widely used starting point for describing an atomic impurity (a single quantum level) in a superconducting host is the Anderson impurity model [14–16], with Hamiltonian $H = H_{\rm QD} + H_{\rm mix} + H_{\rm SC}$. The QD energy

$$H_{\rm QD} = \sum_{\sigma} \epsilon_{\rm QD}\, n_\sigma + U\, n_\uparrow n_\downarrow$$

depends on the (spin σ dependent) occupation $n = d^\dagger d$ of the level, at a bare energy $\epsilon_{\rm QD}$ with respect to E_F.

The Coulomb energy U makes double occupation unfavorable. Further, the coupling energy

$$H_{\rm mix} = \sum_{\sigma,\mathbf{k}} t\, c^\dagger_{\sigma,\mathbf{k}} d_\sigma + h.c.$$

describes tunneling between the QD $(d, d^\dagger)$ and the host $(c, c^\dagger)$. From the tunneling amplitude t and the host's normal density of states ρ_n, one defines the tunnel coupling (hybridization) $\gamma = \pi t^2 \rho_n$.

Finally, the superconducting host (or the lead connecting to the QD) is described by

$$H_{\rm SC} = \sum_{\sigma,\mathbf{k}} \epsilon_{\mathbf{k}}\, c^\dagger_{\sigma,\mathbf{k}} c_\sigma - \sum_{\mathbf{k}} \left(\Delta\, c^\dagger_{\uparrow,\mathbf{k}} c^\dagger_{\downarrow,-\mathbf{k}} + h.c. \right).$$

Δ is the complex superconducting order parameter in the host/lead. It can be replaced by $|\Delta|$ if both the tunneling amplitude t and the creation operators in that lead are multiplied by $e^{i\varphi/2}$, with φ the phase of Δ. In the remainder, we identify Δ and its magnitude. In $H_{\rm SC}$, destroying two electrons with opposite spin and momentum to form a Cooper pair lowers the energy by Δ per electron. In the case of two superconducting leads connected to the QD, both $H_{\rm mix}$ and $H_{\rm SC}$ will be doubled, with respective indices L, R.

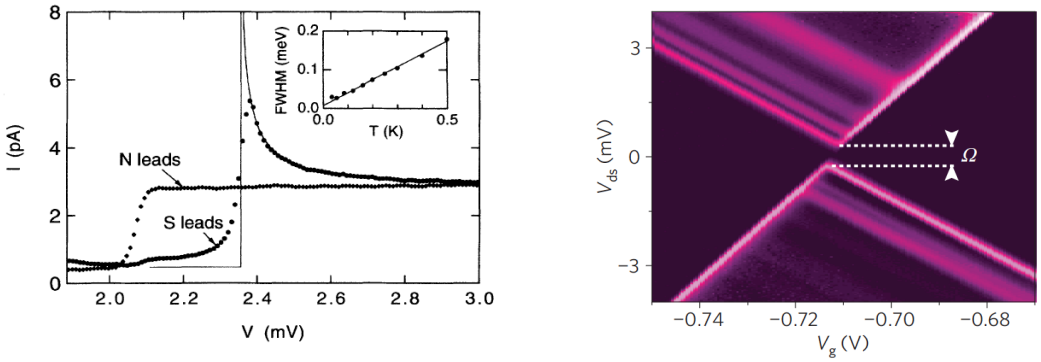

Figure 1.2: **SQS junction the weak-coupling regime. Left:** $I(V_b)$ at a fixed gate in the normal and superconducting states, respectively [17]. The current reproduces the shape of one lead's superconducting density of states; the conductance onset is shifted in voltage by $2\Delta/e$ in the superconducting state. **Right:** differential conductance map of a single molecular SQS junction, displaying sharply resolved spectroscopy of the QD states and a transport gap $\Omega = 4\Delta/e$ around E_F [18].

There are numerous competing energy scales in the above problem. The above Hamiltonian is thus extremely rich, but analytical solutions are only available in some limiting cases. One such special case is the non-interacting situation $U = 0$, for which the spectrum and the current can be calculated exactly. However, the situation of small U is rather marginal in the experiments that will be presented here. We will go through the various situations described by the Anderson impurity model from an experimental point of view, sorted by increasing coupling strength.

1.3.2 Weak coupling regime: sequential and co-tunneling

Early experiments

The first experiments in the weak-coupling regime, $\gamma_{\mathrm{L,R}} \ll \Delta, U$, in which a QD was connected to superconducting leads were performed by D. Ralph in Tinkham's group [17]. Their devices have a vertical geometry and take advantage of both superconducting and tunneling oxide properties of aluminum. The QD itself is also a self-assembled aluminum grain, too small to be superconducting itself (in a later paper this is no longer true [19]). This pioneering SQS transport experiment agrees nicely with the sequential tunneling picture, that is, in the limit of vanishing tunnel coupling. Here, tunneling is described by Fermi's golden rule and the current is given by

$$I(V_b) \propto \int dE\, \rho_L(E)\, \rho_R(E + eV_b)\, \delta(E - \mu^N_{\mathrm{QD}})\, f_L(E)\, (1 - f_R(E + eV_b)),$$

where μ^N_{QD} is a linear function of both V_b and V_g, f is the filling factor and

$$\rho_{\mathrm{L,R}}(E) = \mathcal{R}e\left(\frac{|E|}{\sqrt{\Delta^2 - E^2}}\right) \tag{1.3.1}$$

is the normalized superconducting density of states in the respective lead. From the properties of the δ function, the above expression of the current reduces to

$$|I(V_b)| \propto \rho_L(\mu^N_{\mathrm{QD}})\, \rho_R(\mu^N_{\mathrm{QD}} + eV_b).$$

When μ^N_{QD} is deep inside one band of one lead, the current around the conductance onset is proportional to the density of states in the other lead. This is opposed to usual, single-barrier tunneling experiments, where the differential conductance and not the current is proportional to the density of states. Further, the

conductance onset is shifted to voltages $2\Delta/e$ greater in absolute values with respect to the normal state. All these features are well seen in Fig. 1.2.

One interesting use of superconducting tunneling contacts resides in the fact that this allows overcoming the thermal Fermi edge smearing, unavoidably associated to tunneling from normal leads. In the latter case, tunneling spectroscopies present a full-width at half maximum (FWHM) $\sim 3.5\,k_BT$. This long-known improvement of tunneling spectroscopy resolution by the use of a superconducting probe [20] has been extensively used in STS [21–23] and device physics [24] recently. However, a deconvolution procedure has to be applied to recover the spectral features from the differential conductance measurements, roughly leading to an energy shift by $\pm\Delta$. For example, in the sample shown in Fig. 1.5, we obtain by this method a FWHM resolution of the sub-gap states better than 8 μeV, way below the thermal smearing in normal probes, even at dilution temperatures.

Hybridization

In the work of Ralph and coworkers [17], the sequential tunneling picture does actually not quantitatively hold because the tunnel coupling, at least to one lead, is not much smaller than Δ. The signatures of hybridization of a quantum level coupled to superconducting leads were discussed in more detail in two later theory papers [25,26]. In a NQN junction, hybridization leads to the Wigner-Weisskopf expression of the QD spectral function, which manifests experimentally (at $T = 0$) as a lorentzian differential conductance at the tunneling energy threshold. In a SQS junction, the non-trivial density of states in the lead can be translated into an effective tunnel coupling, which itself depends on the relative position of the bare QD energy level $\epsilon_{\rm QD}$ with respect to the lead's chemical potential, namely $\tilde{\gamma}(\epsilon_{\rm QD}) = \gamma\,\rho(\epsilon_{\rm QD})$, with ρ the single-particle DOS in S. At large energies, $\tilde{\gamma} \approx \gamma$ and the Wigner-Weisskopf expression is recovered. On the other hand, for $\epsilon_{\rm QD} < \Delta$ the renormalized coupling strength $\tilde{\gamma}$ drops brutally to zero. A Green's function based perturbative calculation yields the hybridized QD spectral function $A(E, \epsilon_{\rm QD})$, which is, within a proportionality factor, given by the imaginary part of the retarded Green's function

$$G(E) = \frac{1}{E - \epsilon_{\rm QD} - \Sigma(E)}, \tag{1.3.2}$$

where

$$\Sigma(E) = -\gamma\frac{|E|}{\sqrt{\Delta^2 - E^2}}$$

is the self-energy of the S-Q hybrid. Note that the self-energy and the effective tunnel coupling defined above are related via $\tilde{\gamma} = -\mathcal{R}e(\Sigma)$. For a full SQS junction, the self-energies of the QD-lead coupling on each side must be simply added.

Green's function's poles

The Green's function defined in Eq. (1.3.2) can have either one or two poles, depending on the bare level position $\epsilon_{\rm QD}$ with respect to the gap edge Δ [27]. For simplicity and without loss of generality, we restrict the discussion to positive energies with respect to the lead's Fermi energy. We also introduce a new energy scale $\beta = (\gamma^2\Delta/4)^{1/3}$, with $\gamma < \beta \ll \Delta$ in weakly coupled devices. When the bare QD level is well below the gap edge ($\epsilon_{\rm QD} < \Delta - \beta$), there is a single pole, E_1, which is real valued and very close to $\epsilon_{\rm QD}$. In other words, the QD level is not affected by the states above the gap and its lifetime remains infinite.

In the opposite case ($\epsilon_{\rm QD} > \Delta - \beta$), a second, complex-valued, pole E_2 emerges. For large bare dot levels, $\epsilon_{\rm QD} \to +\infty$, the real and imaginary parts of E_2 can be identified with $\epsilon_{\rm QD}$ and γ, respectively. In other words, when the QD level is far above the gap edge, the Wigner-Weisskopf expression is recovered and the hybridized level can be described as a dressed state with no shift and a lifetime $\hbar/\gamma$. On the other hand, the first pole E_1 remains real valued for all $\epsilon_{\rm QD}$ and increases asymptotically towards the gap edge Δ

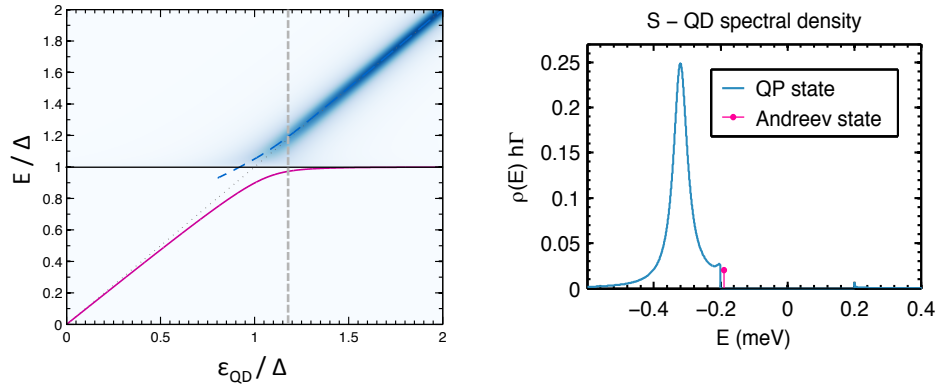

Figure 1.3: **Left:** color map (calculation) of the spectral density of the S-Q hybrid for $\gamma = 0.04\,\Delta$, as a function of $\epsilon_{\rm QD} \propto V_g$. The magenta line shows the infinite life-time subgap state at energy E_1. The blue region corresponds to the complex pole E_2, that is, the QD level dressed by the coupling to the lead. **Right:** line cut through the left map along the grey dashed line. Data from [5].

for large $\epsilon_{\rm QD}$, while always remaining below. This discrete sub-gap state would be tending to the gap edge exponentially if the leads density of states was a step function. However, because of the DOS divergence at the gap edge, level repulsion is very effective and one finds for large $\epsilon_{\rm QD}$

$$E_1 \;\approx\; \Delta - 2\,\frac{\beta^3}{(\epsilon_{\rm QD}-\Delta)^2}. \tag{1.3.3}$$

For completeness, let us also mention the spectral weight of both poles. For $\epsilon_{\rm QD} < \Delta - \beta$, all the spectral weight is obviously in the sub-gap state. As $\epsilon_{\rm QD}$ is cranked up, more and more spectral weight is transferred to the dressed state and the sub-gap state weight Z decreases quickly, $Z \sim [\beta/(\epsilon_{\rm QD}-\Delta)]^3$.

Dynes broadening

The above calculation assumes a BCS-type DOS in the leads, implying infinite Cooper-pair lifetimes. Deviations from this ideal picture are known to be small in superconducting aluminum and are usually described in a more or less phenomenological way by adding an imaginary part to the energy ($E \to E + i\vartheta$) in the BCS DOS in Eq. (1.3.1), called the Dynes parameter. Whether E_1 can still be considered as a separate spectral entity depends therefore on the relative values of ϑ and $\Delta - E_1$. While the intrinsic Cooper-pair lifetime in aluminum is very large ($\vartheta/\Delta < 10^{-7}$), radiation noise from higher temperatures can lead to the same signatures and must thus be shielded carefully [28]. In the literature, the Dynes parameter is sometimes misused as a "fudge-factor", allowing to fit data displaying sub-gap leakage in superconducting tunnel junctions, which should be rather attributed to junction imperfections, such as pin-holes.

1.3.3 Superconductivity versus Kondo effect

Kondo effect

In the (conventional) superconducting ground state, electrons pair up into singlet spin states. Another many-body effect in which electrons form a singlet spin state is the spin-$^1/_2$ Kondo effect, in which a magnetic impurity is screened by the conduction electrons of a metallic host material. Generally speaking, the Kondo effect is a many-body effect resulting from the coupling of a Fermi sea to a degenerate impurity level. In the simplest case, the degeneracy is provided by a spin-$^1/_2$ Kramers doublet, but more exotic degeneracies can exist ($S = 1$, orbital, charge,...) [6, 29, 30]. In the former case, odd electron occupation

of the impurity or QD is a prerequisite for observing the Kondo effect [31, 32]. Electrons in the Fermi sea exchange with the local impurity spin, leading to rapid impurity spin flips. These spin flips tend to cancel/screen the local impurity spin, rendering the system effectively non-magnetic at low energies. The energy gain obtained by the quantum coherent system formed by the impurity and its cloud is $k_B T_K$, giving rise to a novel spectral resonance pinned to the Fermi level of the reservoir (and not to the impurity level), of width $k_B T_K$. The strength of the Kondo effect rapidly increases with tunnel coupling (see [4, 15, 33] and references therein), following

$$T_K = \sqrt{\gamma U}\, \exp\left(-\frac{\pi U}{8\gamma}\left(1 - 4\frac{\epsilon_{\mathrm{QD}}^2}{U^2}\right)\right), \tag{1.3.4}$$

with $\gamma = \gamma_L + \gamma_R$. The effect of any perturbation W (such as temperature, noise or Zeeman splitting of the Kramer's doublet) to the above situation is, to a large extent, universal and depends solely on the ratio W/T_K. True universality relies however on some assumptions, like e.g. $U \gg \gamma$.

In asymmetric NQN junctions, the Kondo resonance develops first between the dot and the lead with stronger coupling. For $T_K^{\mathrm{strong}} > T > T_K^{\mathrm{weak}}$, the other lead can be considered as a non-invasive tunnel probe and differential conductance measurements directly map the Kondo resonance on the strongly coupled side.

In case of symmetric couplings, the Kondo cloud extends over both electrodes. In this case, the linear conductance is $G_0 = 2e^2/h$ at low enough temperature. The effect of a bias voltage is then to lift the degeneracy of both reservoirs' Fermi levels, suppressing coherent tunneling between the leads. The experimental signature is still a zero-bias peak in the differential conductance, but its quantitative interpretation is way more involved than in the strongly asymmetric case, and calls for an out-of-equilibrium modeling of the Kondo problem. The FWHM of the zero-bias conductance resonance can still be related to T_K, via a constant ranging from 2.8 to 4 depending on the models and definitions of T_K [34]. In case of weak coupling asymmetry to the leads, Kondo correlations will gradually set in on both leads as temperature is reduced, which is called the *two-stage* Kondo effect.

In both cases (symmetric and asymmetric), a much more quantitative estimation of T_K is obtained by measuring the linear conductance as a function of temperature. The behavior of $G(T/T_K)$ has a universal form and can be calculated using numerical renormalization group (NRG) methods. For practical uses, it is convenient to use a phenomenological fitting function [31], which we also use here. A fit of the normal state linear conductance of a device obtained by Alvaro Garcia Corral to this equation is shown in Fig. 1.5. Eventually, T_K can also be accessed by applying a magnetic field. The Kondo resonance is stable against a magnetic perturbation until $\mu_B B \sim k_B T_K$, meaning that the Zeeman splitting is small enough not to lift the spin degeneracy. Above this critical field B_c, the Kondo zero bias conduction resonance breaks up into two smaller peaks, shifting symmetrically and linearly from the Fermi level with $B - B_c$ (Fig. 1.4d). A T_K larger than a few Kelvin is difficult to determine precisely from both above methods because high temperature measurements are often unstable and large magnetic fields would be needed.

Kondo effect versus superconductivity

An interesting situation arises from the competition of Kondo physics with the superconducting correlations provided by the leads. Because of the single particle excitation gap in the lead DOS, tunneling from and to the Kondo resonance at E_F has an energy cost Δ. Consequently, one can expect the suppression of the Kondo effect depending on the hierarchy of T_K and Δ. The survival of Kondo correlations when $T_K > \Delta$ was experimentally first verified by Buitelaar *et al.* [12] in superconducting CNT junctions.

The following canonical base will be used in the remainder to describe the QD state: (i) the empty QD, $|0\rangle$, (ii) the singly occupied QD, that is, in a spin doublet state $s = 1/2$, corresponding to $|\uparrow\rangle$ or $|\downarrow\rangle$, and (iii) the doubly occupied singlet state, which we write $|\uparrow\downarrow\rangle$. Both $|0\rangle$ and $|\uparrow\downarrow\rangle$ are spin singlet states, thus any linear combination of both is also $s = 0$.

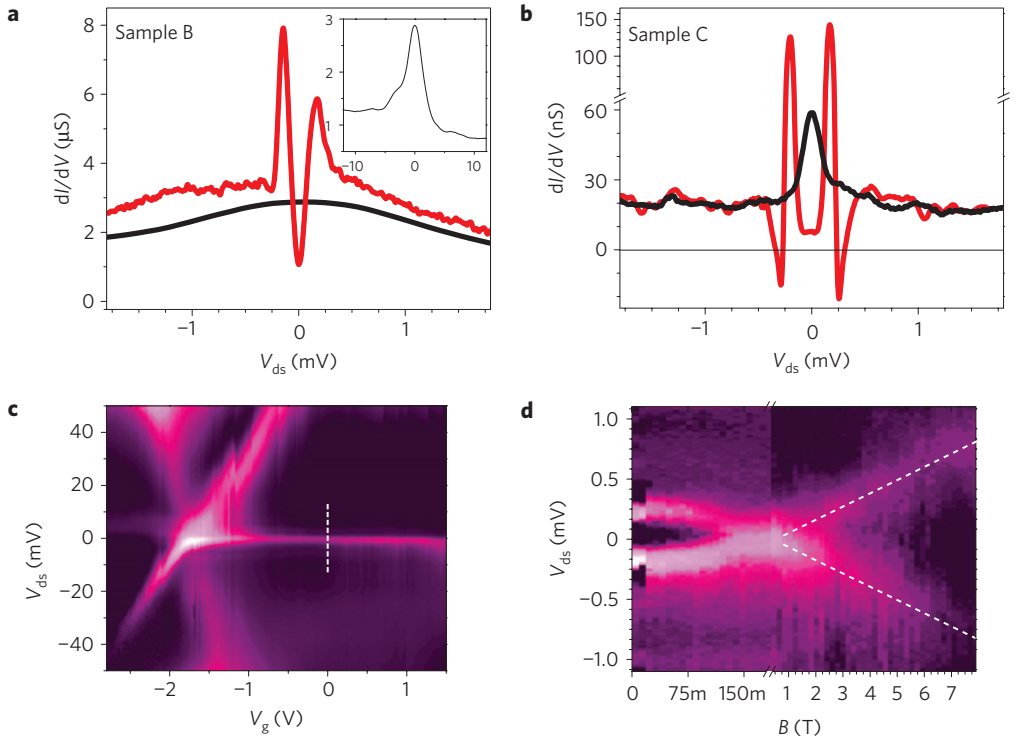

Figure 1.4: **a** and **b**, $\partial I/\partial V$ as a function of V_b at constant gate in two samples ($T < 40$ mK) and in both the normal (black line) and the superconducting state (red line). **a**, Sample B has $T_K = 14$ K, and superconductivity superimposes on top of the Kondo resonance. The inset shows the normal state data over a larger bias voltage window. **b**, Sample C has $T_K = 0.7$ K, and the onset of superconductivity suppresses the Kondo resonance. Above 65 nS, the vertical scale is logarithmic. **c**, $\partial I/\partial V$ map of sample B in the normal state ($T = 40$ mK, $B = 400$ mT). The plots shown in **a** are taken along the dotted line (the color code can be read from the vertical scale in **a**). **d**, Magnetic field dependence of the low energy $\partial I/\partial V$ in sample C. At about 130 mT, the coherence peaks merge into the Kondo resonance which is further Zeeman split above $B_c \approx 0.4$ T. The dotted lines are fits to the Zeeman splitting (see text). For better contrast, the $\partial I/\partial V$ color code is different in the low and high field regions. Data from [18].

For $T_K < \Delta$, the local impurity spin can no longer be screened and the dot ground state is $s = 1/2$. In the opposite case, a Cooper pair is broken in order to form a singlet state at the impurity site and the ground state is a superposition of $|0\rangle$ and $|\uparrow\downarrow\rangle$, that is, $s = 0$. Both above states exist in both regimes of T_K versus Δ, being either the ground state (GS) or the first localised excited state (LES), also called Andreev bound state (ABS), with energy $0 \leq E_b < \Delta$. Notably, the GS→LES transition changes the QD fermionic parity, meaning that a single electron has been added or removed through a tunnelling process (coming for example from a second, weakly coupled, lead). Because both the Kondo effect and superconductivity are many-body problems, the ground state transition characterized by $E_b = 0$ and occurring near $T_K \sim \Delta$ is frequently referred to as a *quantum phase transition* (QPT) in the literature [14, 23, 34].

The above problem, described in the frame of the Anderson impurity model, has no general analytical solution. However, a few interesting limiting cases emerge:

- **Small U limit.** In the non-interacting limit, double dot occupancy is allowed and superconducting correlations on the impurity site are strongly favored. In this case, the Andreev bound states correspond to a spin doublet on the QD, with an energy that can be analytically calculated (Eq. (7) in [15]). Notably, for any ABS energy E_b, the formalism also yields a state of equal weight at $-E_b$. This is a consequence of particle-hole symmetry, which is intrinsic to superconductivity and

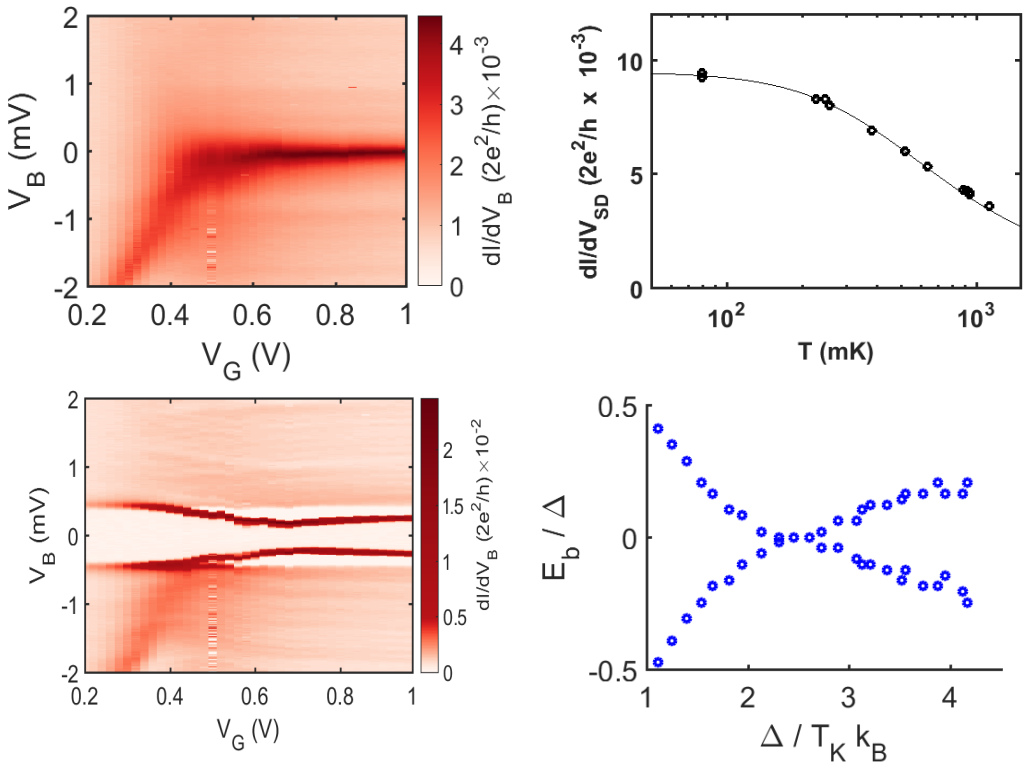

Figure 1.5: Unpublished data by Alvaro García Corral in the regime of strong coupling asymmetry, and Kondo correlations developing on one lead. **Left side maps:** differential conductance maps near a charge degeneracy point in the normal and superconducting state, respectively. The right half of both maps corresponds to an odd electron occupation number, leading to a Kondo ridge in the normal state and ϵ_{QD}-dependent subgap states ($T = 70$ mK; $B = 60$ and 0 mT, respectively). **Top right:** temperature dependence of the linear conductance in the Kondo regime ($B = 60$ mT, $V_g = 0.72$ V). The line is a fit ([31], see text) yielding $T_K = 0.7$ K at this gate voltage. **Bottom right:** bound state energies E_b as a function of $\Delta/k_B T_K$, revealing the screened-unscreened QPT at a critical value ≈ 2.4.

also preserved here because $U = 0$. The negative energy solution should be understood as the process of removing an electron, starting from GS, as opposed to the process at $+E_b$, which corresponds to adding an electron.

- **Large gap limit.** The second analytically solvable limiting case is that of $\Delta \to +\infty$. The Hamiltonian can then be considerably simplified and one finds that (i) the doublet states are eigenstates of zero energy, (ii) neither the empty site $|0\rangle$ nor the doubly occupied $|\uparrow\downarrow\rangle$ state are eigenstates; however one can construct Bogolyubov-like linear combinations of the latter, one of which being an eigenstate with negative energy, provided that $(\epsilon_{\mathrm{QD}} + U/2)^2 + \gamma^2 < (U/2)^2$ [15]. In this case the GS is therefore a singlet state and the impurity spin is screened. The singlet-doublet phase boundary is then given by the semi-circle represented in Fig. 1.7.

The finite-Δ case calls for numerical renormalization group (NRG) calculations, but the outcome is qualitatively similar to the above situation. As seen in Fig. 1.7, the phase boundary for the singlet and doublet GS occurs now at slightly smaller tunnel coupling strengths.

Experimental signatures of the screened-unscreened spin impurity quantum phase transition

The screened-unscreened ground state crossover (or QPT, depending on the authors) was first observed via supercurrent measurements [35, 36], which we will come back to below. The first controlled spectroscopic

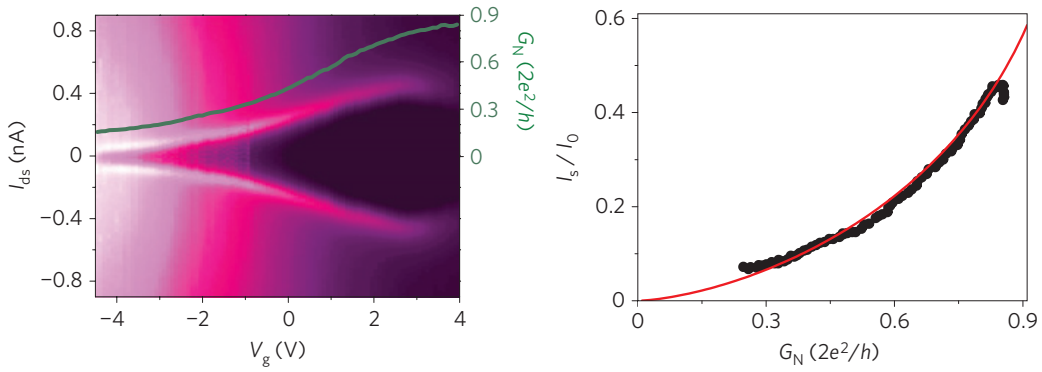

Figure 1.6: **(a)** Differential *resistance* map in the superconducting state (B = 0 T) for small bias currents modulated by $I_{mod} = 18\,\text{pA}$ at $f_0 = 86\,\text{Hz}$. The green line is the zero bias conductance in the normal state. **(b)**, Switching current I_s normalized to $I_0 = 1.01\,\text{nA}$ as a function of normal state conductance (bullets), and fit to equation (2) (line). The only adjustable parameter is I_0. The data points deviating from the fit at high conductance correspond to measurements taken at $V_g \approx 4$ V, where a significant tunnel leakage current from the gate electrode contaminated the measurements. Data from [18].

evidence of the QPT was obtained by transport experiments in Tokyo [37], on an InAs QD strongly coupled to a superconducting lead and weakly coupled to a normal tunnel probe. Here, the ground state transition is tuned by adjusting ϵ_{QD}, and thus T_K, via a gate electrode. In subsequent STM experiments on magnetic molecules [23] these results were better resolved, owing to a superconducting tip as a tunnel probe. Although there was no control of ϵ_{QD}, this study found variations in the tunnel coupling strength of the molecules, depending on the adsorption site on Pb(111). In situ measurements of T_K on the same molecules at higher temperature allowed to track the variations of E_b with T_K/Δ, across the phase boundary.

During my postdoctoral work in the Nanospin group, I obtained several single molecule SQS junctions which also displayed Kondo correlations. Fig. 1.4 shows transport properties of two devices, which illustrate both GS situations, depending on the hierarchy between T_K and Δ [18]. Recently, Alvaro García Corral has obtained several strongly asymmetric SQS junctions, in which one contact acts as a probe of the bound states formed by the coupling of the QD to the other lead. Here, we also measure T_K and E_B independently on a single quantum dot and tune the QPT by the gate voltage (Fig. 1.5). An interesting difference with the STM experiments in Berlin is related to the rather high temperatures (> 1 K) of the STM, leading to dominantly thermally activated tunneling spectroscopies [38], whereas in our experiments the tunneling processes exclusively involve Andreev reflection.

1.3.4 Josephson coupling

In the *strong-coupling regime*, where Γ is the largest energy scale, higher-order tunneling processes can bypass the Coulomb blockade effect and Cooper pairs can be coherently and resonantly transferred across a SQS device [39, 40]. In experiments, the maximum supercurrent observed in SQS Josephsons has nevertheless remained significantly below the predicted values (see [1] and references therein). In the single fullerene SQS junctions obtained in the Nanospin group, we occasionally also observed Josephson coupling, with very small critical currents, as shown in Fig. 1.6. Such Josephson junctions have a low quality factor $Q \approx 1$ and no hysteresis. Further, a residual resistance below the switching current I_s is related to the phase diffusion of the Josephson state along the 'tilted washboard' potential, which will be further discussed in section 2.1.2. Such features are generic to small Josephson junctions with a large normal state resistance [41]. The strong reduction of the switching current with respect to the ideal critical current value $I_0(R_j) = G_N\Delta/e$ (equal to 6 to 20 nA here, depending on the gate voltage; G_N is the normal state linear

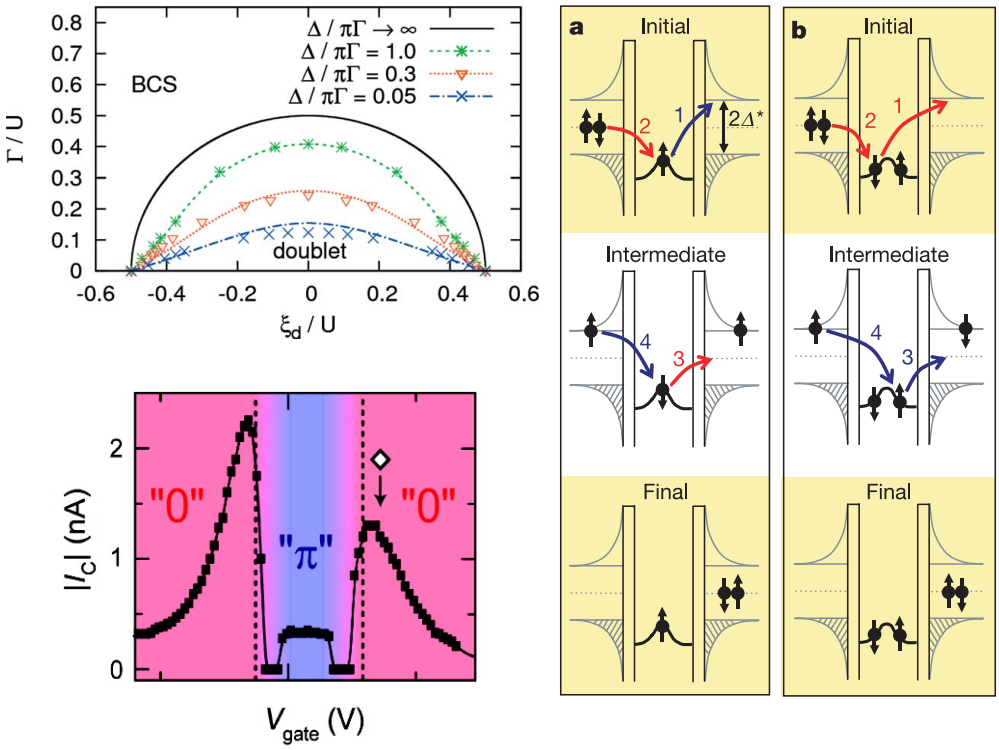

Figure 1.7: **0-π transition. Top left:** phase diagram of the QD ground state [16], highlighting the $E_b = 0$ phase boundary for different values of $\Delta/\pi\Gamma$. Here, $\xi_d = \epsilon_{\rm QD} + U/2$, thus $\xi_d = 0$ is the center of the oddly occupied Coulomb diamond. The symbols are from NRG calculations [15] and the lines are analytical approximations [16]. **Bottom left:** experimental signature of 0-π phase transition, visible as a marked discontinuity in the switching current, in a CNT-based SQUID [44]. **Right side panels:** cartoon of the different intermediate states leading to the transfer of a Cooper pair, in a $0-$ and $\pi-$junction, respectively. Note the different spatial order of the Cooper pair singlet in the final state in the $\pi-$junction [35].

conductance) is understood as an effect of finite temperature and environmental coupling (e.g. to phonons on the quantum dot or electromagnetic modes in the leads). In an unshunted junction hosting a single spin-degenerate conductance channel, the coupling to the environmental admittance is expected [42, 43] to produce a reduction of the switching current following

$$I_s/I_0 = (1 - \sqrt{1 - G_N h/2e^2}\,)^{3/2}. \tag{1.3.5}$$

Experimentally, this 3/2 power-law dependence was observed to hold in metallic superconducting single electron transistors [42] and in carbon nanotube junctions [43]. It is remarkable that whereas the justification of Eq. (1.3.5) strictly holds for weakly damped junctions [42], a very good agreement to experiment is still found in the device shown in Fig. 1.6, which is at the crossover between the under- and overdamped regimes.

0-π transition

In case both leads are rather strongly coupled to the QD, the Kondo screening cloud extends into both contacts. The screened-unsceened ground state transition in a SQS junction can thus strongly affect the ability of the junction to resonantly transfer Cooper pairs [14]. The singlet-doublet QPT leads to a change in the current-phase relation of the Josephson junction, the phase acquiring a π-shift in the case of a doublet GS. A (probably simplistic, yet illustrative) cartoon explaining why the Cooper pair is $\pi-$shifted

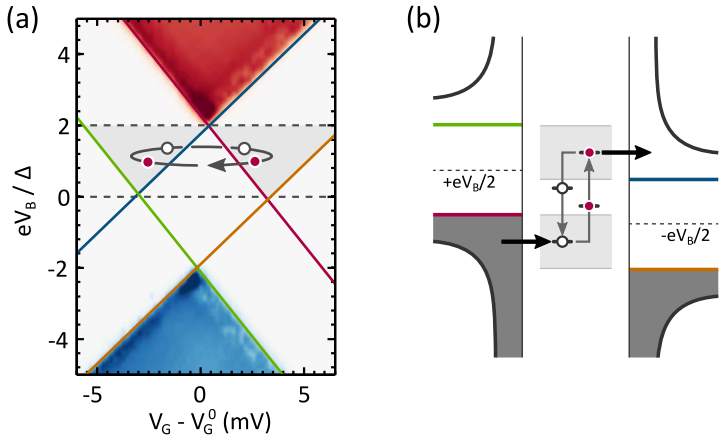

Figure 1.8: (a) Experimental current map of a superconductor - quantum dot hybrid device as function of gate and bias potential, in absence of periodic gate drive (device $\mathcal{S}$). Colored solid lines correspond to the four superconducting gap edges as illustrated in (b). The device is operated as a single level turnstile when its state is modulated periodically around its $(n, n+1)$ charge degeneracy point. The on-state currents are $I_+ = 290$ pA (red) and $I_- = -250$ pA (blue). (b) Energy diagram of the device with a small bias applied, illustrating electron tunneling events in and out the quantum dot. Grey areas indicate the amplitude range for solely forward tunneling, also seen in (a). Driving the turnstile with a square wave signal allows for tunneling to occur within a narrow energy window.

(inverted) after traversing the SQS junction is reproduced in Fig. 1.7. Several transport experiments have brought striking signatures of the 0-π transition in SQS Josephson junctions [34–36, 44]. As will be discussed in section 4.3.3, a single experiment in which the tunnel coupling to one superconducting lead could be continuously tuned would allow to combine the signatures of the QPT both in spectroscopy and Josephson transport.

1.4 SQS junction as a single electron injector and turnstile

The following section will focus on the ability to control current flow at the single electron level, taking advantage of the properties of *weakly coupled* SQS junctions, such as the one shown in Fig. 1.2. We will consider sequential tunneling processes only, and higher-order effects will appear as detrimental. The quest for controlling current flow down to the single electron level in nanodevices has triggered a vast activity on quantum metrological current sources in recent years [45–61]. In a quantum current source, electrons are conveyed one by one across a mesoscopic conductor, which is achieved by Coulomb repulsion. Among the most promising recent approaches are islands with tunable barriers in 2D electron gases [46, 50, 55, 61] along with superconducting single electron transistors [51]. Beyond metrological applications, the development of on-demand single-electron sources opens broad perspectives in the field of quantum coherent electronics and electron optics [62–66].

The SINIS turnstile, invented by Jukka Pekola and collaborators in Helsinki [51, 67], takes advantage of the sharply defined energy gap in the superconducting density of states, as an energy filter. A normal metallic region (N) is weakly coupled to two superconducting leads (S) through tunnel barriers. N has to be sufficiently small to have a Coulomb charging energy U, which should be at least on the order of the superconducting gap in the leads, Δ. Nevertheless, N displays a dense set of states, appearing as continuous at accessible temperatures. A finite island temperature then allows for an entire energy window $\sim k_B T$ of available states in N for tunneling, which leads to turnstile operation errors associated to double occupation or tunneling into the wrong lead [67].

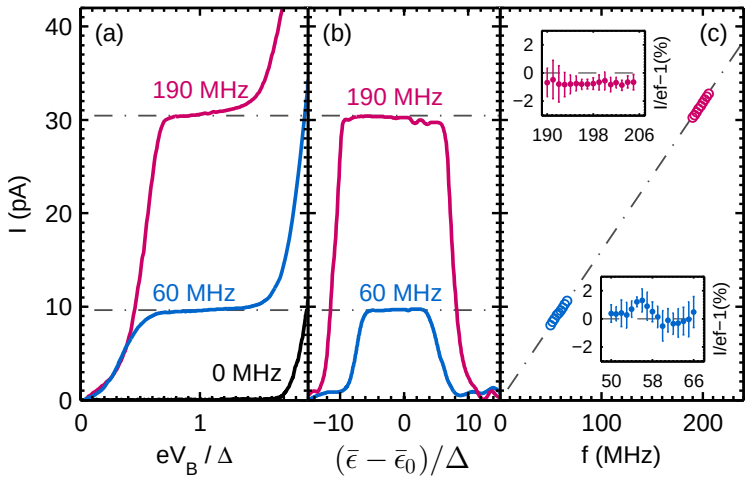

Figure 1.9: (a) Current-bias traces measured near the charge degeneracy point. Characteristic plateaus appear with $I = ef$ (indicated by dashed lines) when applying a small modulation signal (magenta: $A_\epsilon \approx 0.64\Delta$, $f = 190$ MHz, blue: $A_\epsilon \approx 1.0\Delta$, $f = 60$ MHz) to the gate. The black trace shows the current response with no ac gate drive. (b) Current-gate traces measured for $A_\epsilon \approx \Delta$ and the same frequencies as in (a), at $V_b = \frac{3}{2}\Delta/e$ (magenta) and $V_b = \Delta/e$ (blue). (c) Current at the inflection point of the plateaus shown in (a) as function of operation signal frequency. The insets highlight deviations of the normalized current I/ef from 1 in both the low and high frequency ranges (all data are from device $\mathcal{S}$).

During the thesis of David van Zanten, we have realized a source of quantized dc current based on a single quantum energy level [68], which will be described in this section. The physical operation principle is similar to the SINIS turnstile, with the important difference that electrons are here carried by a single energy level of a quantum dot (Q). After demonstrating the expected principal turnstile operation characteristics, we focus on novel electronic transport features of the SQS turnstile. In particular, we show that tunneling can be tuned to occur within a narrow energy window. We theoretically compare the dominant turnstile error processes in the SQS and SINIS devices, concluding that the former has a lower sensitivity to out-of-equilibrium quasiparticles.

The charging energy U, the quantum dot orbital level spacing δE, the tunnel couplings γ_i and the capacitances C to the three terminals source, drain and gate, which we denote by indices S, D and G, respectively, are determined from transport data in static conditions, that is, measuring the current I as a function of the applied bias voltage V_b and gate voltage V_g. The $I(V_b, V_g)$ maps show typical Coulomb blockade behavior in which only a single or at most a few charge degeneracy points (Fig. 1.8a) are accessible in the available gate voltage range. We find charging energies $U > 50$ meV and orbital energy level spacings δE on the order of 1 meV or higher. Because $\delta E \gg k_B T$, the thermal population beyond the ground state is vanishingly small and electron transport occurs uniquely through a single orbital quantum level [17]. We focus on two devices with quite different tunnel couplings: $\mathcal{S}$ has rather symmetric tunnel couplings ($\gamma_S = 2.1$ μeV, $\gamma_D = 1.4$ μeV), while $\mathcal{A}$ is strongly asymmetric ($\gamma_S = 5.2$ μeV, $\gamma_D = 0.4$ μeV). A detailed description and modeling of the dc transport characteristics of both devices can be found in [69].

Turnstile operation

As discussed earlier, the absence of quasi-particle states at energies $|E| < \Delta \approx 260$ μeV in the leads results in a suppression of conductance for $|V_b| < 2\Delta/e$ at any gate voltage (Fig. 1.8a). For turnstile operation, a small constant bias $0 < |V_b| < 2\Delta/e$ is applied and a periodic modulation signal with frequency f and variable amplitude is added to the static gate potential. The energy difference between the $n+1$ and n

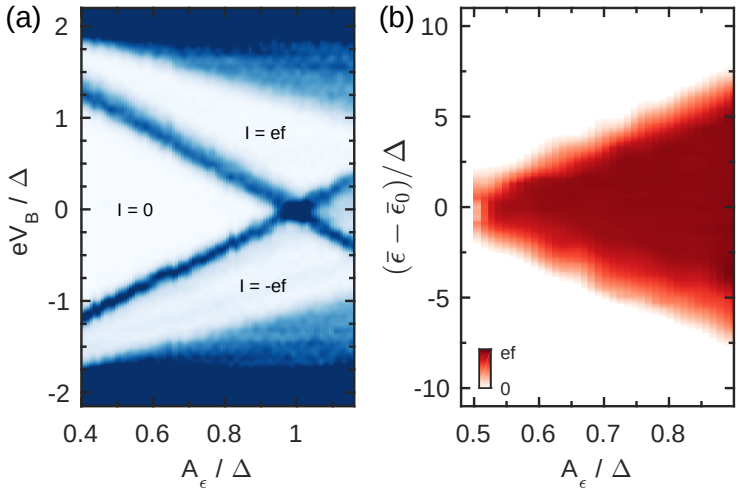

Figure 1.10: (a) Colormap of $\partial I/\partial V_b$ as a function of bias and gate modulation amplitude ($f = 56$ MHz, $\bar{\epsilon} = \bar{\epsilon}_0$). Narrow blue regions, corresponding to rapid increase in current, separate areas of voltage independent current (white), with values $I = 0$ and $I = \pm ef$. (b) Colormap of turnstile current as a function of static gate offset from degeneracy point and gate modulation amplitude ($f = 60$ MHz, $V_b = 1.5\Delta/e$). All data are from device $\mathcal{A}$.

electron occupation numbers in the quantum dot, $\epsilon(t)$, varies between $\bar{\epsilon} \pm A_\epsilon$, where $\bar{\epsilon}$ is controlled by the static voltages V_g and V_b. A single electron can tunnel into the quantum dot as soon as $\epsilon(t)$ reaches the occupied states of the contact with the higher chemical potential (Fig. 1.8b; right grey triangle in Fig. 1.8a). By raising $\epsilon(t)$ via the back gate to reach the empty states above the upper gap edge in the opposite lead (left grey triangle in Fig. 1.8a), the level is emptied to that lead. By driving $\epsilon(t)$ cyclically, one electron is conveyed per cycle from the higher chemical potential lead to the other, giving rise to a dc current $I = ef$.

The combination of both above tunneling processes, in and out of the quantum dot, corresponds to the desired operation mode of the turnstile and will be named *forward* tunneling in the remainder. As shown in Fig. 1.8, forward tunneling requires the amplitude A_ϵ of the modulation of $\epsilon(t)$ to be $A_\epsilon > \Delta - e|V_b|/2$. On the other hand, a too large modulation amplitude $A_\epsilon > \Delta + e|V_b|/2$ will eventually allow for tunneling into/from the opposite lead. Such *backtunneling* processes are detrimental to current quantization, and their signature will be discussed later on.

Throughout this section, a square wave signal, with a rise time $\tau \approx 1.6$ ns associated to the finite bandwidth of the generator, is used for modulating $\epsilon(t)$. The experimental dc current $I(V_b)$ measured for $\epsilon(t)$ with an amplitude A_ϵ around $\bar{\epsilon} = \bar{\epsilon}_0 \equiv (\mu_S + \mu_D)/2$ is shown in Fig. 1.9a. Here $\mu_{S,D}$ are the leads' chemical potentials, with $\mu_S - \mu_D = eV_b$. Above the threshold voltage for forward tunneling, $V_b^{fw} = \pm 2(\Delta - A_\epsilon)/e$, a broad current plateau at $I = ef$ develops. Turnstile operation is only effective for a restricted range of $\bar{\epsilon}$ (Fig. 1.9b). The value of the turnstile current, determined at the inflection point, follows the predicted linear dependence on frequency (Fig. 1.9c), with a standard deviation of about 1 %, to which adds a systematic deficit of about 0.7 % at higher frequencies. The plateaus show a small residual slope at all frequencies, which is due to a parasitic capacitive crosstalk between gate and lead. This could be strongly reduced in later experiments.

At charge degeneracy, the thresholds for the onset of both forward and backtunneling can be seen as the narrow blue stripes in Fig. 1.10a. Both thresholds cross at $V_b = 0$ when $A_\epsilon = \Delta$. Whereas the frequency-dependent transmission of the ac gate signal to the device is not precisely known, this crossing is used to calibrate A_ϵ. The bright color identifies regions of voltage-independent current, corresponding

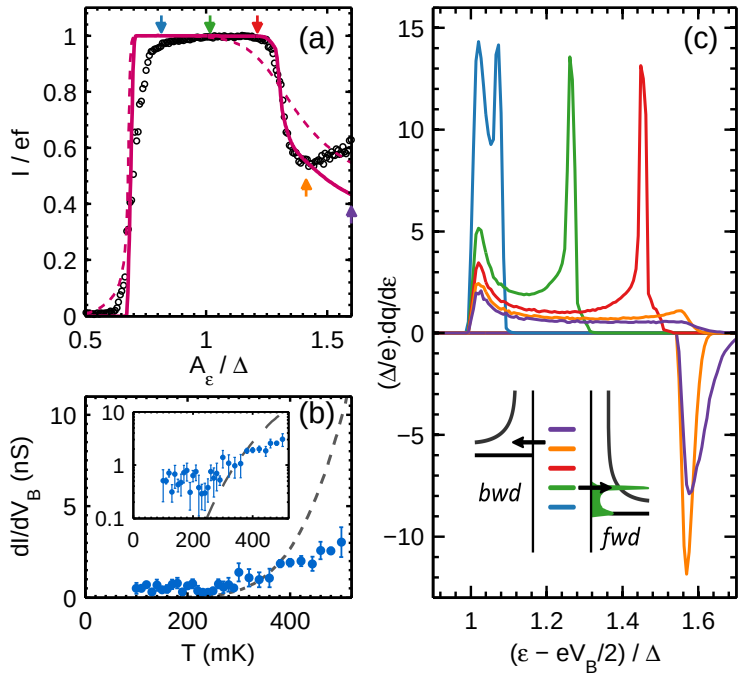

Figure 1.11: (a) Turnstile current as a function of operation signal amplitude (device $\mathcal{A}$, $f = 56$ MHz, $\bar{\epsilon} = \bar{\epsilon}_0$ and $eV_b = 0.7\Delta$). The sharp decrease in current indicates the sudden onset of backtunneling. The continuous line is the numerical calculation for the SQS with all parameters determined by the device dc transport properties (see text). The dashed line is the analogous calculation for an SINIS device with normal state resistance $R_N = 300$ kΩ, $U = 3.0\Delta$ and assuming quasi-equilibrium of electrons in N by electron-phonon relaxation [70]. The arrows indicate the values of A_ϵ used in (c). (b) Slope at inflection point of $I(V_b)$ on the turnstile plateaus, averaged over A_ϵ, as a function of temperature (device $\mathcal{A}$). The dashed line is the calculation for the SINIS device, with parameters as in (a). (c) Calculation of the energy distribution of the delivered charge per cycle, for different gate drive amplitudes A_ϵ, with parameters as in (a). The negative part of the panel displays the backtunneling contribution. The highest position of the quantum dot level, as determined by the gate modulation, is represented in the inset by the lines of corresponding colors.

to $I = 0$ and $I = \pm ef$, respectively. When $\bar{\epsilon}$ is slightly detuned from $\bar{\epsilon}_0$ by the static gate potential, the onset of forward tunneling is linearly shifted towards larger A_ϵ (Fig. 1.8b). Note that turnstile operation requires two successive tunneling events to occur. This is visible in Fig. 1.10b, where the current is shown as function of gate detuning and modulation amplitude. For larger amplitudes A_ϵ, an increasing tolerance of the turnstile operation with respect to the proper tuning of $\bar{\epsilon} - \bar{\epsilon}_0$ develops.

Signatures of single quantum level operation

Having evidenced electron turnstile operation, let us now identify the hallmarks of transport through a single quantum energy level. In SINIS turnstiles, backtunneling can be occasioned by electrons from the high-energy tail of the thermal energy distribution in N. The backtunneling probability increases thus steadily and smoothly as A_ϵ is cranked up [71]. Conversely, in a SQS turnstile backtunneling sets in abruptly, when the threshold $A_\epsilon = \Delta + |V_b|/2e$ is exceeded. This is seen in Fig. 1.11a, where at high enough modulation amplitudes, the current drops suddenly from ef. We numerically model the turnstile current dependence on A_ϵ, both for the SINIS and the SQS turnstile, by solving the time-dependent rate equations using the measured output of the ac signal generator. In the SQS case, the instantaneous tunneling rates to each lead are found from the retarded Green's function's pole [25, 26, 69], that is, beyond Fermi's golden rule. This is particularly important near the singularities in the superconducting density of states (see

Supplemental Information file). The calculation (continuous line in Fig. 1.11a) nicely captures the abrupt decrease of the current as soon as the backtunneling threshold is met. For comparison, in a SINIS device with parameters taken from the most precise devices presently studied [72, 73], the onset of backtunneling is markedly smoother (dashed line).

This particularly sharp onset of backtunneling is all the more pronounced if the rise time τ of $\epsilon(t)$ is short, or more precisely, if the time available for forward tunneling *only* is brief. If ϵ is raised to the backtunneling threshold within $\tau \ll \gamma_{S,D}^{-1}$, the probability of backtunneling may actually exceed that of forward tunneling. This means that a current inversion, of magnitude up to ef, might eventually be produced with proper parameter combinations. This could however not be observed in our experiment, because the square wave rise time is of the same order of magnitude as the inverse tunneling rate ($\tau \sim \gamma_{S,D}^{-1}$).

To highlight the energy selectivity of the tunneling process, we calculate the energy resolved transferred charge $dq/d\epsilon$ over a half-period of an ac gate cycle, using the assumptions and parameters of the calculation in Fig. 1.11a. The results are shown for different values of A_ϵ and for both forward and backward processes in Fig. 1.11c. While a certain fraction of forward tunneling occurs near the superconducting gap edge (where the lead's density of states is largest), good energy selectivity of the tunneling is achieved for sufficiently large values of A_ϵ. For even larger A_ϵ, backtunneling is possible, which we represent using negative values of $dq/d\epsilon$. The accuracy of the energy selectivity is ultimately limited by the tunnel coupling, but in the present experiment it is dominated by deviations of the ac drive signal from a perfect square wave. The SQS device is expected to yield about the same energy resolution as the semiconducting ac single electron source [62], assuming identical gate drive and tunnel couplings.[1] For comparison, the energy distribution of levitons [65] is pinned to the Fermi level.

Turnstile operation errors

We now move to the discussion of possible error processes of the SQS turnstile. One obvious source of error is the missed tunneling event. As the tunneling rate is finite, tunneling may be missed during the corresponding half-period, leading to $I < ef$. For a single-level quantum dot, the Fermi golden rule tunneling rate for each lead ($i = S, D$) can be written as $\Gamma_i = (2)\,\gamma_i\, n_s(\epsilon(t) \pm eV_b/2)$, where $n_s(E)$ is the normalized quasi-particle density of states in the superconducting leads. The factor of 2 takes into account the possibility of tunneling for two spin projections, and is present only for tunneling at one of the leads. For a symmetric square wave modulation of $\epsilon(t)$, the probability of missed tunneling at one of the leads can be roughly estimated as $e^{-\Gamma_i t_{\rm eff}}$. Here, the effective time available for tunneling $t_{\rm eff} \approx 1/(2f) - \tau$, takes into account the signal rise time. At frequencies around 200 MHz, this estimate gives a current deficit of 0.8 % for the device parameters of sample $\mathcal{S}$, which agrees well with the experimental value of about 0.7 % (Fig. 1.9c inset). For device $\mathcal{A}$, the missed tunneling rates at high frequencies are higher because of the tunneling bottleneck at its less transparent tunnel junction.

In turnstile operation with a normal metal island and at finite temperature, a fraction $\sim \exp(-\Delta/k_BT)$ of electrons has sufficiently high energy for backtunneling. In aluminum-based SINIS turnstiles, the associated error is rapidly dominant above about 300 mK [73]. An expected hallmark of energy quantization in the turnstile operation should be a rather marked temperature insensitivity as long as $\delta E \gg k_BT$ and Pauli blocking of states in the leads can be neglected. We have followed the turnstile operation of device $\mathcal{A}$ as a function of temperature up to 0.5 K and we indeed observe the turnstile plateau to subsist through the entire temperature range, with only a rather moderate increase in error rate. We quantify the error by the $I = ef$ plateau slope dI/dV_b. As seen in Fig. 1.11b, this slope shows only little dependence on temperature. For comparison, the calculation of the same for a SINIS turnstile, shows a rapid divergence above about 300 mK. While thermal errors are negligible only in the low mK range in most reported turnstiles, the SQS device can operate up to relatively high temperatures without suffering from thermal tunneling.

[1] This is because the integral over the density of states of a superconductor is the same as in the normal state.

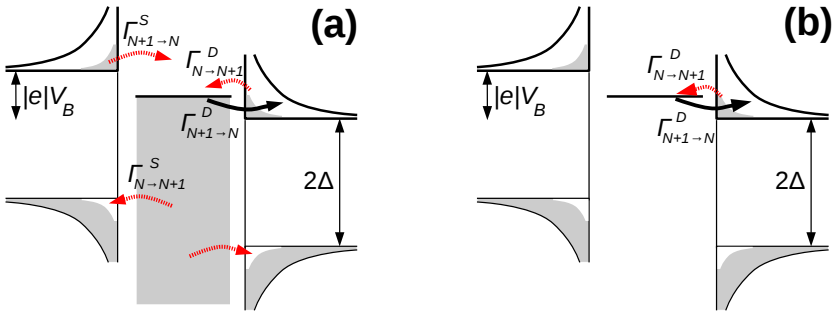

Figure 1.12: Schematic view of different sequential tunneling processes in the SINIS (a) and SQS (b) turnstiles on the ejection stage. The main ejection process is shown by the solid black arrow, various parasitic processes are shown by dotted red arrows. In both panels the grey shading corresponds to the occupied states.

An important source of errors in superconducting turnstiles is related to the presence of non-equilibrium quasiparticles in the leads, with concentration $x_{\rm qp} = n_{\rm qp}/(2\rho_n\Delta)$. Here, $n_{\rm qp}$ is the quasiparticle density in the lead and ν is the density of states (per spin projection) at the Fermi level in the normal state. Such quasiparticles can accumulate as a consequence of noise and, in particular, of the turnstile operation itself and are well known to be difficult to evacuate [72, 74]. Using the diffusion model described in [72] we estimate $n_{\rm qp} \sim 10\,\mu{\rm m}^{-3}$ near the SQS junction, yielding $x_{\rm qp} \approx 2\times10^{-6}$. In the SINIS turnstile, direct tunneling of such quasi-particles between one lead and the central island occurs with a rate $\sim x_{\rm qp}\, g\, \Delta$ leading to a frequency-independent leakage current. Here g is the dimensionless conductance of the tunnel junctions, in units of the conductance quantum. Crucially, this leakage, which is at present the main source of errors in SINIS turnstiles [72], is suppressed for the SQS device by the lack of states in the quantum dot at the quasiparticle energy.[2] For tunneling processes of higher order in $\gamma_{S,D}$, the limitations to accuracy of the SINIS and the SQS devices are comparable.

To conclude the discussion of the respective merits of the SINIS and SQS turnstiles, the SQS device is in principle immune to errors induced by sequential tunneling processes of residual quasi-particles in the leads. As far as higher-order processes are concerned (quasiparticle cotunneling and Cooper pair-electron cotunneling), the error at equal reduced conductance g is theoretically the same in both turnstiles. However, it has to be noted that in order to reach the same g as in a SINIS junction, the SQS junctions needs a quite strong tunnel coupling, because a single channel conducts the current, as opposed to thousands of conductance channels in a planar NIS junction. The SQS junction is therefore much more prone to higher-order effects in γ/Δ. To answer a question I am frequently asked: the SQS turnstile is quite certainly not the future of quantum current metrology. It's originality resides in the ability to deliver electrons at well-defined energies. Therefore, and as will be described in the *Perspectives* chapter, one of the main applications envisioned in the near future is turned towards the use of the SQS single electron injector as a source of well-defined energies in quantum circuits.

[2] Another contribution of the non-equilibrium quasiparticles, the Pauli blocking term, may also be significantly suppressed in the SQS turnstile depending on the quasiparticle distribution function.

Chapter 2

A thermal view on quantum nanoelectronic devices

The flow of heat at the microscopic level is a fundamentally important issue, in particular if it can be converted into free energy via thermoelectric effects [75]. The ability of most conductors to sustain heat flow is linked to the electrical conductance σ via the Wiedemann-Franz law: $\kappa/\sigma = L_0 T$, where κ is the heat conductance, $L_0 = \frac{\pi^2 k_B^2}{3e^2}$ the Lorenz number and T the temperature. While the understanding of quantum charge transport in nano-electronic devices has reached a great level of maturity, heat transport experiments are lagging far behind [76], for two essential reasons: (i) unlike charge, heat is not conserved and (ii) there is no simple thermal equivalent to the ammeter. Heat transport can nevertheless give insight to phenomena that charge transport is blind to [77, 78] and, remarkably, a series of experiments has demonstrated the very universality of the quantization of heat conductance, regardless of the carrier statistics [77–85].

On the other hand, many low temperature quantum transport experiments in nanoelectronic devices assume isothermal conditions. Nevertheless, it is well known that the electrons in nanodevices at low temperatures are generically overheated with respect to the phonons, due to the weakness of electron-phonon coupling and the difficulty to completely shield incoming radiation from higher temperature stages. Further, the electronic device operation itself can be the source of dissipation and even thermal avalanches, such as in the case of thermally hysteretic Josephson junctions.

The first part of this chapter will give an overview of my recent activities about overheating and thermal avalanches in Josephson junctions, when driven close to their critical current. The important message here is that electronic overheating can have paramount influence on the device characteristics, which must be considered in the interpretation of the data. The second part describes experiments in which thermal gradients were created on purpose as to study thermal transport. An experiment about phononic heat transport between two nearby quantum devices [86] will not be discussed here. We will rather focus on a recent experiment on the test of the Wiedemann-Franz law at the nanoscale [87].

2.1 Electron overheating in Josephson junctions

2.1.1 Dissipation and thermal balance in μ-SQUIDs

Our group has a long-standing collaboration with Anjan Gupta from IIT Kanpur on the thermal properties of micro-SQUIDs based on Nb microconstrictions. Such devices display excellent performances for characterizing micromagnets, such as small crystals of molecular magnets [88]. Their hysteretic $V(I)$ characteristic however requires in usual operation a slow operation mode, because once the superconducting switching current of the junction has been reached, the current has to be significantly reduced again to

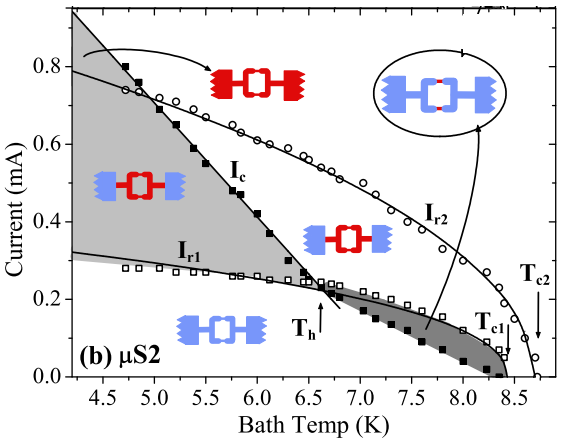

Figure 2.1: Variation of the different critical currents with temperature. I_c is the critical current, I_{r1} and I_{r2} are the retrapping currents of different portions of the circuit. The cartoons depict the state of the device during current ramp-down, with blue showing the superconducting and red showing the resistive portions. The light gray-shaded area is the bistable region where the whole device is in the fully superconducting state during the current ramp-up from zero. In the dark gray-shaded region, only the weak links are resistive. Taken from [89].

recover the superconducting state, due to overheating. Together with Anjan Gupta and his group, we have studied various routes to optimizing the thermal runaway in the dissipative state. The main ideas can be summarized as follows:

- When some part of a superconducting circuit turns normal due to a too large current density, the N-S interface will propagate depending on the balance between Joule heating in N and thermal drain to remote reservoirs. From this one can get a rather complex "phase diagram" of the circuit state, with larger section regions becoming progressively normal as the bias current current increases (Fig. 2.1).

- At higher temperatures, the devices are less hysteretic mainly because the critical current I_c is smaller and thermal couplings are better. However, we have also found that the picture is not as simple as described above and that the superconducting proximity effect from the larger leads on the constriction also influences this reduction in hysteresis [89].

- It is known that shunting the constriction with a less resistive path allows reducing the local thermal runaway, and thus speeding up the SQUID operation. However, such a normal shunt should not be too close, as to avoid inverse proximity effect on the constrictions. It should not be too far either, because the large kinetic inductance of the superconducting path to the shunt will not allow to deviate sufficiently rapidly the current flow from the constriction. In the work of Nikhil Kumar [90] we compare the thermal hysteresis of the same SQUID with and without a nearby gold shunt. The gold shunt is removed by a wet etch in between the two measurements. The hysteresis is significantly less pronounced in the presence of the shunt.

- Usually, when the critical current is exceeded, the quantum phase runaway heats the constriction to temperatures higher than T_c, meaning that the Josephson coupling across the junction also vanishes and the constriction turns entirely normal. However, this needs not be true. When the ratio of the heat generation to its evacuation, which we quantify as a dimensionless parameter β, is sufficiently small, the Josephson coupling is not entirely destroyed although the junction is dissipative (Fig. 2.2). This allows understanding the *a priori* surprising voltage oscillations in the dissipative state displayed by some SQUIDs, when the magnetic field is swept [91].

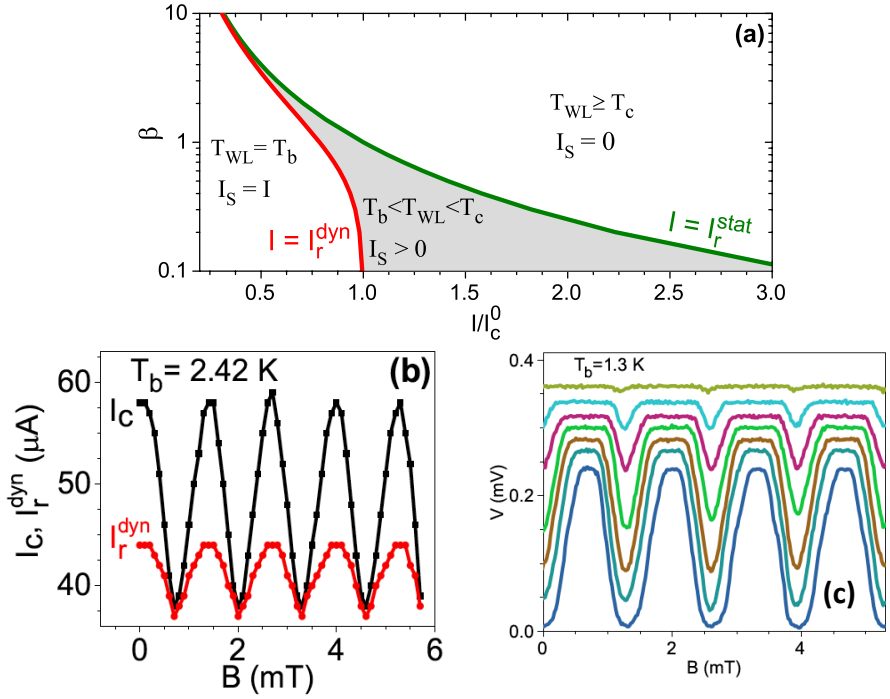

Figure 2.2: (a) Device state diagram, where β is the ratio of heat production to its evacuation at $I = I_c$. I_r^{stat} is the current above which the weak link temperature is heated above T_c. I_r^{dyn} is the current below which the device falls into the zero-voltage state, whatever its history. The grey shaded region is the dynamic regime where the weak link has a finite voltage but carries a non-zero supercurrent. (b) Oscillations of the critical and the retrapping currents with magnetic field in the hysteretic regime at 2.42 K. (c) $V(B)$ oscillations (for bias currents between 50 to 70 μA) of another device with small critical current and thus small $\beta = 0.36$ at 1.3 K. Taken from [91].

2.1.2 Electron overheating in *ac* driven SNS Josephson junctions

This study is an extension to the work led by Hervé Courtois when visiting Aalto University in 2008 [92], which demonstrated that hysteresis in SNS Josephson junctions is indeed of thermal origin. The present Nb-Au based SNS junctions were realized using a novel lithographic technique, developed by Sayanti Samaddar in our group [93]. Shadow evaporation of Nb is indeed problematic because the high melting temperature of Nb leads to strong degassing of the usual organic lithographic resists, which in turn deteriorates the superconducting properties of the Nb nanostructures. With Sayanti Samaddar, we have developed the use of a metallic mask, based on an Al/Mo bilayer. Here, the pattern is reactive-ion etched into the top Mo layer, through a lithographically defined structures in an organic resist layer. Then, the bottom Al layer is easily and selectively etched using rather soft etchants such as the standard clean-room developer MF319. This can lead to suspended Mo bridges such as seen in Fig. 2.3, which allow for shadow evaporation of clean S-N interfaces.

This allowed us studying the response of high-critical current proximity Josephson junctions to a microwave excitation. Electron overheating in such devices is known to create hysteretic dc voltage-current characteristics. Here, we demonstrate that it also strongly influences the ac response [94]. The interplay of electron overheating and ac Josephson dynamics is revealed by the evolution of the Shapiro steps with the microwave drive amplitude. Extending the resistively shunted Josephson junction model by including a thermal balance for the electronic bath coupled to phonons, a strong electron overheating is obtained.

A normal metal (N) coupled to two superconducting electrodes (S) constitutes a Josephson junction, that

is, a device capable of sustaining a dissipationless supercurrent [95–97]. The small normal state resistance and lead-to-lead capacitance of SNS junctions make these strongly overdamped in the RCSJ model [95], meaning that the quantum phase dynamics is intrinsically non-hysteretic. Still, hysteresis is observed in the voltage-current (V-I) characteristics of high-critical current SNS junctions due to electronic over-heating associated to the sudden onset of dissipation when the bias exceeds the critical current [92]. Besides, under a microwave excitation at frequency ν, the junction characteristics display current-independent voltage plateaus defined by $V_n = nh\nu/2e$ with n an integer [98]. These so-called Shapiro steps are due to the phase-locking of the supercurrent oscillations at the Josephson frequency $2eV/h$ to the microwave. Shapiro steps have been frequently used for studying the phase dynamics of a variety of Josephson junctions [99–103], including junctions based on novel materials [104–111]. Still, the interplay between the electron over-heating and the ac Josephson dynamics has not yet been investigated.

This section reports a study led by Alessandro De Cecco [94] in which we discuss the response of high-critical current proximity Josephson junctions to a microwave excitation. We demonstrate the prominent role of electronic over-heating in the Shapiro steps map. Low-index steps can be masked by the switching to the resistive state. A simple model explains this behavior as well as the observation of a sharp discontinuity in the measured critical current when the ac current is increased.

The Nb-Au-Nb junctions are fabricated using the lift-off lithography technique based on the metallic bilayer shadow mask described above [93], which avoids the deterioration of Nb superconducting properties by organic contamination (Fig. 2.3c inset). The junctions were all about 210 nm wide, the separation between the Nb electrodes ranging from 180 to 500 nm, while the Au part was about 200 nm longer in order to ensure a good overlap with each electrode. The normal-state resistance of the junctions can be related to a diffusion constant D in Au of about 100 cm^2/s. The critical temperature of the Nb electrodes is 8.5 K. Table 2.1 lists the main device parameters for the different junctions investigated.

DC transport

Fig. 2.3a-b show V-I characteristics of a typical sample. At low temperature, a strong superconducting branch is observed (Fig. 2.3a), with a large critical current I_c exceeding 100 μA. This is achieved owing to the short length of the Au bridge and the high interface transparencies. Above I_c, the V-I characteristic switches to the ohmic branch, characterized by the normal-state resistance R_N. When the current is lowered again, the V-I characteristic remains on the ohmic branch down to the so-called retrapping current $I_r < I_c$. This pronounced hysteretic behaviour is of thermal origin and is typical of SNS junctions with a large critical current density [92]. At higher temperatures however, the thermal instability at the switching is negligible and the characteristic recovers a reversible behavior (Fig. 2.3b).

The temperature dependence of the critical current is displayed in Fig. 2.3c. The properties of long SNS junctions depend only little on the superconducting electrodes' energy gap Δ, but are mainly governed by the normal island's Thouless energy [96, 101] $E_{\rm Th} = \hbar D/L^2$, where D is the diffusion constant and L the length of N. Within the Usadel equations framework and assuming $E_{\rm Th} \ll \Delta$ and $k_BT > E_{\rm Th}$, the temperature dependence of I_c is [112]:

$$eR_N I_c = \eta\, E_{\rm Th} \frac{32}{3+2\sqrt{2}} \left[\frac{2\pi k_B T}{E_{\rm Th}}\right]^{3/2} \exp\left(-\sqrt{\frac{2\pi k_B T}{E_{\rm Th}}}\right). \tag{2.1.1}$$

Here the phenomenological parameter $\eta < 1$ describes a reduction in the critical current related, for instance, to non-ideal interfaces. A very good fit to the data is obtained in all devices, with η always exceeding 0.6, see Table 1. The effective length $L_{\rm eff} = \sqrt{\hbar D/E_{\rm Th}}$ associated to the fit Thouless energy $E_{\rm Th}^{\rm fit}$ exceeds the mere separation L between the electrodes. It should indeed include about twice the superconducting coherence length since Andreev reflections take place in S over such a length [112]. The dependence of the critical current on a perpendicular magnetic field (Fig. 2.3d) shows both a quasi-gaussian monotonic decay associated to dephasing and a oscillatory part arising from interference effects [113, 114]. The retrapping

N^o	L (nm)	R_N (Ω)	$E_{\rm Th}^{\rm fit}$ (μeV)	$L_{\rm eff}$ (nm)	η	I_c^0 (μA)	I_r^0 (μA)	T^* (K)
J1	225	2.4	28.1	474	0.86	104	33	1.9
J2	300	2.1	23.6	536	0.89	78	45	1.4
J3	180	1.7	49.6	390	0.78	178	35	2.6
J4	500	3.6	9.9	785	0.67	14	2	1.1

Table 2.1: Parameters of the reported samples. In all samples, the Au strip width W is 210±10 nm, its thickness is 20 nm for sample J1 and 30 nm for samples J2 - J4, while Nb thickness is 60 nm for sample J1 and 90 nm for samples J2-J4. L is the Nb-Nb distance. R_N is the normal-state resistance measured at 4.2 K. $E_{\rm Th}^{\rm fit}$ and η are the fitting parameters in Eq. 1. $L_{\rm eff} = \sqrt{\hbar D/E_{\rm Th}^{\rm fit}}$ is the effective junction length. I_c^0 and I_r^0 the values of the critical/retrapping currents respectively at $T \to 0$ and in the absence of magnetic field and microwave excitations. T^* is defined by $I_c(T^*) = I_r^0$.

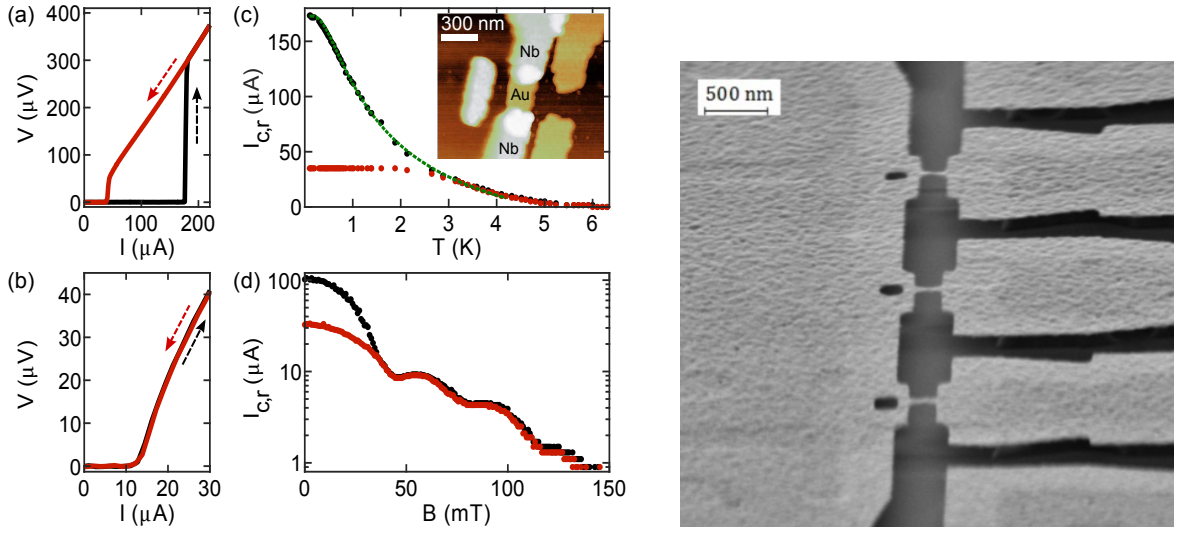

Figure 2.3: V-I characteristics of device J3 measured at temperatures of (a) 100 mK and (b) 4.2 K. The arrows indicate the sweeping direction of the current bias. (c) Temperature dependence of the critical current I_c (black dots) and the retrapping current I_r (red dots) for sample J3. The green dotted line represents a fit to Eq. (1). Inset: AFM image of a typical Nb-Au-Nb junction. (d) Magnetic-field dependence of the critical current I_c (black dots) and the retrapping current I_r (red dots) (T = 280 mK, device J1). Steps in current values appearing at large magnetic field are artifacts. (e) Grazing angle SEM picture of the suspended Mo-Al bilayer mask. The Mo (bright) is suspended at the position where the weak links will be created.

current can be roughly thought of as the value of the critical current at a bias-dependent, higher electronic temperature T^*, determined by the thermal balance between the dissipated Joule heat and the coupling to the phonon bath. Conversely, T^* is also the temperature scale above which I_r and I_c merge and the behavior of the junction becomes non-hysteretic.

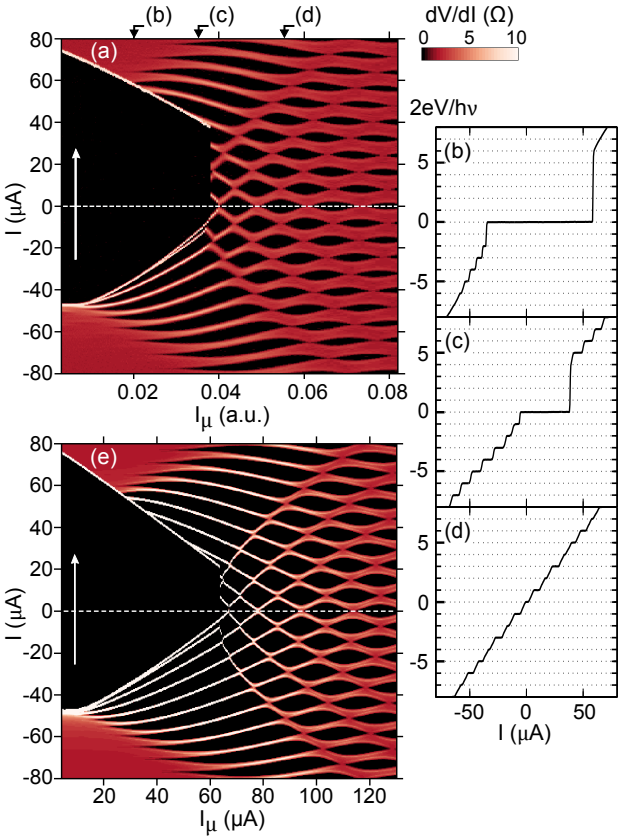

Figure 2.4: (a) Differential resistance map as a function of the dc current bias I and the microwave excitation amplitude I_μ for a frequency $\nu = 6$ GHz (device J2, $T_{\text{bath}} = 100$ mK). The white arrow indicates the sweeping direction of the dc current bias. The top black arrows point to the individual V-I curves taken at microwave drives of (b) 0.020 (c) 0.035 (d) 0.056 (a.u.). Voltage is normalized to $h\nu/2e$. (e) Calculated differential resistance map, including thermal effects.

Microwave response

We now turn to the effect of a microwave excitation on the V-I characteristics. Microwave signals in the frequency range 1 to 26 GHz and with a power P_μ were applied to the shielded cavity containing the sample. As the impedance of our samples is small compared to the estimated line impedance at high frequency, the samples are still current-biased in the microwave regime. The color map of Fig. 2.4a shows the differential resistance dV/dI obtained by numerical derivation as a function of the dc bias current I and the microwave induced current $I_\mu \propto P_\mu^{1/2}$ at frequency $\nu = 6$ GHz. The supercurrent branch and the Shapiro steps (up to an index exceeding 10) appear as dark regions, with zero differential resistance. At large excitation amplitudes, Fig. 2.4a map is symmetric in I and the Shapiro steps' widths oscillate with the microwave excitation amplitude, producing a well-known pattern [104, 105, 108, 110, 111]. At small microwave current I_μ, the hysteresis appears through the asymmetry of Fig. 2.4a map with respect to I.

Strikingly, several low-index steps do not appear in the (positive) current branch corresponding to a current increasing from zero to above the critical current I_c. Individual V-I characteristics displayed in Fig. 2.4b-d clearly demonstrate that the absence of these steps stems from the voltage directly jumping from zero up to about $R_N I_c$, corresponding to the ohmic branch. Steps corresponding to voltages below $R_N I_c$ thus cannot be detected. The behavior discussed here is clearly distinct from the discussion of recent experiments on Josephson junctions based on topological insulator materials [108, 110, 111], in which

odd-index Shapiro steps are predicted to be absent [106, 107, 109].

Let us first focus on the behavior of the critical current as a function of the microwave current amplitude I_μ. In a current bias picture, the microwave irradiation adds adiabatically an oscillatory excursion I_μ to the bias current I, so that the current oscillates between $I - I_\mu$ and $I + I_\mu$ [102]. Switching to the resistive state then occurs at a lower critical current $I_c - I_\mu$. Once the junction has switched, it remains in the resistive state due to hysteresis. To first approximation, one expects then a linear suppression of I_c with increasing I_μ, as seen in Fig. 2.4a. We attribute the slight downward deviation from linear behavior to a small increase in the cryostat bath temperature at high microwave power. On the retrapping branch, a similar decay of the retrapping current I_r with the microwave current I_μ is observed. Here the electronic temperature is high compared to the bath temperature and varies with both the dc and ac bias, which plays a dominant role.

Tilted washboard potential in the presence of dissipation

In order to provide a quantitative description, we need to consider the energy relaxation from the normal metal electronic population. In the present temperature range, electron-phonon scattering is the dominant mechanism. The coupling power between electrons at a temperature T_e and phonons at a temperature T_{ph} is $P_{e-ph} = \Sigma U(T_e^5 - T_{ph}^5)$, where Σ is the material-dependent coupling constant and U is the metal volume. Considering a retrapping temperature T^* of 1 to 3 K, the related rate $\tau_{\mathrm{e-ph}}^{-1} \approx 0.16 \times T^3$ GHz in Au [115] is in the low GHz range ($\approx$ 0.4 GHz in J2 at $T^* = 1.4$ K for instance). In most of the frequency range investigated here, the thermal relaxation is thus slow compared to the microwave ($\tau_{\mathrm{e-ph}}^{-1} < \nu$) so that the electronic temperature can be considered as almost constant with time at a given (I,I_μ) bias point.

We consider a Resistively Shunted Junction (RSJ) model [95] with a current bias, complemented with a thermal balance. The time-dependent current $i(t) = I + I_\mu \sin(2\pi\nu t)$ through the junction is considered as the sum of the ohmic current v/R and the Josephson current $I_c \sin\varphi$, where φ is the phase difference across the junction:

$$i(t) = I + I_\mu \sin(2\pi\nu t) = I_c \sin\varphi + v/R. \tag{2.1.2}$$

The time-dependent voltage v relates to the time-derivative of the phase as $v(t) = \hbar\dot{\varphi}/2e$ from the second Josephson relation. From Eq. (2.1.2), the phase dynamics can be modeled as that of a massless particle of position φ in a *tilted washboard* potential $U(\varphi) = -\hbar[I_c \cos\varphi + i(t)]/2e$. The potential slope is proportional to the current bias $i(t)$: its average is thus determined by I and it oscillates with an amplitude given by I_μ. For large enough I or I_μ, the particle rolls down the slope. The Shapiro steps at voltage values $V_n = n\,hf/2e$ correspond to the particle hopping across n minima during one microwave period.

We can write the instantaneous Joule power:

$$p(t) = i \cdot v = I_c \frac{\hbar}{2e}\dot{\varphi} \sin\varphi + \frac{1}{R}\left(\frac{\hbar}{2e}\dot{\varphi}\right)^2. \tag{2.1.3}$$

The first term is the change of the Josephson energy. It is zero in average and does not contribute to the average power P dissipated over one cycle. Only the second term, which is the Joule power across the junction resistance, dissipates. It can be non-zero in average even though the average voltage V is zero.

In terms of heat balance, the dissipated power P is balanced by the electron-phonon coupling power P_{e-ph}. The related temperature elevation acts on the phase dynamics through the temperature dependence of the critical current following Eq. (2.1.1). Using Eqs. (2.1.2) and (2.1.3) and taking the volume U as a free parameter, we have numerically calculated the time-dependence of the phase, the dissipated power and the ensuing electronic temperature T_e for every (I,I_μ) bias point, which gives access to the related dc voltage drop V. Fig. 2.4e shows the calculated differential resistance for device J2's parameters. For the best fit, the volume U was chosen as 10 times the physical volume. This can be explained by both the inverse proximity effect in the leads in the vicinity of the N-S interface and the thermal conductance of the

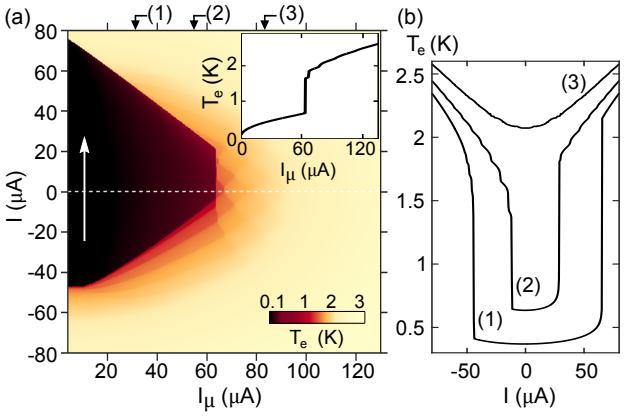

Figure 2.5: (a) Calculated electronic temperature T_e map corresponding to situation of Fig. 2, i.e. for device J2 at $T_{\mathrm{bath}} = 100$ mK. Inset: Line cut showing the electronic temperature at zero dc bias current as a function of the microwave current. (b) Line cuts of the map (a) showing the dependence of the electronic temperature as a function of the dc bias current I at different values of the microwave current indicated by arrows at the top of the map.

leads between the N island and the N metal regions of the leads. A semi-quantitative agreement for the differential resistance between Fig. 2.4a and 2.4e is readily seen.

The associated temperature map of Fig. 2.5a highlights the importance of dissipation in the ac phase dynamics in SNS junctions. Strikingly, the electronic temperature varies significantly as a function of the microwave current bias: the temperature increases from the bath temperature of 0.1 K up to above 2 K. On the first Shapiro step, the temperature is already of about 1 K. Even for zero dc current I and hence zero voltage V, the electrons in N are significantly overheated at large microwave drives, see Fig. 2.5a inset. The Shapiro steps structure appears also on the temperature map, as can be seen in Fig. 2.5a and more clearly in Fig. 2.5b as wiggles in every curve, especially the curve (2).

Both the data (Fig. 2.4a) and the calculations (Fig. 2.4e) exhibit a sudden drop of the critical current I_c as the retrapping current I_r reaches the border of the $n = 0$ Shapiro step (at a microwave current $I_\mu = I^*$ of about 0.04 in Fig. 2a). The numerical solution of the phase dynamics provides the explanation for this: for a zero dc current bias ($I = 0$), while at an ac drive below I^* the particle oscillates in a single washboard valley, above I^* it hops back and forth between two valleys. Although not causing any dc voltage over the junction, this produces dissipation similar to that of the $n = 1$ state, which is also revealed by the temperature map Fig. 2.5a.

In summary, this study evidences that electron over-heating is of paramount influence in the microwave response of Josephson junctions [94]. Exploring the microwave response of Josephson junctions involves variable electronic temperatures, which is of uttermost importance for the complete analysis of devices based on new materials like topological conductors. In a subsequent recent work to which I contributed [116], Benjamin Sacépé and coworkers exploited the very same approach to the microwave response of Josephson junctions incorporating thin flakes of Bi_2Se_3. Under isothermal conditions, the odd index Shapiro steps are predicted to be absent in topological Josephson junctions due to a 4π-periodic current-phase relation. However, all but the the $n = 1$ index Shapiro step are experimentally observed. Using the same analysis as above this non-observation of higher-order missing Shapiro steps can be explained by ac dissipation, and ensuing thermal poisoning.

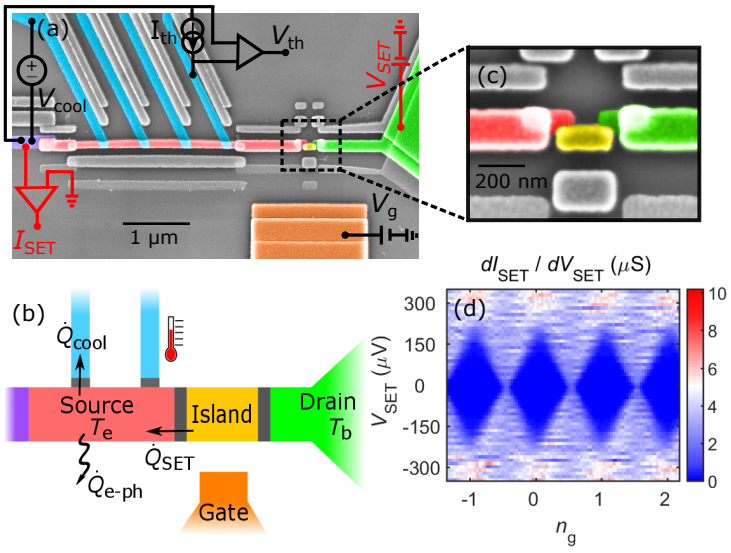

Figure 2.6: A single-electron transistor and the set-up for the heat transport measurement. (a) False-colored SEM image of the full device. The circuit in red indicates the charge transport set-up, while the black one stands for the heat transport set-up. (b) Schematic of the device, with the different elements shown in colors. (c) Zoomed-in view of the central part of the SET. (d) Differential conductance map of sample A SET at 50 mK against drain-source voltage V_{SET} and induced charge n_{g}.

2.2 Thermal transport in single electron devices

As device dimensions are reduced, electron interactions gain capital importance, leading to Coulomb blockade in mesoscopic devices in which a small island is connected by tunnel junctions. A metallic island connected to a source and a drain through tunnel junctions exceeding the Klitzing resistance $R_{\mathrm{K}} = h/e^2$ and under the influence of a gate electric field constitutes a Single-Electron Transistor (SET) [117]. The charging energy of the island by a single electron writes $E_{\mathrm{C}} = e^2/2C$ where C is the total capacitance of the island. It defines the temperature and bias thresholds below which single-electron physics appears. In the regime where charge transport is governed by unscreened Coulomb interactions, the question of the associated heat flow has been addressed by several theoretical studies [118–125]. The Wiedemann-Franz law is expected to hold in an SET only at the charge degeneracy points in the limit of small transparency, where the effective transport channel is free from interactions, and is violated otherwise.

In this experiment, led by Bivas Dutta in collaboration with our colleagues at Aalto University, we performed measurements of both the heat and charge conduction through a metallic SET, with both quantities displaying a marked gate modulation [87]. A strong deviation from the Wiedemann-Franz law is observed when the transport through the SET is driven by the Coulomb blockade, as the electrons flowing through the device are then filtered based on their energy.

Figure 2.6a is a colored scanning electron micrograph of one of the devices that we have investigated while Fig. 2.6b shows a schematics with the same colors for every element. It includes an SET with a drain made of a bulky electrode that is well thermalized to the bath. In contrast, the source of the SET is connected to its lead through a direct Normal metal-Superconductor (NS) contact, which thermally isolates it due to poor thermal conductivity of a superconductor at low temperature. In addition, four superconducting contacts form Superconductor-Insulator-Normal metal (SIN) junctions. As will be discussed below, the latter can be used either as electronic thermometers or coolers/heaters. Samples were fabricated by three-angle evaporation of Cu (30-45 nm), Al (20 nm) and again Cu (30 nm). The Al layer was oxidized in order to form tunnel barriers with the second Cu layer. Still, the drain, island and source are in the normal state

as the SET tunnel junctions are based on a short Al strip rendered normal by inverse proximity effect via a clean contact to a long normal (Cu) line [126]. The SET island was designed with a small volume in order to render the electron-phonon coupling negligible in the island.

We report here on two investigated devices with identical geometry but different drain-source tunnel resistance R_N of 164 kΩ (sample A) and 52 kΩ (sample B). Figure 2.6d shows the differential conductance at 50 mK as a function of both the SET bias V_{SET} and the average number $n_g = C_g V_g/e$ of electrons induced electrostatically by the gate potential V_g on the island. Here C_g is the capacitance between the gate and the island. Coulomb diamonds (in dark blue) are regions of zero current through the SET. Every diamond is centered around an integer value of n_g and defines a fixed charge state on the island. At zero bias, the charge conductance is thus vanishing, except in the vicinity of the degeneracy points at half-integer values of n_g. At these points, two charge states have the same energy and the conductance (for small barrier transparency) is half the high-temperature value, which is related to the fact that only these two states are involved. From the map, one can estimate a charging energy E_C of about 155 and 100 μeV for sample A and B, respectively.

Thermal balance

In the present work, our approach is to study the thermal balance in the source when it is heated or cooled. In every thermal measurement, we ensured that no current is flowing through the SET, so that pure heat transport can be considered. The thermal conductance of the SET is inferred from the heat balance in the source, and then compared to the electrical conductance measured in parallel.

We will consider here that the electron population of the source is in quasi-equilibrium at a well-defined (electronic) temperature T_e. This is justified as the mean electron escape time from this element is longer than the estimated electron-electron interaction time [127]. By heating or cooling electrons in the source, its electronic temperature T_e can be different from the temperature of the phonons thermalized at the bath temperature T_b. We achieve electronic thermometry by measuring the voltage drop across a current-biased NIS junction [70, 128, 129], the current set-point being chosen to be low enough in the sub-gap regime ($eV < \Delta$, Δ being the energy gap of the superconductor) to avoid any significant cooling.

Indeed, a current bias through a (pair of) NIS junction enables to cool electrons with respect to the phonons [130, 131]. This can be understood as a kind of selective evaporation: when the voltage drop is below the energy gap, only higher energy electrons can escape the normal metal. The maximum cooling power is obtained right below the gap in terms of voltage drop across one NIS junction. At a larger voltage, the usual Joule heating is recovered and electrons are heated above the thermal bath temperature.

The cooling and heating of the source electronic bath is illustrated for sample B in Fig. 2.7 left. Here one NIS junction to the source is used for thermometry while a second junction acts as a cooler used for cooling/heating. At a low cooler bias V_{cool}, the electronic temperature T_e is below the bath temperature T_b of 152 mK (indicated by a horizontal dashed line in Fig. 2.7 left) so that cooling is achieved. The maximum temperature reduction of about 50 mK is reached at a potential drop V_{cool} of about 190 μeV, close to the gap Δ for Al. A larger cooling is obtained when the gate potential is adjusted so that electron transport through the SET is blocked ($n_g = 0$) and so is thermal transport through it. At higher bias of the cooler ($V_{cool} > \Delta$), an electron overheating is obtained: $T_e > T_b$. Again, the electron temperature change (here an increase) is larger when the SET is blocked. The electron temperature at a fixed cooler bias but as a function of the gate potential is displayed in Fig. 2.7 right. Clear temperature oscillations are obtained, with an opposite sign for the electron cooling and the over-heating regimes. This demonstrates the contribution of the thermal conductance of the SET to heat transport.

In order to quantify the thermal conductance through the SET, we describe the thermal balance in the source following a thermal model depicted in Fig. 2.6b. In this model, the electron bath in the source receives the power $\dot{Q}_{cool}$ from the cooler junction, with a positive or negative sign corresponding to cooling or heating respectively. It can be calculated from [70]

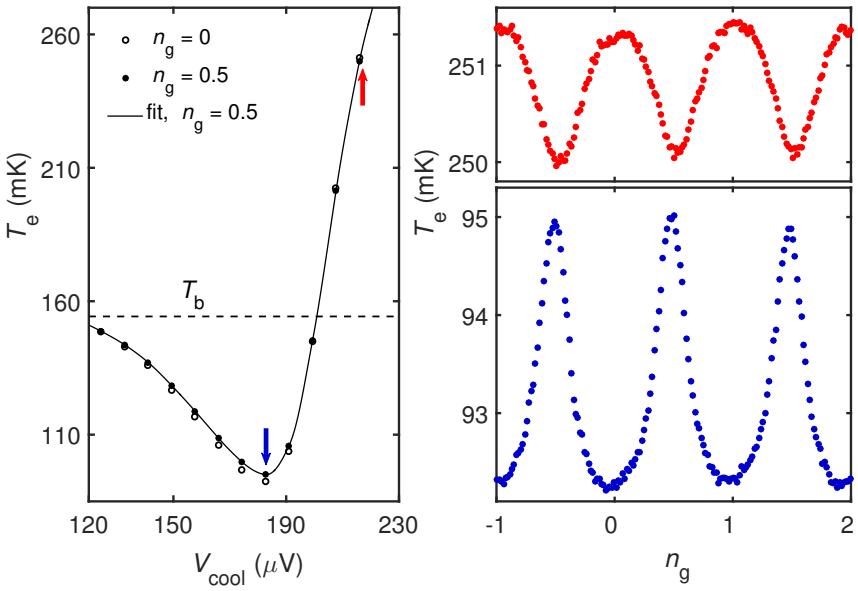

Figure 2.7: Left: Variation of electronic temperature T_e of sample B source with cooler bias voltage, at gate open ($n_g = 0.5$) and gate closed ($n_g = 0$) states, at a bath temperature T_b of 152 mK. The full line is a fit of the gate-open state data, see text. Right: Temperature modulation by the gate voltage expressed in terms of induced charge n_g in the heating regime (top) and in the cooling regime (bottom) at cooler bias points indicated by the blue and red arrows in the left plot.

$$\dot{Q}_{cool} = \frac{1}{e^2 R_{cool}} \int_{-\infty}^{\infty} (E - eV_{cool}) n_S(E) [f_{source}(E - eV_{cool}) - f_S(E)] dE - \dot{Q}_0, \tag{2.2.1}$$

where R_{cool} is the tunnel junction resistance of the cooler, $n_S(E)$ is the (BCS) density of states of the superconductor, $f_{source,S}(E)$ is the thermal energy distribution function in the source or the S lead of the cooler at respective temperatures T_e and T_S. The parasitic power $\dot{Q}_0$ takes into account imperfect thermalization of the electrical connections. The main energy relaxation channel for the source electrons is the coupling to phonons, with a power following $\dot{Q}_{e\text{-}ph} = \Sigma\mathcal{V}(T_e^5 - T_{ph}^5)$, where Σ is characteristic of the material, $\mathcal{V}$ is the volume, and T_{ph} is the phonon temperature here assumed to be equal the bath temperature [70]. Eventually, the SET transmits a power $\dot{Q}_{SET}$ to the source.

Let us first consider the gate-open position $n_g = 0.5$, where the two charge states involved in electron transport have the same electrostatic energy. Electron transport is thus (for small barrier transparency) unaffected by electron interaction and the Wiedemann-Franz law is expected to be valid. The power $\dot{Q}_{SET}$ can thus be calculated from the measured differential conductance for charge dI/dV at low bias. We use the thermal balance for the source electrons $\dot{Q}_{SET} - \dot{Q}_{cool} - \dot{Q}_{e\text{-}ph} = 0$ to extract the cooling/heating power $\dot{Q}_{cool}$. Here the electron-phonon coupling power $\dot{Q}_{e\text{-}ph}$ is calculated using the actual volume $\mathcal{V}$ and a parameter value: $\Sigma = 2.8$ nW μm^3 K^{-5}, close to the expected value for Cu. The parasitic power $\dot{Q}_0$ is found to be 0.1 fW in agreement with previous works [80].

The preceding analysis at the gate open state provides us with a full knowledge of the thermal behavior of the source, including all physical parameters for electronic cooling and electron-phonon coupling. We now assume that, whatever the gate potential is, the temperature of the superconducting leads of the cooler varies with the cooler's bias as determined above in the gate open case. The measured values of the source electronic temperature $T_e(n_g)$ are used to calculate the power flowing through the SET as $\dot{Q}_{SET} = \dot{Q}_{cool} + \dot{Q}_{e\text{-}ph}$ as a function of n_g. Considering the limit of a small temperature difference, the SET heat conductance is then calculated as $\kappa = \dot{Q}_{SET}/(T_b - T_e)$.

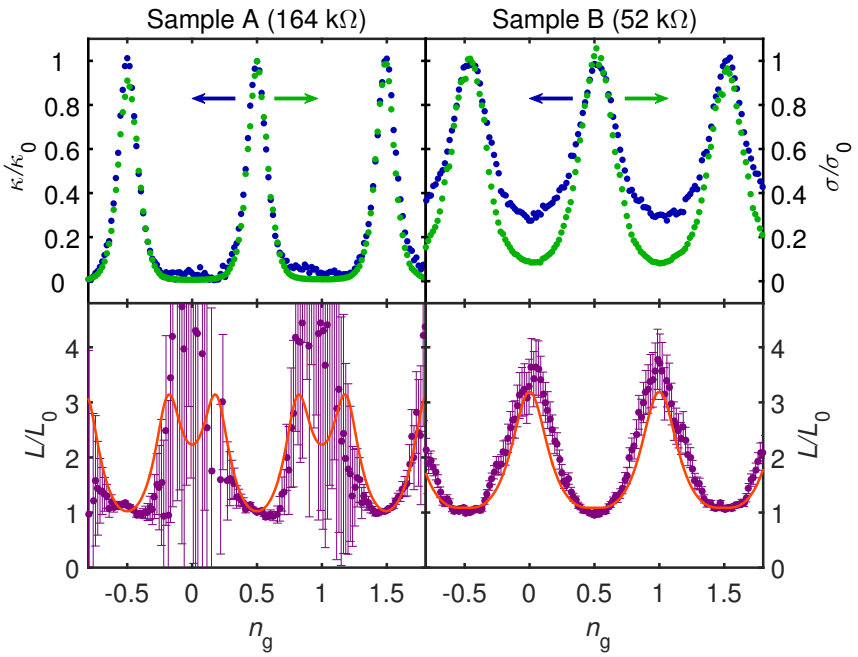

Figure 2.8: Top: Thermal (blue dots) and charge (green dots) conductances of the SET at a bath temperature of 132 mK (left, sample A) and 152 mK (right, sample B) in units of the conductances in the gate-open state κ_0 and σ_0. The thermal flow through the SET was calculated assuming that the Wiedemann-Franz law is fulfilled at the gate-open state. The charge transport was measured at a bias of 22.4 μV (sample A) and 19.2 μV (sample B). The heat transport data was acquired by cooling the source electronic bath by 30 mK (sample A) and 22 mK (sample B) below the bath temperature. Bottom: Lorenz ratio (purple dots) defined as L/L_0 where $L = \kappa/(\sigma T_\mathrm{m})$ for sample A (left) and sample B (right). The error bars are related to the uncertainty in temperature measurement. The Wiedemann-Franz law sets $L = L_0$. The red line is the theoretical prediction based on Ref. [124].

Electronic versus thermal conductance

Figure 2.8a shows both the heat conductance κ and the charge conductance σ for samples A and B, as a function of the gate potential. Both quantities were measured at the same bath temperature. An SET bias of about 20 μV and an electron cooling by about 25 mK were used for the charge and the heat transport measurements respectively. The charge conductance is plotted in units of the low-bias gate-open conductance σ_0. The heat conductance is plotted in units of the Wiedemann-Franz value in the gate-open state $\kappa_0 = \sigma_0 L_0 T_\mathrm{m}(n_\mathrm{g}{=}0.5)$. We use here the mean temperature $T_\mathrm{m} = (T_\mathrm{e} + T_\mathrm{b})/2$ so that a linear response is expected in the Wiedemann-Franz regime even for the case of a significant temperature difference $T_\mathrm{e} - T_\mathrm{b}$.

For both samples A and B, the charge and heat conductances oscillate with n_g. In the case of sample A (top left), the two conductances mostly overlap over the full gate potential range. Close to the gate-closed state, the two conductances seem to deviate one from the other but their absolute values are small. In contrast, sample B exhibits a clear deviation from the Wiedemann-Franz law. At the gate closed state, the heat conductance clearly exceeds the charge conductance multiplied by $L_0 T$.

In order to get more insight, let us now consider the Lorenz factor defined as L/L_0 with $L = \kappa/(\sigma T_\mathrm{m})$. The Wiedemann-Franz law sets a Lorenz factor equal to unity. In contrast, for sample B the Lorenz factor (Fig. 2.8 bottom right) oscillates between 1 at gate-open state and about 4 at gate closed state. This is the main result of this work. Sample A shows essentially the same behavior over the gate potential range where it can be accurately determined whereas error bars are very large in the vicinity of the gate-closed

state due to vanishingly small conductances. We obtained similar results for the whole range of bias points of the cooler, both in the cooling and the heating regimes.

The physical origin of the violation of the Wiedemann-Franz law resides in the energy selectivity of electron transport through an SET. As a consequence of this, the population of electrons flowing through the SET is non-thermal. For instance, at the gate-closed state, only electrons with an energy (counted from the Fermi level) above the charging energy E_C contribute to the zero-bias SET conductance. These electrons obviously carry the same (electron) charge but a higher energy. Thus the heat conductance does not decay due to interactions as much as the charge conductance does and the Lorenz number exceeds its basic value L_0. Electron co-tunneling can counter-balance this, as it involves electrons with an energy close to the Fermi level. The cross-over to the co-tunneling regime shows up at the gate-closed state as a maximum of the Lorenz factor at a temperature $T \approx 0.1E_C/k_B$ [124].

We have calculated the theoretical Lorenz factor for our samples using the theory of Ref. [124]. Figure 2.8 bottom shows as full lines the calculated Lorenz factor in parallel with the experimental data. As for parameters, we used the calculated values of $k_BT/E_C \approx 0.06$ and 0.12 for sample A and B respectively and the measured values of the SETs conductance. The theoretical prediction and the experimental data match very well, within error bars. For sample A, the calculated Lorenz number shows a relative minimum in the gate-closed state, which cannot be checked in the experiment due to experimental uncertainties.

To conclude, this work demonstrates that the heat transport through an SET can be driven by a gate potential, making the SET a heat switch. The celebrated Wiedemann-Franz law is strongly violated away from the charge degeneracy positions. Our experimental data agree very well with theoretical predictions. As a prospect, investigating SETs where the island is a quantum dot could exhibit new thermo-electric effects driven by a single energy level [68].

Chapter 3

Bridging the gap between scanning probe and device physics

Device physics and scanning probe microscopy studies are usually the playgrounds of very different scientific communities, in terms of experimental techniques. However, the STM tunnel junction itself can be seen as a device, with spatially tunable characteristics. Our group at Néel has been working in the past years (decades...) at the interface between both fields, principally along two directions: (i) the scanning probe inspection of the local properties of solid-state devices (see [132, 133] for two results obtained prior to my recruitment), and (ii), more recently, creating devices with one contact being the STM tip, in combination with other control knobs such as a gate electrode. The latter is however still at the level of a project.

This chapter mainly describes the Grenoble cryogenic AFM-STM setup built in 2009, along with three selected results obtained with this instrument on the local properties of graphene [134–136]. The planned integration of a UHV surface preparation chamber to the STM setup, which will allow to extend our work beyond inert surfaces, is described in the Perspective chapter.

3.1 Cryogenic combined AFM-STM

3.1.1 The scanning probe microscope

While a postdoc at Tokyo University, part of my work was devoted to conceiving and building a new cryogenic STM that would allow for coarse xy positioning the sample. The PhD dissertation of A. Wachowiak was a very useful document for this purpose. The Pan-design [21] was chosen for the coarse Z approach of the tip. For XY positioning the sample, I used commercial piezoelectric stacks, with orthogonal polarisation from one layer to the next and independent contacts. Thereby, the same stack could move either along X or Y, depending on which layers of the stacks the voltage was applied to. The sample was pressed against the stacks by a spring from top, but was not guided along a peculiar axis, that is, is was free to move in the XY plane. This solution is very compact (it is chosen by several commercial suppliers, such as CreaTec) and suited the requirement to fit the STM into a diameter of less than 26 mm, as anticipated for applications in high magnetic fields. The STM that I built in Tokyo produced good topographic images, although it was tested inside a rather poorly vibration-isolated helium cryostat (Fig. 3.1a,b). However, it was never inserted into the dilution-refrigerated setup I had designed it for. Also, although the coarse Z motion (tip approach/retract) was very reliable, the XY motion was not sufficiently deterministic. The sample stage eventually always drifted to a position where it would get stuck.

When starting my research project at Néel in 2008, I concluded from my previous experience that the X and Y coarse motions have to be separated. We designed the sample positioning to occur via two orthogonal

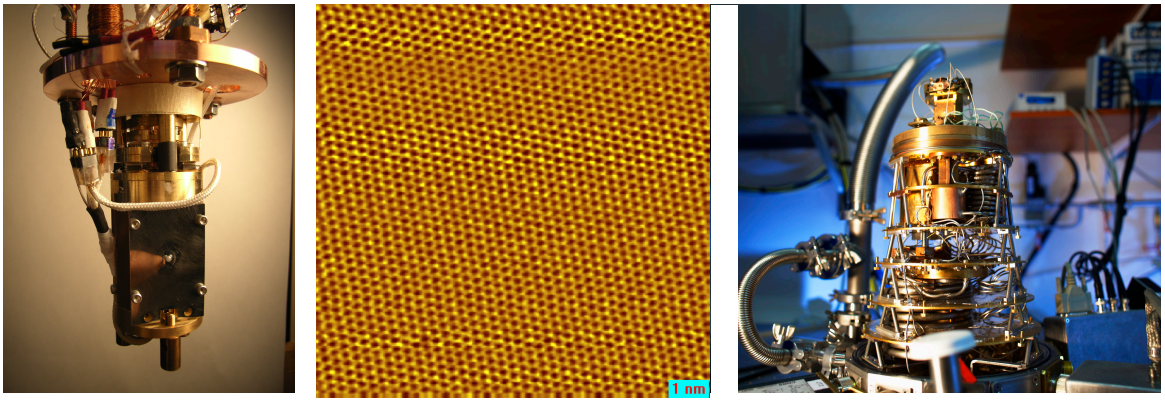

Figure 3.1: **Left:** STM head developed at the University of Tokyo. **Center:** Atomically resolved topography on graphite obtained at 4K with this instrument. **Right:** Inverted dilution cryostat set up in Grenoble, with the combined AFM-STM on top of the cold plate.

uniaxial translations: a frame moving along a groove. This frame then carries the sample holder, which itself can move orthogonally, along a groove on the first frame. The obvious drawback here resides in the larger lateral dimensions, of about 65 mm here. Because the *sionludi* has a wide cold stage and because we did not target high magnetic fields, this was not a critical issue. The main difference with the frequently used geometry involving a stack of orthogonal positioners (e.g. Attocube) is that the above-described XY coarse motion system sample is very flat and thus less prone to vibrations.

The combined AFM-STM that allowed obtaining the results presented in this chapter was constructed in 2009, principally by Sylvain Martin and myself. The AFM operation was significantly improved a few years later, by Sayanti Samaddar. Detailed descriptions of the construction and the setup can be found in both their theses. In the remainder of this section, I will simply highlight a few peculiar features and unpublished results.

3.1.2 Length extension resonator-based combined AFM and STM

In low-temperature AFM, quartz tuning forks are the usual choice for the mechanical-to-electrical transduction of the tip-sample interaction. In the early 2000's quartz length extension resonators (LERs) were proposed as an alternative [137, 138] (Fig. 3.2a). These are more compact than usual tuning forks and resonate usually at 1 MHz or above. They are extremely stiff in the z direction, perpendicular to the sample surface, with a $k = 10^6$ N/m. This is a drawback in terms of force sensitivity for AFM operation, but an advantage for subsequent STM, and led us to chose this solution for our AFM-STM. A detailed comparison of the relative merits of the tuning fork and the LER can be found in [139] and in the thesis of Sayanti Samaddar.

Because of the high operation frequency, actuation and sensing of the LER requires some precautions. Dedicated electronics allow for simple self compensation of the large and strongly temperature-dependent stray capacitive currents. In our setup, we apply the excitation signal identically to two close-lying and similar wires throughout the cryostat, one leading to the LER, the other one being a dead end in the vicinity of the SPM. The measured signal is the difference of the currents to both sides, which ideally leaves over the sole contribution of the LER resonance (Fig. 3.2e). This self-cancellation has the great benefit of being independent of the SPM temperature since the capacitances of both wires vary similarly. Removal of residual contributions from stray capacitances is achieved by fine-tuning of the relative phase and amplitude of the AFM current amplifications. Further, we also observed that only two wires are enough for both and simultaneous AFM and STM operation. This is not the case in tuning fork-based AFM-STMs, in which

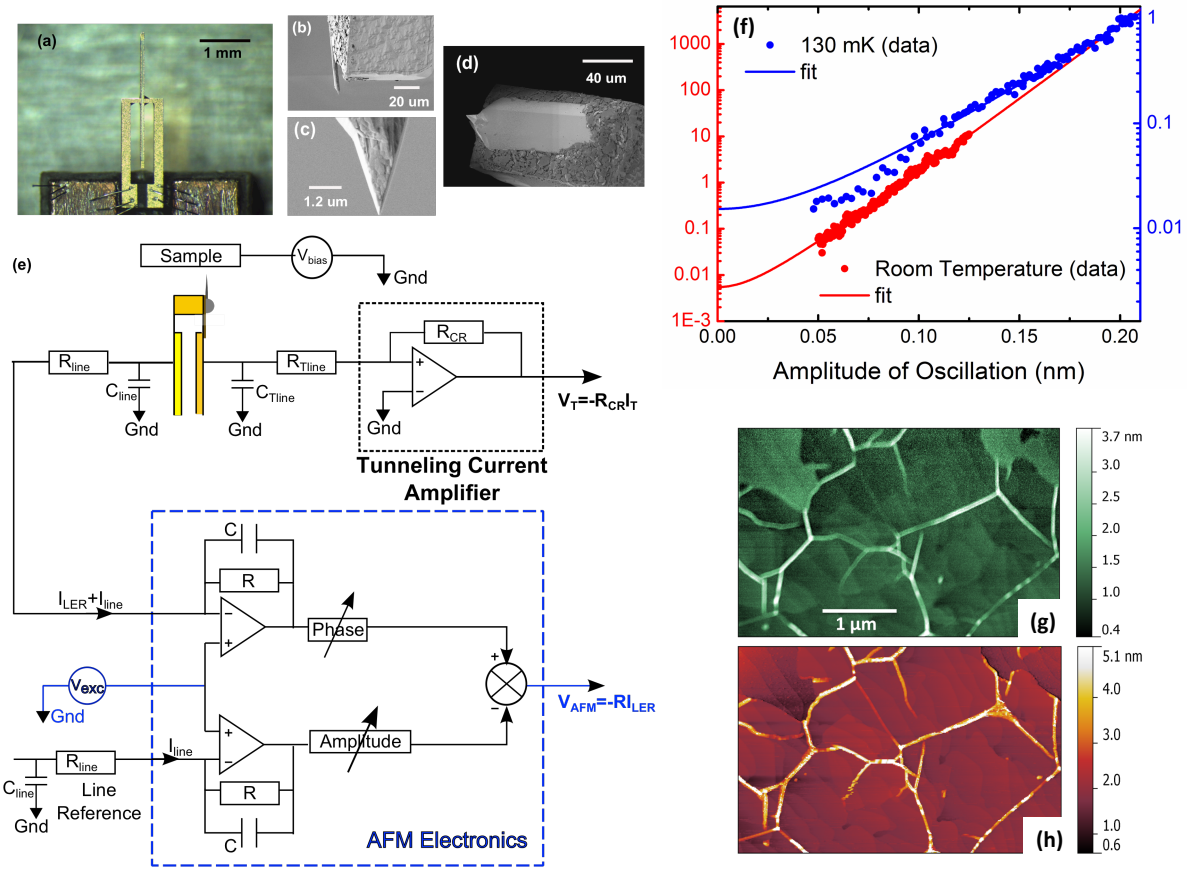

Figure 3.2: (a) Optical image of the LER. The two side electrodes are microbonded to the supporting chip. (b) SEM image of a 4 μm tungsten wire glued on the side of the top electrode of the LER. (c) A zoomed in view of (b) showing the shape of the tip, defined by FIB-etching. (d) SEM image of a commercial PtIr-coated silicon cantilever and tip glued on the top of the top electrode of the LER. (e) Schematics of the electronic readout and compensation setup. (f) Variation of the tunneling current (in units of pA) with the amplitude of oscillation of the LER at room temperature and at 130 mK, respectively. The data are fitted with a modified Bessel's function of zeroth order. (g) AFM topograph of the surface of CVD grown epitaxial graphene on iridium(111) at room temperature (Δf_{set}= 5Hz, A_{set} = 700 pm, V_{bias} = 0.8 V). (h) STM topograph over the same region recorded in a consecutive scan (I_{set} = 100pA, V_{bias} = 0.8 V). The continuous ridges running all over surface are wrinkles of the graphene sheet. The region on the top left of each image shows uncovered iridium having undergone atmospheric oxidation.

the STM wire cannot act as the resonator counter-electrode. This difference is due to the very different resonance frequency regimes of both types of resonators.

The combined operation of the STM and AFM modes allows for a variety of experiments. For example, when the tip is brought into tunneling contact, measuring the tunneling current as a function of the LER oscillation amplitude allows for calibrating directly and in situ the LER amplitude of oscillation. This oscillation amplitude dependence of the tunnel current is due to the non-linear dependence of the tunneling current on the tip height, and can be captured by a simple Bessel-type integral, leading to the fits in Fig. 3.2f. Further, the combination of AFM and STM topographies at the same location gives interesting insights into the surface properties, as exemplified by Figs. 3.2g,h. The region which appears as a protrusion in the top left corner of the AFM image appears actually lower than the surroundings in the STM topography. This region is graphene-free iridium, covered by a non-conductive oxide (IrO). The stronger tip-sample

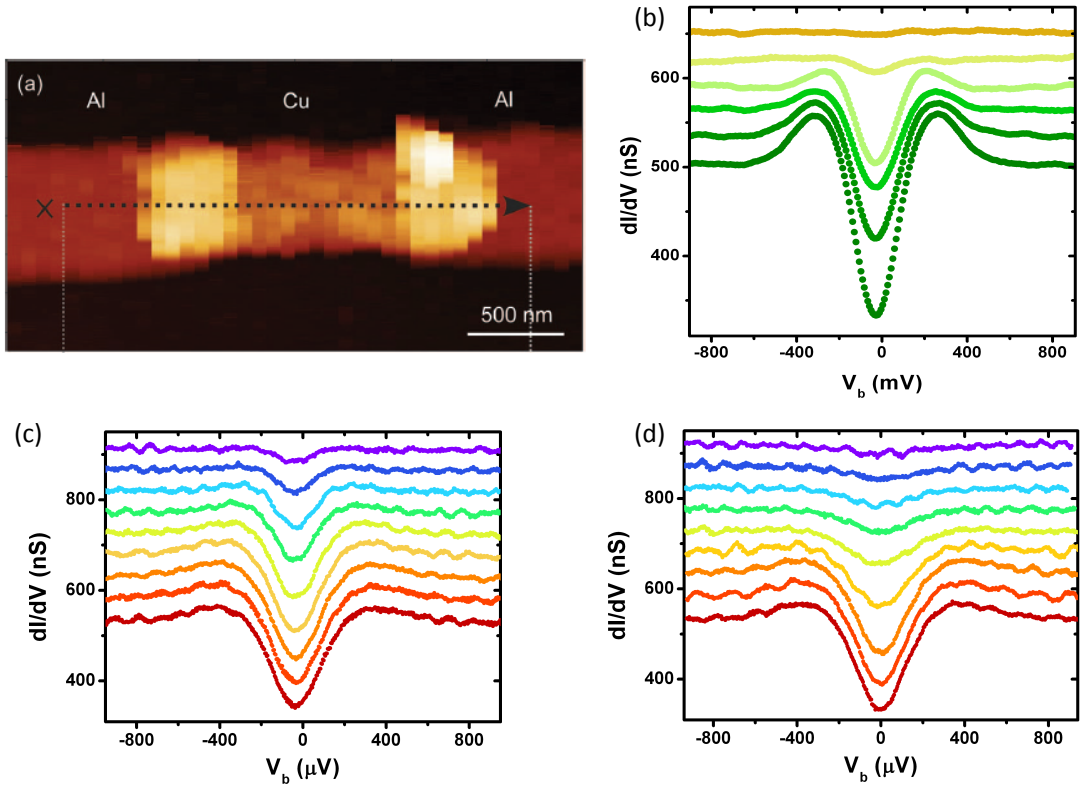

Figure 3.3: (a) Low temperature AFM image of an Al-Cu-Al Josephson junction. (b) Tunneling spectroscopies on proximized Cu at increasing distances from the interface. At a distance of 100 nm, the induced gap becomes unobservable, in striking contrast with the critical current of several μA of the Josephson device. (c) Effect of increasing current bias in the SNS device on the tunneling spectroscopies near the initial position of (b) (at zero magnetic field). (d) Effect of increasing magnetic field on the same (at zero current bias).

interaction in the STM mode leads also to the deformation of some structures, such as seen at the point of convergence of three graphene wrinkles in the top right corner of both images.

Eventually, we must also stress one of the main drawbacks of the LER: its symmetry properties and extremely small mass make the LER's quality factor rather sensitive to the mass imbalance caused by the tip attached to one prong. This has obliged us to test several strategies for attaching tips, which need to be both sharp and electrically conductive/connected (Figs. 3.2b-d). Up to date, individually focussed-ion-beam-shaped tungsten tips appear as the most viable solution, although their preparation is quite time consuming and the electrical contact is sometimes lost at low temperatures.

3.1.3 Spectroscopy of the superconducting proximity effect

Determining the local value of the proximity-induced pairing amplitude at the vicinity of a transparent NS interface has been one of the main motivations that led Hervé Courtois to construct a dilution-refrigerated STM in Grenoble in the late 1990's. This was achieved with his student Norbert Moussy, who was able to determine the proximity-induced gap near the gold-niobium interface [140], in good agreement with the Usadel formalism (see also [141]).

Thereafter, the most obvious follow-up experiments were to extend to above measurements to (i) incorporate a current or a quantum phase bias across the diffusive normal island between two superconductors, and (ii) consider a non-diffusive (ballistic) normal conductor, such as a quantum dot. This initially im-

pulsed the development of the combined AFM-STM technique, in order to being able to locate single phase- or current-biased devices, on an insulating substrate. Eventually, both the phase-bias- and the superconducting quantum dot spectroscopy experiments were tackled a few years later by P. Joyez and coworkers [24, 101]. Here, a few complementary and unpublished results obtained by Sylvain Martin on local tunneling spectroscopies on current-biased SNS junctions will be presented.

One of the main difficulties of the Grenoble STM experiments on SNS devices was due the unfortunate choice of copper (rather than silver, as used in [101]) as the normal conductor. As we found out after significant efforts, even in an extended 10 nm-thick copper thin film on top of superconducting aluminum, the proximity effect is significantly suppressed at the surface [142], possibly due to the quick growth of a magnetic oxide on copper under ambient conditions. This is somewhat surprising because Cu has excellent properties as an N link in SNS Josephson junctions, while the presence of a magnetically active surface should produce pair breaking.

Figure 3.3a shows an AFM image obtained by T. Quaglio on an Al-Cu-Al junction [133]. In this device, the superconducting gap is nearly immediately suppressed when the tip moves from the Al to the Cu surface. In a similar device, Sylvain Martin succeeded in observing a more progressive variation of the induced gap, when moving to the Cu (Fig. 3.3b). Interestingly, it was possible to observe the evolution of the induced gap as a function of the applied current across the Josephson junction (Fig. 3.3c). When the critical current is reached, the induced gap disappears. The same effect is obtained by applying a magnetic field at the same location (Fig. 3.3d). This is not surprising because in the Hamiltonian of the (inhomogeneous) superconducting state, the superfluid velocity and the vector potential $\vec{A}$ appear on equal footings.

3.2 Charge disorder and screening in graphene

The difficulties encountered in working on non-inert surfaces using scanning probe techniques and without a preparation chamber encouraged us to develop an activity on graphene surfaces and devices. As of 2010, we started collaborating with J. Coraux, who at that time started growing graphene on thin film iridium(111) at Néel, which led to three joint publications [134, 136, 143]. A few years later, we were ready to move from bulk samples to graphene devices [135, 136].

3.2.1 Charge disorder in graphene on Ir(111) upon molecular intercalation

At the time of Sylvain Martin's first experiments on Gr/Ir(111), M. Crommie's group had recently published on the *Origin of spatial charge inhomogeneity in graphene* [144]. This paper not only demonstrated the mapping of the charge puddles by STM, but further associated the observed charge inhomogeneities to the presence of individual charge inhomogeneities below the graphene. These were identified by surrounding LDOS fringes (Friedel oscillations), which became visible at energies off the Dirac point and displayed the expected spatial periodicity $\propto (E - E_D)^{-1}$. Eventually, these authors highlighted the total absence of correlations between the doping landscape and neither the topography, nor its curvature. This was at that time a particularly hotly debated issue, in which the mainstream scenario of charge density inhomogeneities induced by isolated charges in the substrate [145] was challenged by more exotic scenarios, calling for possible effects of the graphene curvature on the local doping [146–148].

In Sylvain Martin's work, we demonstrated the coexistence of charge puddles and topographic ripples in graphene decoupled from the Ir(111) substrate it was grown on. We show the topographic corrugations and the charge disorder to be locally correlated. This sounds at first sight as it was challenging the findings of the Crommie group in a different system. However, here the situation in graphene on Ir(111) is quite different and the observed correlation appears as a result of the intercalation of molecular species. More interestingly, from the analysis of quasi-particle scattering interferences observed by STM, we determine

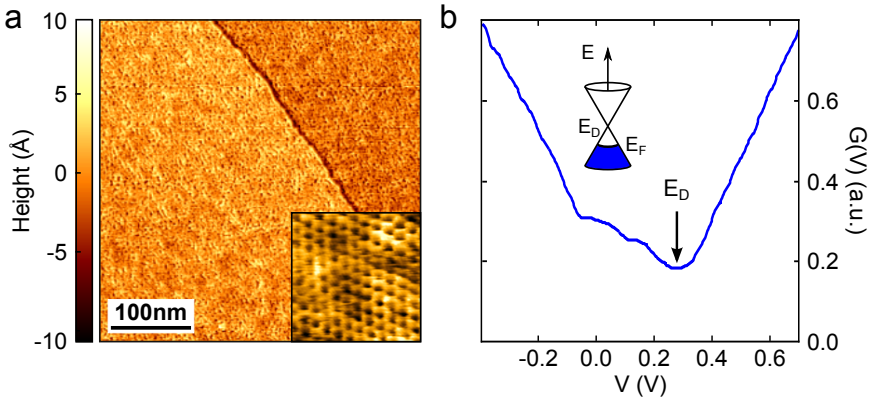

Figure 3.4: (a) Scanning tunneling micrograph on graphene on Ir(111). The image size is 400×400 nm^2, tunnel current $I = 1$ nA, bias voltage $V = 0.57$ V). The atomic step in epitaxial Ir(111) covered by graphene is 2.5 Å high. Inset: zoom-in (2.3×2.3 nm^2) atomic resolution image, $I = 1$ nA, V=0.01V. (b) Local tunneling spectroscopy $G(V) = dI/dV$. The Dirac point ($eV = E_D$, arrow) is defined by the minimum of G.

a linear dispersion relation, demonstrating that graphene on a metal can recover its intrinsic electronic properties. The measured Fermi velocity $v_F = 0.9 \pm 0.04 \times 10^6$ m/s is lower than in graphene on dielectric substrates, pointing to a strong screening of electron-electron interactions in graphene by the nearby metallic substrate.

The experiment is conducted using the home-made scanning probe microscope described above, at 130 mK. Local tunnel conductance data were obtained using the lock-in technique ($V_{AC} = 6$ mV, $f = 407$ Hz). Samples are heated to 70°C while pumping the chamber and during cryostat cool-down, in order to avoid cryosorption of residual gases. The studied sample is graphene prepared by chemical vapor deposition (CVD) on epitaxial Ir(111) under ultra-high vacuum (UHV), as described in [149]. The samples are exposed to air between the growth and STM inspection. This produces a decoupling of the graphene from its metallic support by oxygen intercalation, transforming the moiré pattern into a disordered topographic landscape [143]. Figure 3.4(a) shows the topography of graphene on a plain Ir atomic terrace. A disordered topographic landscape with a typical rms roughness $\sigma_z \approx 50 - 100$ pm is observed, comparable to the corrugation of graphene on SiO_2 [144]. While the usual moiré pattern is absent, atomic resolution is routinely achieved, demonstrating the cleanliness of the surface.

Mapping the local doping level

The electronic LDOS can then be accessed in STM by the measurement of the local tunneling conductance $G(V) = dI/dV$. The tunnel spectra display a V-shape (Fig. 3.4(b)), characteristic of the density of states of graphene and similar to data observed by STS on exfoliated graphene on SiO_2 [150, 151]. The voltage V_{min} at the conductance minimum has been identified in previous works [144] as the charge neutrality point, that is, the Dirac point in graphene at energy $E_D = eV_{min}$. The value of E_D reflects the strength of the local graphene doping [144, 146, 151], which is p-type here. A dip of width of about 20 meV is also present around zero bias, which is frequently reported in STS studies on graphene [150–152] and will not be discussed in this work. We have measured a series of high-resolution conductance maps at low temperature. At each position $\mathbf{r}$ of a tunnel conductance map, the Dirac point energy E_D is extracted using a parabolic fit around the minimum of G. The average doping (sample dependent by ±10%) is found to be $E_D^0 = 340$ meV in Fig. 3.5a. This is somewhat larger than that of the same system in undisrupted UHV conditions (≈ 100 meV) [153], and lesser than that achieved therein by controlled and exclusive intercalation of oxygen (≈ 500 meV) [154].

The map shown in Fig. 3.5a pictures the spatial inhomogeneities of E_D around its mean value, forming a smooth landscape of charge puddles, of about 8-9 nm in diameter. From the relation $E_D^2 = (\hbar v_F)^2 \pi n$ [155], where $\hbar$ and v_F are the reduced Planck constant and the Fermi velocity respectively, we deduce the distribution of the charge carrier density n (Fig. 3.5b), where we take $v_F = 0.9 \times 10^6$ m/s as will be discussed later. Notably, the standard deviation $\sigma_n \approx 1.2 \times 10^{12}$ cm^{-2} is slightly higher than in graphene exfoliated on SiO_2 ($\approx 4 \times 10^{11}$ cm^{-2}) [144]. We further note that the puddle radius is very close to the Thomas-Fermi screening length which can be evaluated [155] as $\lambda_{TF} \approx 1.1 \times n^{-1/2} \approx 3.4$ nm.

Doping versus corrugation

We now focus on the comparison between the Dirac point distribution and the topography. Since only topographic variations at length scales similar or larger than the typical puddle size can correlate with the charge inhomogeneities, we filter out the topographic maps from structures of dimensions below half the mean puddle size. Figure 3.5a shows the superposition of an $E_D(\mathbf{r})$ map (color scale) along with the long wavelength-pass filtered topography $z(\mathbf{r})$ recorded at the same position (3D profile). A very high degree of correlation between doping and topography is readily seen. We have quantified this by calculating the normalized cross-correlation function

$$\chi_{z-E_D}(\mathbf{r}) = \sum_i E_D(\mathbf{r_i} - \mathbf{r}) \times z(\mathbf{r}) / (\sigma_{E_D} \times \sigma_z)$$

of the two data sets. The local cross-correlations $\chi^0_{z-E_D}$ between $z(\mathbf{r})$ and $E_D(\mathbf{r})$ are in excess of 60 % in large area maps (Fig. 3.5c). These correlations are independent on the region chosen, but are enhanced in maps with dimensions much larger than the typical puddle size. When correlating spectroscopic maps with topography, one also has to recall that in constant-current STM mode a LDOS variation will lead to a change in the tip-sample distance z. This can misleadingly induce phantom topographic features. We have carefully analyzed such possible LDOS contribution to the topography and shown them to be much smaller than the observed corrugation.

The above analysis therefore leads to the conclusion that disordered graphene on a metallic substrate displays a strong local correlation between doping and topography. Several scenarios can be considered for this observation. A contribution of curvature effects [147, 148, 156] could for example be anticipated. In the present system, the theoretically expected contribution of this effect is however nearly two orders of magnitude below the observed amplitude of the doping disorder, as we analyzed in a correspondence with M. Polini and coworkers. The graphene doping could further be due to graphene-metal distance dependent charge transfer from the metallic substrate due to finite electronic wave function overlap. Calculations of this effect [157] yield a qualitatively correct description, including the correct sign of $\chi^0_{z-E_D}$ for graphene on iridium. Scanning probe measurements at the boundary between coupled and uncoupled graphene on iridium have however shown the graphene to iridium distance to increase by about 1 nm upon decoupling [143], a distance at which the above scenario would have negligible contributions. The most likely explanation of the doping bases on the presence of molecular species intercalated between the graphene and its substrate [143, 154]. Locally enhanced accumulation of negatively charged intercalates induce a reduction of the Fermi level, that is, enhanced p-doping in the graphene. It has indeed been shown that oxygen intercalation at high temperatures could reversibly modify both the graphene doping and its hybridization to the substrate [154].

Determination of the band structure from Fourier-transform STS

In order to obtain a more microscopic understanding of the role of the local electrostatic environment as electron scattering centers, we have tracked the wave vector $\mathbf{k}$ distribution of interference patterns in the Fourier transforms of LDOS maps. The evolution of the dominant $\mathbf{k}$, relative to the Brillouin zone corner, as a function of the energy level of each map then reflects the dispersion relation of the scattered

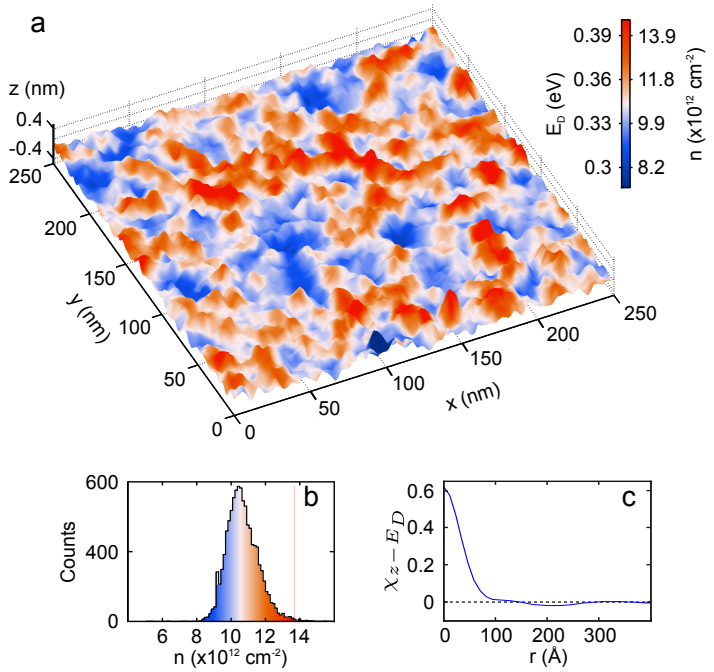

Figure 3.5: (a) Dirac point map (color code) superimposed with a 3D plot of the long-wavelength topography. Image of 250×250 nm^2. (b) Carrier density distribution extracted from (a) (see text). (c) Angular average $\chi_{z-E_D}(|\mathbf{r}|)$ of the cross-correlation function (see text) between the above E_D and topography maps.

electrons. In graphene, both the large k intervalley and the small k intravalley scatterings have been observed by this technique [158]. For intravalley scattering, the wave vector transfer $\mathbf{q}$ links two points of the circle resulting from the intersection of a given Dirac cone and a constant energy plane. A particular characteristic of graphene is the suppression of low-energy backscattering [159]. One therefore expects a smooth distribution of q between 0 and $2k_F$ for intravalley scattering, seen as a disk in reciprocal space.

In our data, the LDOS maps at energies far from E_D^0 display clearly resolved structures at length scales smaller than the typical puddle size (Figs. 3.6a–f). Further, the size of the observed features decreases with increasing $|E - E_D^0|$. The Fourier transform maps display a disk-like structure (Fig. 3.6g) from which we extract $k = q_{max}/2$ at each energy (Fig. 3.6h). The radius $q_{max}/2$ of the interference patterns is defined as the inflection point of the angular averaged Fourier intensity, that is, the minimum of its smoothed derivative. This criterion produces the $k(E)$ dispersion with least noise but also slightly overestimates the wave vectors involved by adding a constant shift [144] to the detected values of q, which results in the linear dispersion bands crossing at $k > 0$ in Fig. 3.6h.

The experimental dispersion relation at small k has the features of graphene close to the Dirac point, evidencing thus the scattering mechanism at work as intravalley. A fit by the linear dispersion relation of graphene $E = E_D^0 \pm \hbar v_F k$ (Fig. 3.6h) yields $v_F = 0.90 \pm 0.04 \times 10^6$ m/s. In unhybridized graphene, v_F is a sensitive probe of the strength of electron-electron interactions [155, 160], which can be screened by a large dielectric constant ϵ environment. While a Fermi velocity $v_F = 2.5 \times 10^6$ m/s has been reported on a low-ϵ quartz substrate [161], it decreases to about $1.1 - 1.4 \times 10^6$ m/s on SiO_2 [144, 150], with a limiting value of about 0.85×10^6 m/s expected for infinite screening [161, 162]. The present system can actually be envisaged as graphene on a dielectric substrate with divergent ϵ. In spite of the rather high doping level, the Thomas-Fermi screening length λ_{TF} remains larger than the graphene-iridium distance. One can thus reasonably assume the substrate screening to dominate over the intrinsic screening of the graphene, although highly doped. With the above analysis it is thus seen that (i) the linear dispersion relation of graphene decoupled from a metallic substrate survives at both positive and negative energies

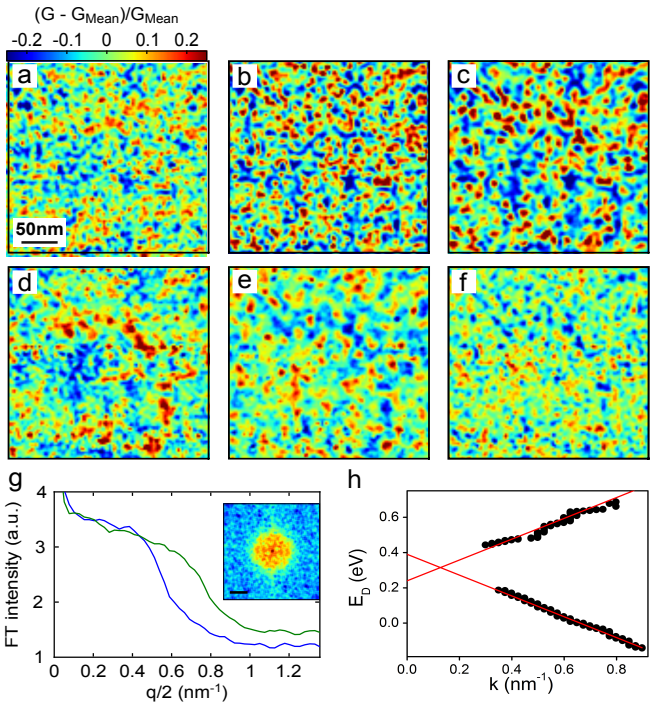

Figure 3.6: (a) - (f) $G(\mathbf{r}, E)$ maps for $E = -185; 15; 125; 345; 555$ and 700 meV respectively. The color scale is set to cover fluctuations of ± 25 % with respect to the average G at a given E. As the Dirac point is approached, the islands size can no longer be resolved. (g) Power spectral density from angular averaging of Fourier transform of (b) (blue) and (c) (green). The inset shows the Fourier transform of (b). The scale bar is 0.5 nm^{-1}. (h) Energy - wave vector relation extracted from Fourier analysis of the density of states maps at energy E. The dashed lines are fits to the linear dispersion relation of graphene, yielding $v_F = 0.90 \pm 0.04 \times 10^6$ m/s and $E_D^0 = 0.32$ eV.

and (ii) electron-electron interactions in the graphene sheet are strongly screened.

In conclusion, this study demonstrated that CVD-grown graphene can be completely decoupled from its metallic substrate, displaying local properties that are very similar to graphene on a dielectric substrate like SiO_2. The main contrasting feature with respect to the latter system is that the dopants here indeed have a topographic signature. We observe a linear electronic dispersion relation, demonstrating unhybridized graphene with highly screened electron-electron interactions. While the coupling constant of graphene, that is, the ratio of interaction to kinetic energy $\alpha \propto (\epsilon v_F)^{-1}$, is of order unity in unscreened graphene [160], studying graphene in a large and adjustable dielectric constant environment could allow for tuning the *fine structure constant* α.

3.2.2 Charge puddles in graphene near the Dirac point

As discussed above, the charge carrier density in graphene on a dielectric substrate such as SiO_2 displays inhomogeneities, the so-called charge puddles. Because of the linear dispersion relation in monolayer graphene, the puddles are predicted to grow near charge neutrality, a markedly distinct property from conventional two-dimensional electron gases. By applying a variable gate potential, while performing scanning tunneling microscopy/spectroscopy on a mesoscopic graphene device, we directly observe the puddles' growth, both in spatial extent and in amplitude, as the Fermi level approaches the Dirac point. Self-consistent screening theory provides a unified description of both the macroscopic transport properties and the microscopically observed charge disorder.

Electrostatic screening in 2D electron gases

Electrons in graphene are subjected to a disordered potential created by random charged impurities, either adsorbed on the graphene or buried in the substrate, leading to charge puddles [144, 146, 155, 163–166]. Scanning probe microscopies have in particular strongly contributed to unraveling the puddles' spatial properties and have challenged different theories about their origin [144, 146, 163]. Charge puddles are usually thought of as a limitation to the extent the charge neutrality point can be approached macroscopically, thereby also limiting possible device performances. However, the behavior of the puddles itself unveils the fascinating electronic properties of graphene and, more generally, Dirac materials.

Electrostatic screening in two dimensions (2D) has a counterintuitive behavior. Thomas-Fermi screening entails a characteristic length scale q_{TF}^{-1}. Unlike in three dimensions, the Thomas-Fermi wave vector q_{TF} in a 2D electron gas (2DEG) is proportional to the density of states at the Fermi level. As a consequence, q_{TF} is energy- and thus carrier density-independent in conventional 2DEGs, while q_{TF} is proportional to $k_F = \sqrt{\pi n}$ in graphene and other Dirac materials. This has the important consequence that the unscreened potential created by a charged impurity in a medium with dielectric constant κ, $V(q) = e^2/2\kappa\epsilon_0 q$ and the screened potential $\tilde{V}(q) \propto (q + q_{\mathrm{TF}})^{-1}$ are identical within a multiplicative constant [155]. In other words, near charge neutrality local inhomogeneities in the screened potential can be arbitrarily large. Further, a rough estimate of the lateral extent of charge carrier density correlations is given by q_{TF}^{-1}, from which a strong growth $\propto 1/\sqrt{n}$ of the puddles size is expected near charge neutrality. The carrier density dependence of both the charge puddles' amplitude and size in a Dirac material has not been reported yet.

The sample is fabricated on a heavily doped Si substrate covered with thermal oxide. Single layer graphene is prepared by mechanical exfoliation [167]. The number of graphene layers and the absence of surface contamination are confirmed from combined optical, Raman and ex-situ AFM characterization. Using a mechanical mask [168], we deposit the metallic source and drain contacts to form a 4 μm long graphene junction (Fig. 3.7a). Organic resist is avoided, as to ensure a residue-free surface for scanning probe microscopy. Details of the device fabrication are described in the thesis of Sayanti Samaddar.

The experimental setup is our home-made combined AFM-STM, operating at a temperature of 130 mK [134], at which all measurements presented here were obtained. The sample stage allows for in situ multi-terminal transport measurements of the device. AFM is performed by electrical excitation and read-out of a mechanical quartz Length Extension Resonator (LER) [137, 138]. This allows to rapidly move the tip to the graphene junction with the help of the position code [101, 133]. Scanning tunneling micrographs reveal a clean graphene surface, following the substrate corrugation with a roughness of about 100 pm. Scanning tunneling spectroscopy (STS) is achieved by lock-in measurements of the differential tip-to-sample tunneling conductance $G_t(x, y) = dI_t/dV_b$, by adding a 12 mV ac modulation at frequency $f = 322$ Hz to the bias voltage V_b, which is uniformly applied to the sample.

Transport measurements are performed with the tip retracted a few hundreds of nm from the sample surface. However, approaching the tip to STM contact does not produce a significant effect in the device characteristics. The conductivity of the graphene device shows a perfectly linear behavior at high carrier densities (Fig. 3.7b), in line with a density independent mobility of about 6000 $\mathrm{cm^2V^{-1}s^{-1}}$. This indicates that carrier transport is dominated by long range disorder, as can be caused by random charge impurities in the substrate [145]. A slight difference between the measured electron and hole mobilities, $\mu_e/\mu_h = 0.9{\pm}0.05$ could be related to the difference in their scattering cross-sections off charged impurities [165].

The gate voltage at which conductivity is minimized gives the overall charge neutrality point, $V_g^0 = 29$ V. This overall hole doping is consistent with the presence of negatively charged silanol groups on the surface. A residual conductivity $\sigma_0 \approx 11\, e^2/h$ is found at the charge neutrality point. Within self-consistent screening theory [155], the above values of residual conductivity and mobility point to a charged impurity distribution with a density $n_i = 7.5 \pm 0.5 \times 10^{11}$ $\mathrm{cm^{-2}}$ at a distance $0.1\,\mathrm{nm} < d < 1\,\mathrm{nm}$ below the graphene, in agreement with earlier experiments in similar conditions [145, 165, 166].

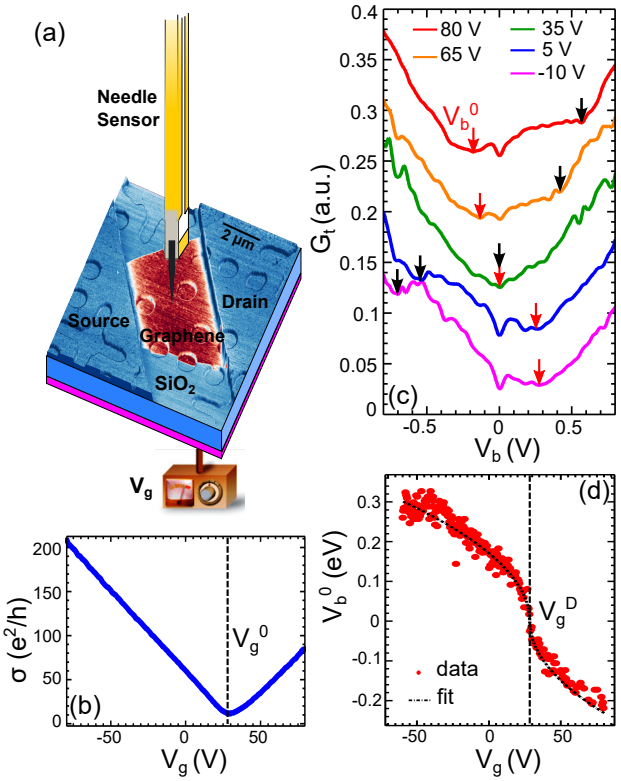

Figure 3.7: (a) Experimental configuration, combining transport measurements with scanning probe microscopy on a monolayer graphene device. A conductive tip mounted on a stiff mechanical resonator serves as the probe for combined AFM-STM. Two isolated electrical contacts (*Source* and *Drain*) enable two-probe transport measurements. The atomic force micrograph shows both the topography (vertical scale, varying between 0 and 57 nm) and the phase (varying by 3.8° from blue to brown). (b) Device conductivity as a function of backgate voltage V_g, measured at a bias voltage of 5 mV. The overall charge neutrality point is found at $V_g^0 = 29\,\mathrm{V}$. (c) Differential tip-to-sample tunneling conductance G_t as a function of the voltage V_b (uniformly applied to the sample), at several values of V_g. The red and black arrows indicate the position of the primary (V_b^0) and the secondary minimum of G_t respectively (see text). $I_t^{set} = 50\,\mathrm{pA}$ at $V_b = 0.9\,\mathrm{V}$. The curves are vertically offset for clarity. (d) Variation of the primary minimum with V_g. The black dashed line shows the fit with Eq. (3.2.1), yielding the fit parameter $V_g^D = 28\,\mathrm{V}$.

STS on gated graphene

We performed scanning tunneling spectroscopy on the graphene sheet, at distances greater than 1 μm from the metal-graphene interface as to rule out any possible influence of the leads on local properties. Fig. 3.7c shows the differential tunneling conductance $G_t(V_b)$ acquired at a given location, but at different gate voltages V_g. As in the previous section, a V-shape spectrum, characteristic of graphene, is obtained in every case. A frequently reported gate-independent depression of the tunneling conductance is seen at zero bias [134, 150, 151]. In addition, the curves display two gate-dependent local minima, highlighted by red and black arrows respectively, which move in opposite directions with V_g.

The primary minimum V_b^0 (red arrows) occurs when the Fermi level of the tip is aligned with the local Dirac point $E_D(\mathbf{r})$ of graphene, which can be written as:

$$V_b^0 = -\gamma\ \mathrm{sign}(V_g - V_g^D)\sqrt{|V_g - V_g^D|}, \tag{3.2.1}$$

where $\gamma = \hbar v_F \sqrt{\pi\kappa\epsilon_0/(e^3 t)}$ employing a plate-capacitor model, with $v_F = 1.1 \times 10^6$ m/s the graphene Fermi velocity, $t = 285$ nm and $\kappa = 3.9$ the SiO_2 thickness and dielectric constant, respectively. The local

quantity V_g^D is the gate voltage at which the Fermi levels of both the graphene and the tip are aligned with the Dirac point. It includes the influence of the local gating produced by the tip due to both the tip-sample work function mismatch and the bias voltage [168,169]. In the absence of capacitive coupling to the tip, the spatially averaged V_g^D would coincide with V_g^0 found from transport experiments. In the case of Fig. 3.7, the experimental gate dependence of the primary minimum V_b^0 can be well fitted with Eq. (3.2.1), yielding $V_g^D = 28$ V (Fig. 3.7d), the value of γ being determined by known parameters. The nearly exact matching of V_g^D at that particular position and tip condition with the global value of V_g^0 is coincidental, since V_g^D depends on the position. The secondary minimum (black arrows) occurs when the Fermi level of graphene passes through the Dirac point [150,168–170]. The above analysis provides a detailed understanding of the electron tunneling spectra dependence on the gate potential, at a given location.

Dirac point mapping

Several strategies can be used for mapping the local Dirac point. Performing a complete spectrum with open feedback loop at each position, from which E_D is then individually extracted, is the most reliable method but is very time-consuming [134, 144]. Mapping G_t with closed feedback loop set to a fixed set-point tunnel current I_t^{set} and a single V_b that is slightly offset from the average primary minimum V_b^0 by δV_b, was shown to reproduce qualitatively the $E_D(x, y)$ maps [144]. This stems from the fact that, to first approximation, a shift in E_D simply shifts the $G_t(V_b)$ curves along the V_b axis. Complications with this approach arise when one wishes to compare E_D maps at different gate voltages because V_b^0 itself is a function of V_g. Our strategy consists in first determining $V_b^0(V_g)$ at a given position (Fig. 3.7d) and then mapping G_t at a gate dependent bias voltage $V_b(V_g) = V_b^0(V_g) \pm 100$ mV. The sign of the offset is set such that $|V_b| > |V_b^0|$.

We further normalize the differential tunnel conductance maps to the set-point tunnel conductance, writing $\tilde{G}_t = (V_b/I_t^{set})\, G_t$. This normalization is known to provide a more faithful conversion of the differential tunnel conductance to the density of states when the set-point tunnel conductance is not fixed from map to map [171]. We have verified the structures observed in $\tilde{G}_t$ maps to be consistent with the E_D maps found from full current imaging tunneling spectroscopy (CITS) measurements, which were acquired at selected gate voltages. These full CITS also allow for determining the proportionality factor between the $\tilde{G}_t$ and E_D maps.

Experimental maps of the variations of $\tilde{G}_t \sim E_D$ around their spatially averaged value are shown for several gate voltages in Fig. 3.8. It is readily seen that not only the lateral extent, but also the amplitude of the doping inhomogeneities, gradually increase as the Fermi level approaches the Dirac point. For proper quantification of the observed inhomogeneities, we introduce the auto-correlation function of the E_D maps. Assuming rotational symmetry (which is only approximately true, due to the finite size of the maps), the latter is a function of only $r = |\mathbf{r}|$. The charge puddles' size ξ is determined from fitting the angular average of the auto-correlation function of each E_D map to a gaussian decay. The gate dependence of ξ displayed on Fig. 3.9a shows a strong increase near charge neutrality, which is found at a gate voltage $\bar{V}_g^D$ of about 38 V. This value is a spatially averaged property of the map area. Because of the capacitive influence of the tip [1], $\bar{V}_g^D$ is somewhat larger than the charge neutrality condition $V_g^0 = 29$ V found from transport experiments [168,169].

We further determine the standard deviation of the Dirac point variations δE_D over a map. This quantity, which reflects the amplitude of the doping inhomogeneities across the sample, is plotted on Fig. 3.9b as a function of V_g and also shows a marked peak at $\bar{V}_g^D \approx 38$ V. The error bars on ξ and δE_D are mainly associated to the finite size of the maps. Some asymmetry of the puddles' behavior is observed, which appear somewhat larger and more prominent at large electron doping, than on the hole doped side. As electron doping involves a quite large gate potential of about 60 V, a possible scenario for this asymmetry

[1] The capacitive lever arm of the tip with respect to the back gate can be estimated to $\beta \approx 50$, meaning that a tip-sample work function difference by 0.2 eV will induce a shift in V_g^D by 10 V.

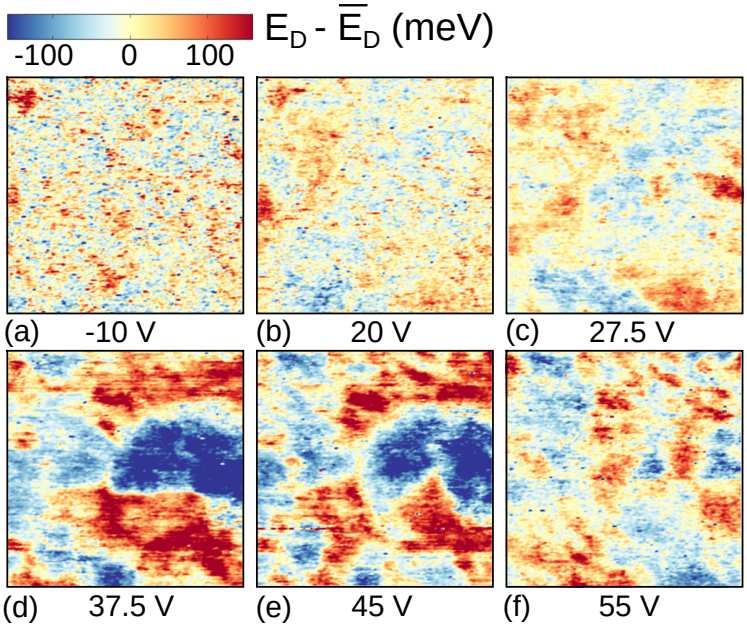

Figure 3.8: Spatial maps of the variations of the local Dirac point energy E_D around its spatially averaged value $\bar{E}_D$, over an area of $100 \times 100\,\mathrm{nm}^2$ at different gate voltages (indicated below each figure). The imaging parameters for the original G_t maps (see text) are $I_t^{set} = 50\,\mathrm{pA}$ and bias voltages V_b equal to (a) 0.298 V, (b) 0.191 V (c) 0.122 V, (d) −0.145 V, (e) −0.232 V and (f) −0.267 V.

is that the back-gate eventually influences the substrate impurities distribution itself [166].

Comparison with self-consistent screening theory

Our main experimental findings are thus that both the amplitude and the spatial extent of the puddles significantly increase as the Fermi level approaches the Dirac point. For a quantitative understanding, we now compare these results to calculations, which we have led in collaboration with the team of Shaffique Adam at the National University of Singapore. From Thomas-Fermi theory in 2D, assuming a flat Fermi sea, follows that variations in the local value of E_D/e are equal to variations in the screened electrostatic potential $\tilde{V}$ [172]. For a random 2D distribution of charged impurities with density n_i at a distance d from the graphene sheet, the auto-correlation function of the screened potential can be written [173]

$$C(r) = 2\pi n_i \left(\frac{e^2}{4\pi\epsilon_0\kappa}\right)^2 \int_0^{+\infty} q\,dq \left[\frac{1}{\epsilon(q)}\frac{e^{-qd}}{q}\right]^2 J_0(qr), \tag{3.2.2}$$

where J_0 is the zeroth-order Bessel function and $\epsilon(q)$ is the graphene dielectric function. The latter describes the screening of Dirac fermions which, within Random Phase Approximation (RPA), can be written as [145]

$$\epsilon(q) = \begin{cases} 1 + 4k_F r_s/q & \text{for } q < 2k_F, \\ 1 + \pi r_s/2 & \text{for } q > 2k_F, \end{cases} \tag{3.2.3}$$

where $r_s = e^2/(4\pi\epsilon_0\kappa\hbar v_F) \approx 0.8$ on SiO_2 is the effective fine structure constant of graphene. The dependence of the correlation function on the mean doping level (and thus on the gate potential) enters here through the dependence of $\epsilon(q)$ on $2k_F$.

We calculated the auto-correlation function for the screened potential and extracted the correlation length ξ and fluctuation amplitude $\delta\tilde{V} = \delta E_D/e$. The result for $d = 1$ nm, shown as dashed curves in Fig. 3.9a,b, accounts for the overall decrease of both ξ and δE_D, that is, stronger screening with increasing charge carrier density. The calculations have no other adjustable parameter than $\bar{V}_g^D = 38V$, the impurity

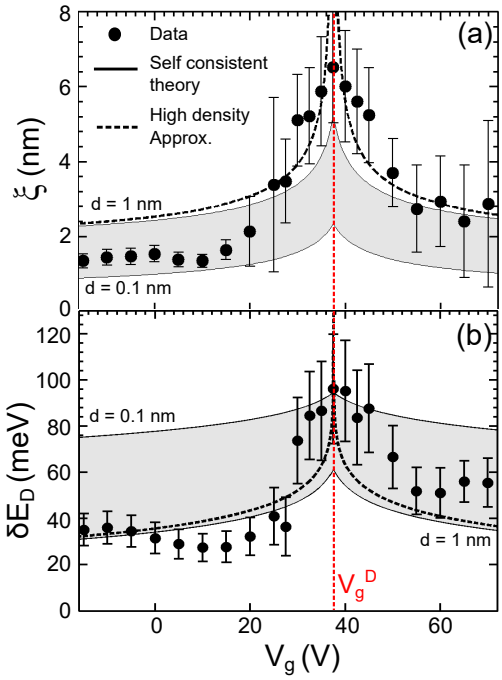

Figure 3.9: (a) Puddle size and (b) amplitude of doping inhomogeneities, as a function of the back-gate potential. The dashed lines are calculations without self-consistent correction to carrier density, with $d = 1\,\mathrm{nm}$. The gray areas represent the range of values expected from a random impurity distribution at a distance d ranging from 0.1 to 1 nm from the graphene sheet. They are delimited by solid lines corresponding to calculations using the extremal values of d, respectively. For all calculations, the value derived from transport data is used: $n_i = 7.5 \times 10^{11}\,\mathrm{cm}^{-2}$.

density in the substrate n_i being determined from the transport measurements. The puddles size follows in particular the expected trend $\xi \sim q_{TF}^{-1} \propto 1/\sqrt{n}$ at high carrier densities, where $n \propto |V_g - \bar{V}_g^D|$ is the gate induced charge carrier density. This agreement validates the microscopic picture of random potential fluctuations, for the description of which we call for Thomas-Fermi screening in a Dirac material.

At charge neutrality, for a homogeneous system, there are no excess charges available to screen the impurity potential. Accordingly, Eq. (3.2.3) predicts that both the amplitude and the correlation length diverge. However, this ignores the fact that the induced charges within the puddles can themselves screen the impurity potential. Accounting for this process self-consistently [145] leads to rewriting the RPA dielectric function of Eq. (3.2.3) with a corrected charge carrier density. The usual expression of $k_F = \sqrt{\pi n}$ is then replaced by $\sqrt{\pi(n + n^*)}$ [173], where n^* represents the disorder-induced residual charge carrier density in the graphene sheet which cannot be compensated by a global gate. The self-consistent calculations are plotted in Fig. 3.9a,b. The gray regions are delimited by the theoretical curves for $d = 0.1$ nm and 1 nm respectively. The ensuing saturation of both the puddles' size and amplitude at the charge neutrality point is in very good agreement with the experimentally observed trend.

To conclude, Sayanti Samaddar's work provides the first microscopic observation of the growth of charge inhomogeneities in graphene near the Dirac point. It further shows that the observed behavior can be very well described with a theory based on a microscopic description of the impurity potential, using parameters found from transport measurements, performed *in situ* on the very same graphene sample. This observation gives utmost credit to the charged impurity potential scenario as a limiting factor to the exploitability of Dirac physics in graphene on SiO_2.

Figure 3.10: Sketch of the band structure and its filling in a three-dimensional semiconductor (left) and in graphene (right), as a function of wave vector and of distance normal to the vacuum interface. The surface states of the 3D semiconductor are not represented. E_v, E_c and E_{vac} are the local values of the top of the valence band, the bottom of the conduction band, and the vacuum energy, respectively. The superscripts n and p indicate the situation of electron and hole doping, respectively.

3.2.3 Equivalence of electronic doping and work function in graphene at the nanoscale

After determining the response of a single graphene sheet to a disordered potential by measuring the local density of states, it was tempting to extend the experiments to a force-measurement related approach. This is readily available in situ in the combined AF-STM setup. In this section, a study of the conjunct variations of the doping level and the work function in graphene is presented and discussed. Indeed, if surface effects are neglected, any change of the Fermi level in a semiconductor is expected to result in an equal and opposite change of the work function. This is however not observed in general in three-dimensional semiconductors, because of Fermi level pinning at the surface. By combining Kelvin Probe Force Microscopy and Scanning Tunneling Spectroscopy on single layer graphene, we have measured in the frame of Sayanti Samaddar's PhD work both the local work function and the charge carrier density. The one-to-one equivalence of changes in the Fermi level and the work function is demonstrated to accurately hold in single layer graphene down to the nanometer scale [136].

In the basic picture of semiconductors and semiconductor interfaces, the Fermi level position and the work function are utterly linked [174–178]. The work function W is defined as the difference of local vacuum energy level E_{vac} and the Fermi level E_{F}. If E_{vac} is fixed, one thus has simply $\partial W/\partial E_{\mathrm{F}} = -1$. This fundamental relation however fails to hold at the surface of most three-dimensional semiconductors owing to the pinning of the Fermi level by surface states. As sketched in Fig. 3.10, a generally large density of surface states lying within the semiconductor band gap pins the Fermi level with respect to the band structure. Any change in E_F is thereby accompanied by an almost equal shift in the band structure and thus E_{vac} at the surface, leading to $|\partial W/\partial E_{\mathrm{F}}| \ll 1$ in practice [176].

The graphene surface has no dangling bonds that provide surface states to pin the Fermi level. By electrostatically tuning the doping level in a graphene device, the work function was observed to follow with good agreement the expected $\partial W/\partial E_{\mathrm{F}} = -1$ gate dependence, with $E_D - E_F$ assessed from transport measurements through the device [179, 180]. The above conclusions were thus drawn from values of both W and $E_D - E_F$ obtained from spatial averaging over the entire device, without demonstrating the work function to doping level correspondence on the local scale. However, as discussed in the preceding sections, the doping level in graphene itself can be strongly inhomogeneous down to the nanometer length scale, calling thus for a truly local comparison of the Dirac point level (that is, doping) and work function.

Using both scanning tunneling microscopy (STM) and Kelvin probe force microscopy (KPFM) we experimentally compare the local electronic charge carrier density (that is, the Fermi level position) and the work function in single layer graphene. Hereto, we study the conjunct variations of the above quantities as a function of (i) electrostatic gating and (ii) position across local delaminations of the graphene from its substrate. We have studied two different kinds of graphene samples. The first set of data presented here was obtained on graphene prepared by mechanical exfoliation on SiO_2/Si [167]. We further investigate graphene grown on an Ir(111) substrate and decoupled by intercalation of a disordered molecular layer [134, 143]. We demonstrate in both cases that variations of the local charge neutrality point, $E_D - E_F$, are in one-to-one correspondence with variations of the work function.

The monolayer graphene sample and the STS measurements are the same as described in the previous section. KPFM is performed at slightly larger tip-sample distances than STS, such that tunneling can be neglected and van der Waals forces are small. In frequency-modulated non-contact atomic force microscopy

and related techniques such as KPFM, measuring the resonator frequency shift Δf provides access to the mechanical tip-sample force gradients [181]. At zero bias voltage, that is, when the Fermi levels of probe and sample are aligned, an electric field exists between probe and sample, due to their distinct work functions and, in some cases, to local charges or dipoles. The local contact potential difference (V_{LCPD}) is the potential of the sample with respect to the tip that allows for cancelling these electrostatic forces. In the absence of isolated charges or dipoles, this potential equals the difference in the sample and tip work functions [182], $V_{\mathrm{LCPD}} = (W_{\mathrm{sample}} - W_{\mathrm{tip}})/e$.

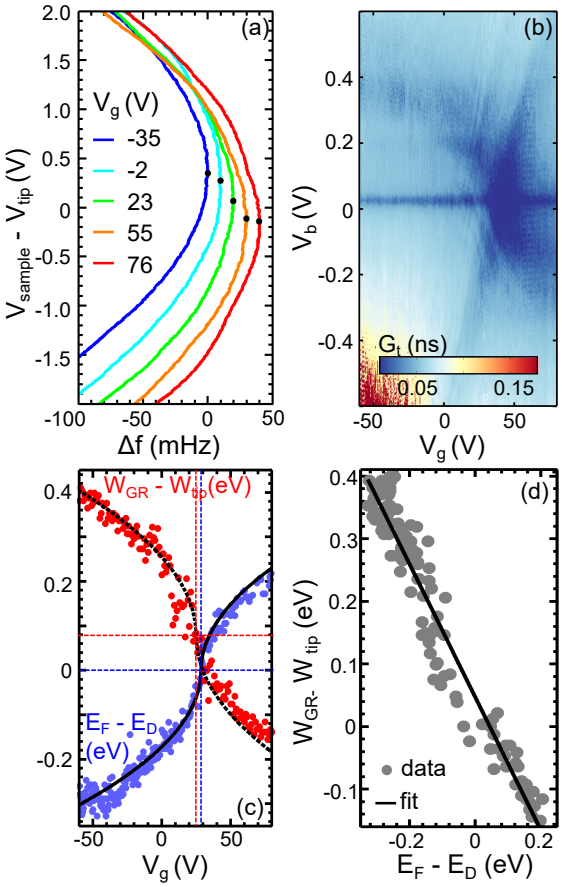

Figure 3.11: (a) Variation of the AFM probe frequency shift (each curve is offset by 10 mHz for clarity) with sample-to-tip voltage, at different back-gate voltages V_g. The black dots indicate the position of the curves' maxima at V_{LCPD}, as determined from a parabolic fit. (b) Change of V_{LCPD} with V_g. The line shows the best fit (see text) with fit parameters $V_g^D = 25\,\mathrm{V}$ and $W_0 = 80\,\mathrm{meV}$. (c) Color map showing the dependence of the differential tunneling conductance G_t on bias and back gate voltage. (d) Back-gate voltage dependence of the primary minimum V_b^0 (see text) of the tunnel spectroscopies as shown in (c). The line shows the fit with Eq. (3.2.1), yielding $V_g^D = 28\,\mathrm{V}$.

Using KPFM *in situ* on the same sample and graphene area, we have recorded the parabolic dependence of Δf on V_b for different gate voltages, the maximum of each parabola corresponding to $V_b = V_{\mathrm{LCPD}}$, whose dependence on V_g is shown in Figs. 3.11a,b. It is nicely fitted by the right-hand term of Eq. (3.2.1) offset by the sample-tip work function difference at the graphene charge neutrality point, W_0. The small value of $|W_0| < 0.1$ eV is in good agreement with the fact that both the tungsten tip and charge neutral graphene have a work function close to 4.5 eV [183].

Tunnel spectroscopies acquired *in situ* in the immediate vicinity (Figs. 3.11c,d) show an identical gate dependence of eV_b^0, that is, $E_D - E_F$, which is also very well fitted by Eq. (3.2.1). Notably, the gate coupling α is the same for both experiments and is entirely determined from known parameters. The

close agreement of both sets of data thus confirms the precise equivalence of changes of the Fermi level position and the work function in graphene. As compared to previous work [179], this is to our knowledge the first comparison of both the work function and the Fermi level determined on the *local* scale. In our experiment, the only difference between both approaches appears in the value of V_g^D. This can be well understood by considering the fact that the tip-sample capacitance being an order of magnitude larger in STM contact, the tip acts as a strong local gate which locally distorts the doping profile [169]. Apart from the tip-sample capacitance, the extent of this distortion directly depends on the effective potential drop between the sample and tip which is equal to $V_b - V_{\mathrm{LCPD}}$. This would ultimately cause a slight shift in the point of occurrence of charge neutrality, which depends on the tip-sample distance and the work function mismatch between charge neutral graphene and the tip [135].

Eventually, we have also measured the relative variations of work function and $E_D - E_F$ in a different configuration, namely, graphene decoupled from the iridium substrate it was grown on, as discussed in section 3.2.1. This work was performed in collaboration with B. Grévin from INAC/CEA, who performed part of the KPFM measurements in his dedicated setup, and who I am indebted to for teaching us the basics of KPFM. In graphene on iridium, one cannot adjust the average charge carrier density by electric field effect from a back gate. However, one can correlate spatial variations of the Dirac point level and the work function along the sample surface by moving to topographic delaminations of the graphene, the so-called wrinkles [184]. Here again, and as discussed in more detail in [136], the combination of STM and KPFM demonstrates on the local scale the validity of the relation $\partial W/\partial E_{\mathrm{F}} = -1$ between work function and doping.

In conclusion, by combining two scanning probe microscopies and two graphene substrate types, we have demonstrated the one-to-one correspondence of the Fermi level and the work function in graphene to hold accurately and on the local scale.

Chapter 4

Perspective

This chapter presents my ongoing research works, preliminary results or projects. It is structured along the three main axes of the three preceding chapters and proposes their deepening, namely along the following directions: (i) the dynamical behavior of SQS junctions, (ii) thermal and thermoelectric effects in QD junctions, and (iii) a scanning probe microscopy approach to study of the competition of superconductivity and other many-body effects.

4.1 Quantum dynamics in SQS hybrids

4.1.1 Landau-Zener-Stückelberg physics at the edge of a semi-continuum

This section is devoted to an interpretation by Denis Basko of some experimental data we obtained during the thesis of David van Zanten. Because the experimental data would deserve to be reproduced and explored in more depth, they are not yet published. In the meanwhile, Denis Basko has published the theoretical frame independently from our data [27]. Below, I will present some preliminary data corroborating Denis Basko's scenario of Landau-Zener-Stückelberg physics, which can occur when the quantum dot level is driven sufficiently slowly across the superconducting single-particle gap edge.

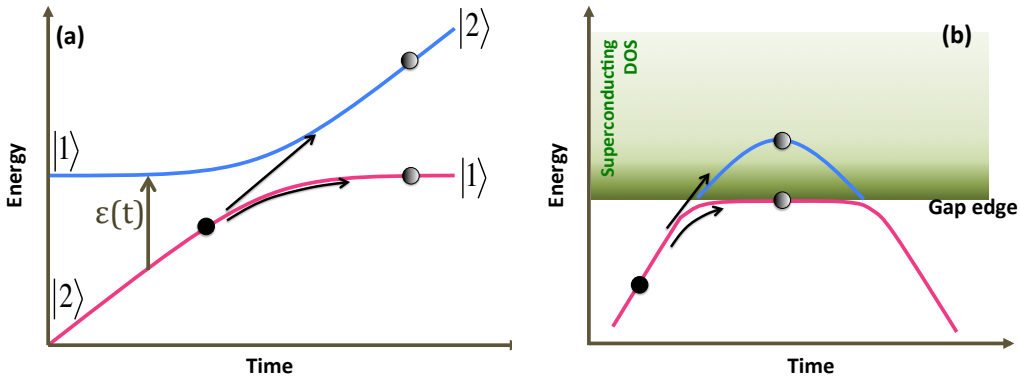

Figure 4.1: (a) Standard picture of the Landau-Zener transition occurring at the avoided crossing of two perturbatively coupled states. The amplitude of the wave function in both final states depends critically on $\dot{\epsilon}$ at the avoided crossing. (b) Analogue of the Landau-Zener transition, as a quantum level crosses the edge of a semi-continuum it is coupled to. In the adiabatic limit, the particle stays in the ground state. For fast drives, the wave function amplitude is insensitive to the subgap state and the particle behaves semi-classically.

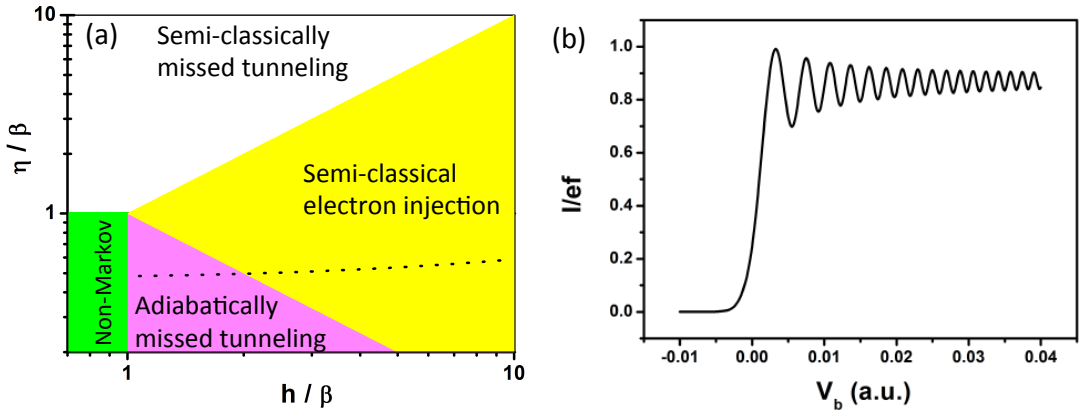

Figure 4.2: **(a)**: Different turnstile operation regimes in the parameter space describing a parabolic excursion of the quantum dot level about the superconducting gap edge. The two control parameters are the reduced height h/β of the parabola above the gap edge, and the parameter $\eta \propto (\text{parabola curvature})^{1/3}$. The colored regions correspond to the different regimes identified in the text, that is, the semi-classical turnstile operation regime (yellow), classically missed tunneling (white), adiabatically missed tunneling (pink), and the non-Markovian regime (green). A frequency sweep at fixed amplitude corresponds to a vertical line in this map. The dashed line represents a typical amplitude sweep, assuming $f = 10^{-2}\gamma = 10^{-4}\Delta$. Figure adapted from D. Basko [27]. **(a)**: Calculation of the SQS current near the threshold for turnstile operation, as a function of bias voltage. The oscillations of the current are characteristic of the Stückelberg oscillations, due to the interference of the wave functions having travelled along the two different trajectories in Fig. 4.1. Only at much higher bias/amplitude will the current tend towards ef (courtesy D. Basko).

Landau-Zener transition

Assume two quantum levels $(1, 2)$ of an unperturbed Hamiltonian, separated by an energy $\epsilon = E_2 - E_1$, which can be externally controlled (by a gate, magnetic field, ...), and which are further coupled through a time-independent perturbation W. The latter has no significant qualitative influence on the system, unless $|\epsilon|$ is tuned to be smaller than the off-diagonal terms $|W_{1,2}|$ (which is nothing but the tunnel coupling Γ in our case) in the basis of the original levels. In the latter case, the eigenvalues of the full Hamiltonian display an anti-crossing at $\epsilon = 0$, often referred to as *level repulsion*. Now, when a particle is initially in one of the unperturbed quantum levels (for example, the one of lower energy) and $\epsilon(t)$ is swept dynamically through degeneracy at $t = t_0$, the probability of finding eventually the particle in one or the other eigenstate varies rapidly between 0 and 1 depending on the value of $\hbar\,\dot{\epsilon}(t_0)/|W_{1,2}|^2$ compared to 1 [185–188] (Fig. 4.1). Such Landau-Zener transitions, in which a particle in promoted to the excited state by *diabatically* driving the system through level degeneracy, are benchmark experiments in atomic physics [189] and quantum magnetism [190]. In the opposite limit of small $\dot{\epsilon}$, the adiabatic theorem ensures that the particle stays in the ground state.

Crossing of a single level with a semi-continuum

The generalization of the Landau-Zener transition to a single level entering a semi-continuum, which it is weakly coupled to, was first described by Demkov and Osherov [191]. It was recently refined for the special case of a semi-continuum with a singular edge, such as provided by the superconducting single particle gap edge [27]. Here, the static spectral functions of the perturbed system change qualitatively as the single level crosses the gap edge, as already discussed in section 1.3.2. From this description, it becomes clear that the semi-classical "elevator-like" picture used in the discussion of the SQS turnstile (section 1.4) corresponds to the limit of a strongly diabatically driven quantum level.

In [27] an excursion of the single quantum level into the semi-continuum is considered, parametrized by a parabola $\epsilon(t) = h - \eta^3 t^2$, the origin of energies being taken at the gap edge. Semi-classically, tunneling is possible over the time window $\Delta t = 2\sqrt{h/\eta^3}$ around $t = 0$. Several regimes can be identified, depending on the hierarchy of three relevant energy scales: h, η and $\beta = (\gamma^2\Delta)^{\frac{1}{3}}$ (a quantity we already encountered in section 1.3.2, within a numerical prefactor). Depending on these, different regimes are identified in Fig. 4.2a and can be summarized as follows:

- $\eta/h \gg 1$. The parabolic level excursion into the semi-continuum is too brief for tunneling to occur (white region). The same is true for $h < 0$, that is, meaning that the level is not even entering semi-classically the semi-continuum.
- $\eta/h \ll 1$ and $\eta h \gg \beta^2$ (pink region). In this limit, which represents the main novelty of the prediction by D. Basko, the behavior is adiabatic, meaning that the particle does not tunnel to the semi-continuum, although this would be expected semi-classically.
- If $\eta h \ll \beta^2$ (yellow region). Adiabaticity is broken and the usual semi-classical picture for tunneling, using the Fermi golden rule expression, is recovered.
- Finally, when η and h are both $\sim \beta$ or less (green region), the calculations are difficult because the Markovian approximation breaks down but the ejection probability will be neither very close to 0 neither to 1.

When a SQS turnstile is driven with a sinusoidal gate voltage, decreasing the frequency can be viewed as going down on a vertical line in Fig. 4.2a. For very large frequencies, missed tunneling leads to significant deviations from $I = e\,f$ in the white region. At intermediate frequencies (yellow region), semi-classically as well as adiabatically missed tunneling events are both strongly suppressed and turnstile operation is optimal. Finally, at very low frequencies (pink region) the particle remains adiabatically in the sub-gap state and the tunneling is exponentially suppressed, with a probability

$$P_\infty \approx \exp\left(-\frac{\pi}{4}\left(\frac{\beta}{\sqrt{\eta h}}\right)^3\right).$$

When decreasing the gate drive amplitude at a fixed bias and frequency, the parabola parameters follow $\eta = ((\Delta + h)\,\omega^2/2)^{\frac{1}{3}}$, shown as a quasi-horizontal line in Fig. 4.2a. If $\eta(h)$ enters the pink region, adiabatically missed tunneling sets on. In this case, and in stark contrast with the semi-classical situation, the tunneling probability displays a beating pattern at the edge of the adiabatic regime (Fig. 4.2b). This is due to quantum interference of the two wave functions that recombine after $\Delta t = \sqrt{h/\eta^3}$, having taken different paths in energy space. This effect is analogous to the Landau-Zener-Stückelberg interference effect [189, 190].

SQS turnstile experiments with a sine gate drive

The turnstile experiment described in section 1.4 (and [68]) was using a square ac gate drive of the QD level, corresponding to a large $|\dot{\epsilon}|$, meaning that adiabatic effects can be neglected. Within the semi-classical picture, we observed the static thresholds for tunneling, linking the bias voltage and the gate drive amplitude linearly, and leading thereby to the cross-like pattern seen in Fig. 1.10, which separates the regions of current equal to 0 and $\pm ef$, respectively. In Fig. 4.3 are shown the same data for a **sine** gate drive. At high frequencies, a similar cross-like pattern is observed. However, as the frequency is lowered, between the two turnstile current regions a gap opens, at which the current is suppressed. As the frequency is lowered, this gap widens. Note that we have taken great care to ensure that this gap was not due to an improper centering of the dc part of $\epsilon(t)$.

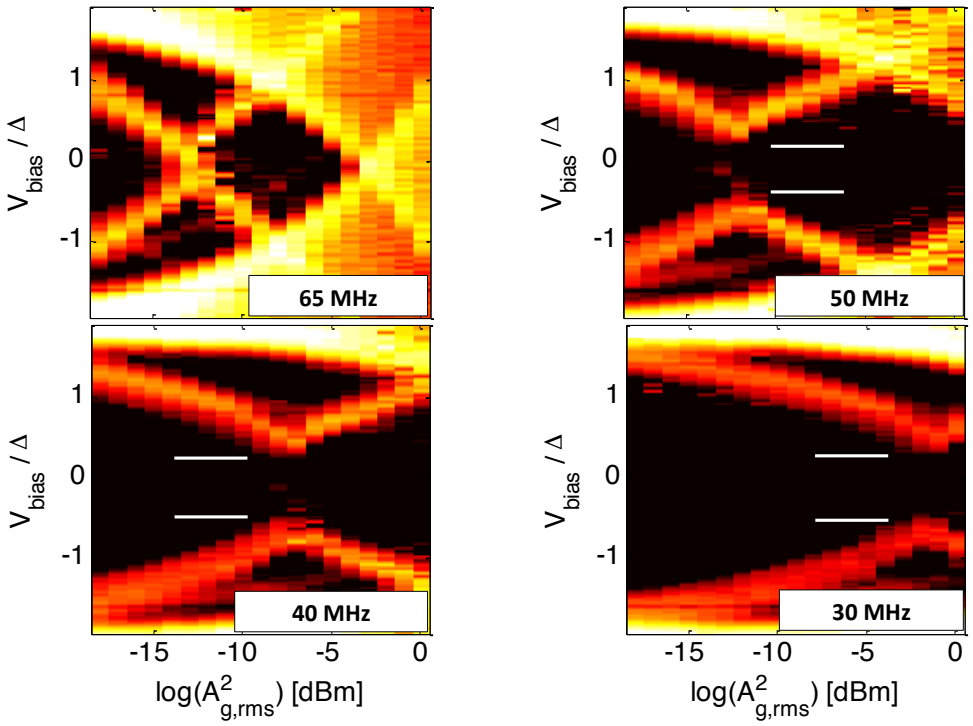

Figure 4.3: Maps of the differential conductance of the SQS turnstile as a function of bias voltage and sinusoidal ac gate drive amplitudes, at different frequencies. The results are to be compared with the map shown in Fig.1.10, in which a square gate drive was applied. As the frequency is lowered, the turnstile plateaus at $\pm e\,f$ start to be separated by a gap in V_b. Note that the x-axis involves the logarithm of the drive amplitude, which leads to a distortion with respect to the cross-like pattern from Fig. 1.10.

While it is too early to claim the experimental observation of Landau-Zener(-Stückelberg) physics occurring at the edge of the singular superconducting semi-continuum, this perspective has clearly been one the main objectives in the studies of SQS junctions lately. During the initial experiments led by David van Zanten, we did not understand this opening of a gap and did thus not fully characterize the effect. In particular, we are lacking experimental evidence of the Stückelberg beating pattern just above the turnstile threshold. Nevertheless, the magnitude of the observed gap agrees qualitatively with theoretical estimations.

Possible limitations of the adiabatic scenario

We have identified two effects that could spoil the prediction of adiabatically missed tunneling at slow sinusoidal gate drives.

Decoherence. Any supplementary perturbation might induce transitions from the fragile sub-gap state to the continuum. These can be seen semi-classically as high-frequency noise on top of the sinusoidal gate drive, breaking thus adiabaticity, or quantum mechanically speaking, as photons connecting the sub-gap state to the states above the gap edge. Careful engineering of the electromagnetic environment might thus be key for enhancing the signatures of adiabatically missed tunneling. If such decoherence does not completely destroy the effect, it might nevertheless lower the threshold for breaking the adiabatic protection. From first estimates, it seems indeed that the experimentally observed suppression of tunneling near the threshold be slightly less than the prediction (Fig. 4.4), and completely collapse above ~ 70 MHz.

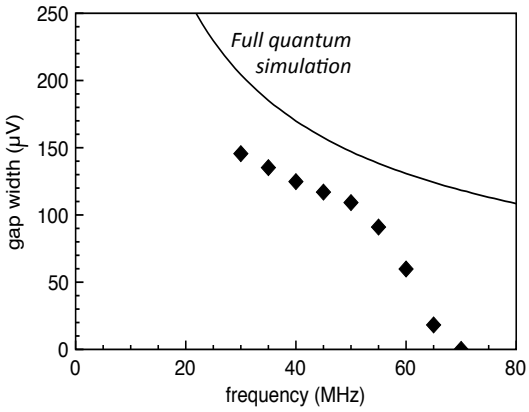

Figure 4.4: Amplitude of the gap observed in Fig. 4.3 as a function of frequency. The line shows a calculation of the same by D. Basko, assuming a BCS-type density of states without Dynes broadening and no decoherence mechanism of the subgap state.

Smearing of the superconducting edge. The superconducting gap edge of aluminum is extremely sharp [74]. However, finite Cooper pair life-times (due to intrinsic or extrinsic processes [192, 193]), will induce a smearing, which is well captured by the Dynes parameter, already discussed in section 1.3.2. When the distance of the sub-gap state energy to the gap edge is less than the Dynes broadening, which we find using Eq. (1.3.3) to occur for $h > \gamma\sqrt{\Delta/\vartheta}$, the adiabatic picture breaks down. For a very conservative estimate of the Dynes parameter $\vartheta = 10^{-4}\Delta$ and assuming $\gamma = 0.01\Delta$, one finds adiabaticity to be unaffected up to $h \approx \Delta$, that is, amplitudes at which semi-classical backtunneling must already also be considered. Therefore, although great care must be taken to shield the SQS junction electromagnetic environment, Dynes broadening should not significantly alter the sub-gap state protection *with pure aluminum as the superconducting material*. We stress that the very particular properties of our superconducting junctions, in terms of point-like contact and absence of an interface material to the QD, as discussed in section 1.1, can probably explain why this effect has never been observed before, for example in CNT-based superconducting junctions.

4.1.2 Spin selection and manipulation in the SQS turnstile

In materials with small spin-orbit coupling (such as in aluminum), an applied magnetic field B will shift the densities of states of both spin eigenstates along the quantization axis by their respective Zeeman energies $E_Z = \pm\frac{1}{2}g\mu_B B$. Here, g is the material-dependent gyromagnetic ratio, which is close to 2 for free electrons, and also in aluminum [194]. The ensuing spin-dependent tunneling probabilities lead to a doubling of the coherence peak structures in tunnel spectroscopies, where one lead is superconducting aluminum. This effect is the basis of Meservey-Tederoff spectroscopy [194], and can be used for measuring the spin polarization of the other (normal or magnetic) lead. Importantly, the magnetic field should not destroy or excessively smear the superconducting spectroscopic features, which can be achieved by using a parallel magnetic field and Si-doping induced disorder in the aluminum leads.

Similarly, a QD level's spin degeneracy is also lifted by a magnetic field (see discussion in section 1.1), where g will again vary between ~ 2 and quite large numbers in large spin-orbit coupling materials, such as semiconducting QDs [195]. It is now an intriguing question how the Zeeman spin-splitting of the relevant densities of states, both in the leads and in the QD, would affect the SQS turnstile operation, and if spin-selective turnstile operation can be achieved. In the case where $g_{\mathrm{lead}} \approx g_{\mathrm{QD}} \approx 2$, the densities of states of each spin species are shifted by the same amount throughout the device, and no spin dependence of the tunneling probabilities can be induced. Conversely, a small difference between g_{lead} and g_{QD} could suffice to allow one spin species to tunnel between the QD and one lead, but not the other. The criterion is that

$|(g_{\mathrm{lead}} - g_{\mathrm{QD}})\mu_B B|$ be less than the spectroscopic smearing, in particular of the superconducting gap edge, which gets strongly altered above about 1 Tesla, in the best case.

Finally, the case where the QD has a g factor differing significantly from 2 also corresponds to large spin-orbit coupling. While large Zeeman splittings can now be easily achieved, the levels are no longer spin eigenstates. Nevertheless, the quantum expectation of S_z in either level can still be different from 0. Therefore, any difference in the leads' and QD's respective g factors could in principle lead to spin-polarized turnstile operation. Besides possible applications as a spin-polarized single-electron source, the understanding of spin-dependent tunneling processes in SQS-type junctions and turnstiles, with or without spin-orbit coupling, would be a highly intriguing challenge.

4.1.3 Calorimetric detection of a single tunneling electron

Quantum thermodynamics and the control of entropy flow in the quantum regime has been recently the subject of intense theoretical and experimental investigations [197], with the Landauer erasure principle

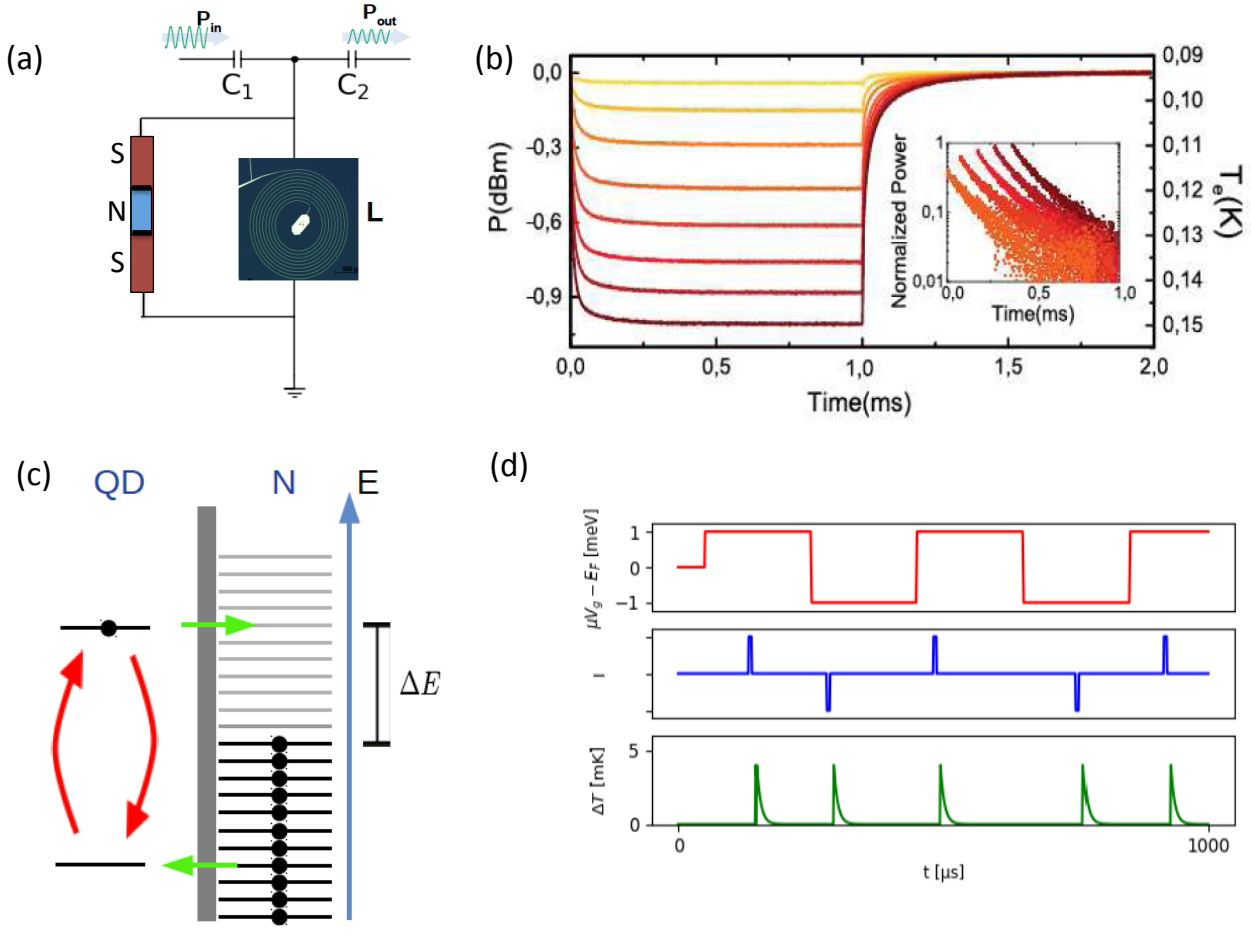

Figure 4.5: (a) Proposed RF readout of the SINIS electron thermometer using a superconducting LC resonator, as already used in Aalto. (b) Time-resolved transmission at resonance, reflecting the relaxation of the temperature in N after the heater is switched off at $t = 1$ ms [196]. (c) Gate-controlled charge and energy exchanges between N and a QD. If the gate is driven with a square signal, the QD injects one electron and one hole (both providing the same amount of heating) per gate cycle. (d) Schematic time dependence of the gate drive, instantaneous charge current and temperature in N, respectively, in the course of the cycles described in (c). Drawings by Efe Gümüs.

[198] and the understanding of Maxwell demons [199] at heart. For the study of thermodynamics, reliable and fast thermometry is key. The NIS tunnel junctions discussed in section 2.2 are excellent electron thermometers in the sub-Kelvin regime. Because of the high impedance of such junctions, they are however very slow, due to large RC time constants, on the order of a fraction of a second. In this context, the group of J. Pekola at Aalto University (Finland) has recently developed a dispersive read-out technique of NIS junctions, by embedding these inside a radio-frequency on-chip resonator [196,200]. The resonator response at resonance then strongly depends on the tunnel junction impedance, which itself depends on the local temperature (Figure 4.5). The above fast thermometry technique already demonstrated mK sensitivity at MHz read-out bandwidth in its first version, and could still be significantly improved.

The goal of this project, which will be conducted by Efe Gümüs, is a proof-of-principle experiment for detecting extremely small instantaneous energy releases in a quantum circuit. The first milestone will be to couple this novel dispersive thermometry technique to a single-electron injector, based on the same or a similar principle as the turnstile devices from section 1.4. For a copper island of volume $30 \times 300 \times 500$ nm^3 at 50 mK, the injection of a single 0.1 meV electron raises the electronic temperature by 0.7 mK, which is within reach of the RF-NIS thermometers.

We have recently implemented three microwave lines to the sample cavity in one sionludi. Two of them are used for the resonator transmission measurements, the third for the ac gate drive. At this stage, the setup is close to a conformal copy of the one described in [196]: we are using the same cryogenic circulators (located at base temperature), low pass filters, and a similar cryogenic amplifier (LNF; 0.4 - 8 GHz; gain=+40dB, located at 4 K). Presently we are using LC resonators provided by Aalto. Data acquisition is done with a NI PXI generator/synthesiser. Fig. 4.6 shows the first measurements of the bare LC resonator.

Before coupling electromigrated QD junctions to the above circuit, we will start with a simpler device, shown on Fig. 4.6b. A small island is tunnel coupled to a larger normal region N, large enough to have a negligible charging energy (as compared to the superconducting dot) but small enough to have a heat capacity allowing for detecting small heat releases. The normal island is tunnel coupled to two superconducting leads, forming an NIS junction. The tunnel barriers to the dot and to the leads will be identical if two evaporation angles are used, but can be different using three angles. The entire junction resides on the ac backgate developed for the SQS turnstiles.

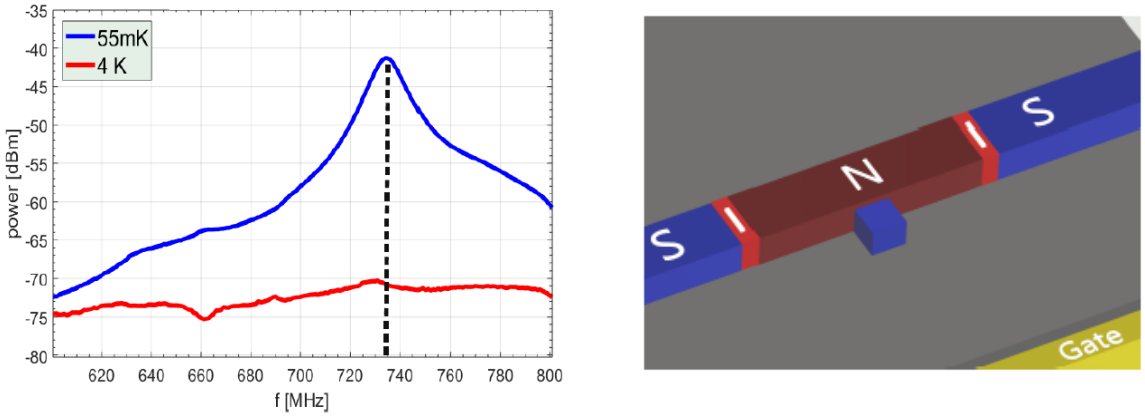

Figure 4.6: **Left**: Transmitted power $\propto S_{1,2}^2$ of the superconducting LC resonator. At base temperature, a resonance at 735 MHz is visible, with quality factor 60. In the absence of the NIS junction in parallel, this response changes very little up to $T \approx 1$ K. Around $T \approx T_c^{\text{aluminum}}$, the transmission rapidly collapses towards the red curve, measured at 4 K. **Right**: Proposed single electron injector into N, provided by a single electron box, or a quantum dot (blue cube). Data and drawings by Efe Gümüs.

Towards implementing a Maxwell demon using temperature as the feedback parameter

The tunneling device depicted in Fig. 4.5c could be used as a Maxwell demon. Suppose the that QD level is $\epsilon \sim k_B T > 0$ (the origin of energies being taken at the Fermi energy of N). The average occupation of the QD is now $< 1/2$. However, If the temperature T_N in N is finite, an electron at energy ϵ could from time to time tunnel into the QD, lowering thereby the energy in N by $k_B T$, and decreasing thus T_N. If the occupation number of the QD can be measured in real time, ϵ can then be immediately set to negative values $\sim -k_B T$, as soon as the electron has entered the QD. The electron will then be released to fill a hole at energy $-k_B T$ in N, which leads again to cooling. And the same procedure is started from the beginning. Such a Maxwell demon, which allows generating a cooling power from information (here, the occupation number of the QD), has already been implemented by the Helsinki group in a similar device geometry. In their experiment, the demon was measuring the charge state of the QD (a single electron box there). However, the RF readout of T_N could here be taken advantage of, and take the fluctuations in T_N as the demon feedback parameter: if at $\epsilon \sim k_B T$, T_N shows a negative fluctuation, ϵ is immediately driven to $\sim -k_B T$, etc.

4.2 Thermal transport through a quantum dot junction

In this section, ongoing experiments and projects on the thermoelectric response of single quantum dot junctions are described. This work is led by Bivas Dutta, who was joined by Danial Majidi recently, and the results are very recent and yet under analysis. The principle of these experiments is similar to those described in section 2.2, the principle difference being that the single-electron box connecting the source and drain has now discrete energy levels. Depending on the tunnel couplings, the physics at play can however display completely novel features, including Kondo-correlations.

4.2.1 SNS thermometry

In section 2.2, the local thermometry for determining the temperature gradient across the SET was performed using NIS junctions. In the recent QD-based thermoelectric experiments, we have moved to SNS Josephson junction-based thermometry, via the temperature dependence of the critical current, as given for example in Eq. (2.1.1). NIS thermometry is precise but it has a few drawbacks: First, forcing a current through these extremely high differential resistance junctions at voltages below Δ/e produces dissipation and has long RC response times. In the particular situation of electromigration junctions, the *source* island as shown in Fig. 4.7 must have at least one low-impedance access, which is not the case of the NIS junctions.

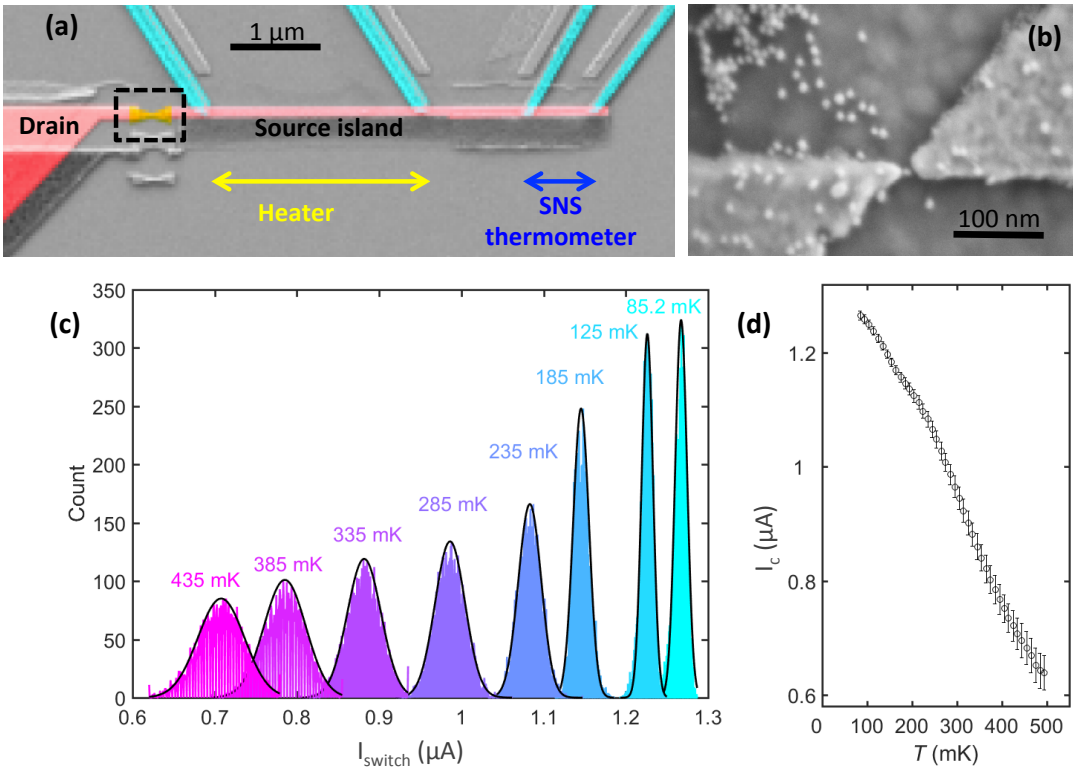

Figure 4.7: (a) Scanning electron micrograph of the QD device for thermoelectric measurements. The central *source* island is made of gold. The leads of the electromigration junction itself (orange color) are made of Pt, which suppresses proximity superconductivity from the nearby Al probes. Four transparent superconducting aluminum contacts are used for SNS thermometry (right-most pair) and heating (left pair), respectively. The left-most contact is a *drain* both for charge and heat flow. (b) Zoom on an electromigration junction such as the one in the dashed box in (a), showing one 8 nm diameter nanoparticle here. (c) Switching current histograms, from which I_c is extracted at a given temperature. (d) Temperature dependence of the critical current of the SNS thermometer.

This problem is circumvented in SNS-based thermometry, using transparent contacts of the superconducting leads to the *source* island. Beyond being compatible with electromigration, this choice further saves one shadow-evaporation angle and allows for thermovoltage measurements with lesser access impedance to the junction. Finally, the estimation of the Joule power injected into the *source* island is also much simpler and more reliable using transparent contacts to the island rather than using NIS junctions, in which a balance between Eq. (2.2.1) and heat backflow from the superconducting leads has to be considered [87].

As discussed in section 2.1.2, for good thermometric sensitivity, the Thouless energy of the SNS junction must be smaller than $k_B T$. In our case, E_T is usually 5 to 15 μeV and, after careful filtering of the electrical lines, we find an unsaturated $I_c(T)$ dependence (Fig. 4.7d). Because the experimentally measured switching current is a stochastic quantity, we determine I_c from the median value over 5000 measurements, taken with a rate of about 300 Hz. The associated temperature noise is $\sim 100\,\mu\mathrm{K}/\sqrt{\mathrm{Hz}}$ and we can detect changes in the heat load $\delta\dot{Q}$ of a few tens of aW to the island. The heater junctions are also of SNS type, but here the normal part is sufficiently long ($> 2\mu$m) and narrow to ensure ohmic behavior down to extremely small nominally injected powers. We also ensure that the closest NS interface for proximity-induced pairing correlations to be negligible at the QD contact (which was not the case in early experiments).

4.2.2 Thermopower of a weakly coupled quantum dot junction

The thermopower of a junction is defined as

$$S = -\left.\frac{V_{\mathrm{Th}}}{\Delta T}\right|_{I=0},$$

relating a small temperature difference ΔT to an associated open-circuit thermovoltage V_{Th}. In the presence of sequential tunneling processes only, the thermopower of a QD junction has a sawtooth behavior. The signal increases linearly, goes through zero at each degeneracy point, and switches sign abruptly in the middle of each Coulomb diamond [118]. In practice, cotunneling processes become rapidly the dominant mechanism away from the charge degeneracy point, leading to a truncation of the sawtooth signal [120] (see sketch in Fig. 4.9).

The measurement of the thermovoltage across a high-impedance device is rapidly confronted to difficulties in providing experimentally true open-circuit conditions. The frequently used lock-in technique at frequency 2ω, with ω the heater current modulation angular frequency, is also prone to equilibration problems. Given the nearly divergent RC times of the junction away from charge degeneracy, the assumption of instantaneous current equilibration (corresponding to the subscript $I = 0$ in the definition of S) is not necessarily verified for experimentally reasonable excitation frequencies. Therefore, in all ensuing thermovoltage measurements, we have used the following protocol: we sweep the dc voltage bias and measure the current, defining therefrom $-V_{\mathrm{Th}}$ as the bias voltage at which the current changes sign (Fig. 4.8a). Whenever tested in parallel to our method, the 2ω lock-in technique led to a qualitatively identical thermovoltage response as a function of V_g, but quantitatively much smaller amplitudes.

Measuring the full $I(V_b, V_g)$ characteristics in presence of a temperature gradient further allows extracting the thermocurrent I_{Th}, defined at $V_b = 0$. The full thermoelectric data can be fitted using a cotunneling model (collaboration with Paolo Erdman, Fabio Taddei and Saro Fazio from Pisa) [201], which allows extracting the local temperatures and thus the temperature drop ΔT, even without an independent thermometer (Fig. 4.8b). Knowing both the thermoelectric power generated and ΔT, we are presently analyzing the full efficiency of the QD junction as a heat engine, in the spirit of a recent publication on a similar system, based on a QD defined in a semiconducting wire [202]. However, both the above-cited work and our experiments shown in Fig. 4.8 are lacking an independent determination of ΔT. This significantly weakens the conclusions on the heat engine efficiency, because the determination of the heat flow across the junction is indirect. This is in contrast with the experiments of section 2.2, in which this heat flow was experimentally known. In the present case, the absence of an independent measurement of ΔT was due to

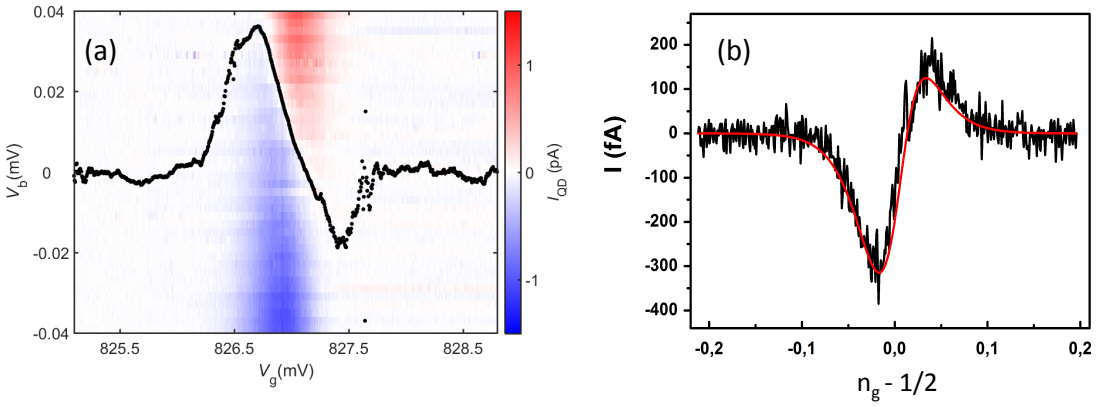

Figure 4.8: **(a)**: $I(V_b, V_g)$ map (color code range = ±1.5 pA) of a weakly coupled QD junction, near a degeneracy point and in the presence of a thermal gradient across the junction, with a power $\dot{Q} = 9$ fW applied to the source island. Along the black line, by which we define $-V_{\mathrm{Th}}(V_g)$, the current is zero. $T_b = 80$ mK. **(b)**: Experimental thermocurrent at a finite $V_b = -9\,\mu$V versus $n_g \propto V_g$ and fit (line) using the sequential+cotunneling model developed by Erdman and collaborators. The fit allows estimating the temperature on both sides of the junction, and thus ΔT, without an independent thermometer. Here, $T_{source} = 235$ mK, $T_{drain} = 143$ mK, $\Gamma_L = 9$ MHz, $\Gamma_R = 30\,\Gamma_L$ are found from the fit.

a broken contact on the SNS thermometer. The experiment will be repeated soon, including thermometry, and will allow a reliable determination of the maximum achievable efficiencies, both at zero and maximum output power, in a single quantum level-based thermoelectric device.

4.2.3 Thermopower in the presence of Kondo correlations

Thermopower is always the result of electron-hole asymmetry. When the highest occupied level of a QD junction is far down from E_F, the spectral function is asymmetric, but its effect is shunted by cotunneling. In the presence of Kondo correlations, which can appear for an odd QD occupation number and sufficiently high couplings as discussed in chapter 1, a novel spectral resonance emerges. The Kondo peak, of width $k_B T_K$, is at the Fermi level and symmetric around E_F.

In their calculation of the thermoelectric properties of a junction across a spin 1/2 impurity [203], Costi and Zlatić find a 2e-periodic thermovoltage signal, which has a clear sign change from one degeneracy point to the following one. The only experiment to date on thermovoltage in the Kondo regime was performed in a QD formed in a 2DEG [204]. However, the signatures of the Kondo effect superimpose with other effects such as conventional cotunneling in the devices studied in that work, leading to an ambiguous thermovoltage signature, that does not change sign from one degeneracy point to the following. The main conclusion from that work is essentially that the Mott formula

$$S_{\mathrm{Mott}} = \frac{\pi^2 k_B^2 T}{3\,e} \frac{\partial \ln G(E)}{\partial E},$$

relating the energy-dependent charge conductance $G(E)$ to the thermopower under the assumption of uncorrelated transport, does not hold.

Fig. 4.9 describes a QD junction displaying a spin-1/2 Kondo effect, revealed by a zero-bias resonance in charge conductance in every other Coulomb diamond. The associated energy scale is $T_K \sim 1$ K, and varies with V_g. The Kondo origin of the resonance is confirmed by measurements under magnetic field (data not shown), under which the resonance splits. The plot on the right bottom side in this figure shows the measured thermopower of the QD junction. The data are in agreement with the theoretically expected behavior, shown above, and display in particular a sign change of S at consecutive charge degeneracy points,

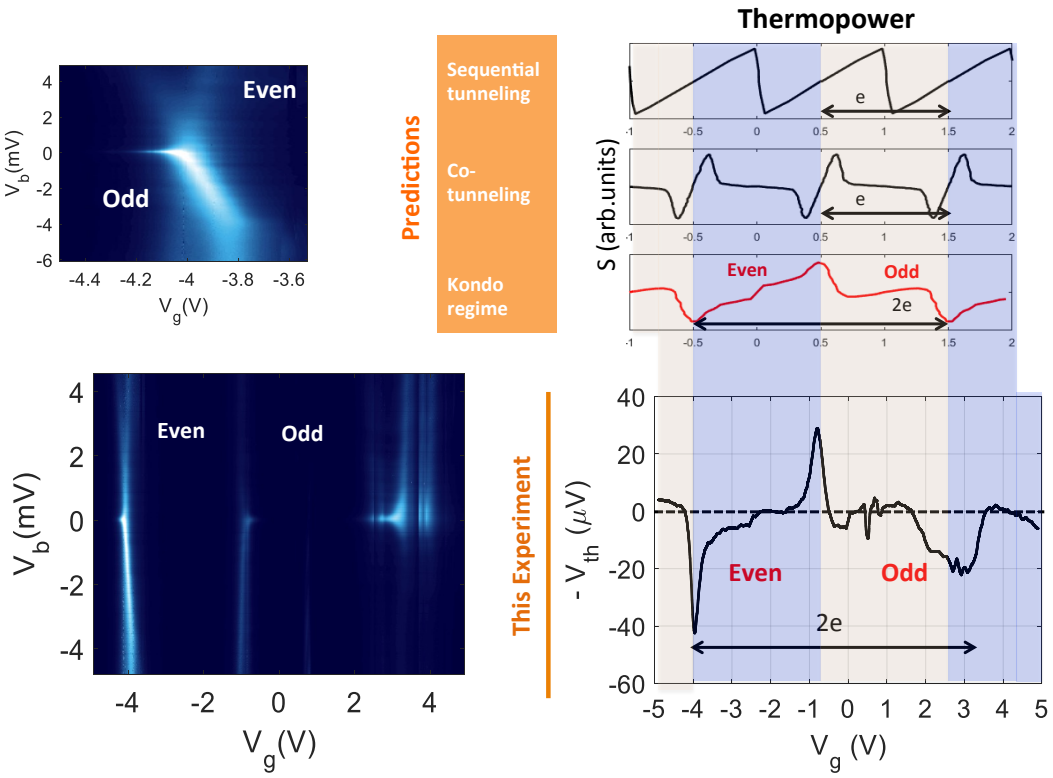

Figure 4.9: The left maps show differential conductance maps of the device ($T = 70$ mK), the top one being a zoom of the map in the lower panel. The zero-bias resonances appearing alternatingly to the left and and to the right hand of consecutive degeneracy points are the result of a spin-1/2 Kondo resonance in the oddly-occupied Coulomb diamonds. As the QD chemical potential in the oddly occupied state moves away from the leads' chemical potential, the Kondo energy scale T_K decreases, following Eq. (1.3.4), until it can no longer be resolved experimentally. The left top panel shows schematically the theoretically expected thermopower of a QD junction, assuming (i) sequential tunneling only [118], (ii) additional contributions from cotunneling [120], and (iii) Kondo correlations [203]. The presence of Kondo correlations induces a striking $2e$ periodicity of S in the gate-induced charge on the QD, in stark contrast with the other transport mechanisms. The experimental data (lower right panel) show the characteristic sign change of S between two neighboring degeneracy points, in excellent agreement with the Kondo picture.

pointing to an overall $2e$ periodicity. This preliminary result is still under investigation and analysis.

4.2.4 Heat imprint of the electron transport in a quantum dot junction

Electron transport usually produces Joule heating. In some special cases however, such as in NIS coolers, it may produce cooling of one lead [70] (section 2.2). This effect has been thoroughly investigated by Hervé Courtois before my recruitment [205, 206] and I have contributed to a few works [86, 207–211] which will not be described here. Electronic on-chip refrigeration is based on the energy selectivity of the available transport channels: when only high-energy quasi-particles may leave one lead, this lead's enthalpy might get reduced and its temperature decreases. The mechanism is analogous to Peltier cooling in semiconducting $p-n$ junctions [70].

Energy-selective transport is also naturally provided by QD junctions and QD-based refrigeration has been proposed [212] and later realized in a 2DEG [213]. We also plan to study QD-based refrigeration, as a function of a variety of parameters, such as the tunnel couplings and the ensuing quantum coherence across the junction. The pioneering experiment by Prance *et al.* [213] was eventually limited by the charging

energy and the internal thermalization of the island to be cooled by the QD. In our experimental geometry, these problems should be absent because of the metallicity and the transparent superconducting contacts to the *source* island, as depicted in Fig. 4.7a.

The samples we have studied so far have not allowed entering the regime in which refrigeration could be observed. However, in the following will be presented a QD junction which we have operated as a heat valve, similarly to the preceding single-electron heat transistor experiment that allowed studying the Wiedemann-Franz law in the presence of Coulomb interactions [87]. Further, we study here the gradual crossover from thermal transport (at zero current) towards Joule heating, which sets on as the bias voltage is cranked up. The data are presently still under analysis.

Fig. 4.10d shows preliminary results of a temperature map of the island as a function of bias and gate voltages to the QD junction. At the same time, an additional and constant heating power of 5 fW is applied to the island. The light blue region corresponds to the situation in which electron transport through the QD is blocked and the island temperature is defined by the thermal balance between the heat input and losses to the colder environment, just as discussed in detail in [87]. Close to the degeneracy point, the island cools, essentially not because of the above-described refrigerator effect, but simply because the QD allows heat to flow to the drain. The novel thermal balance near equilibrium is still under analysis but

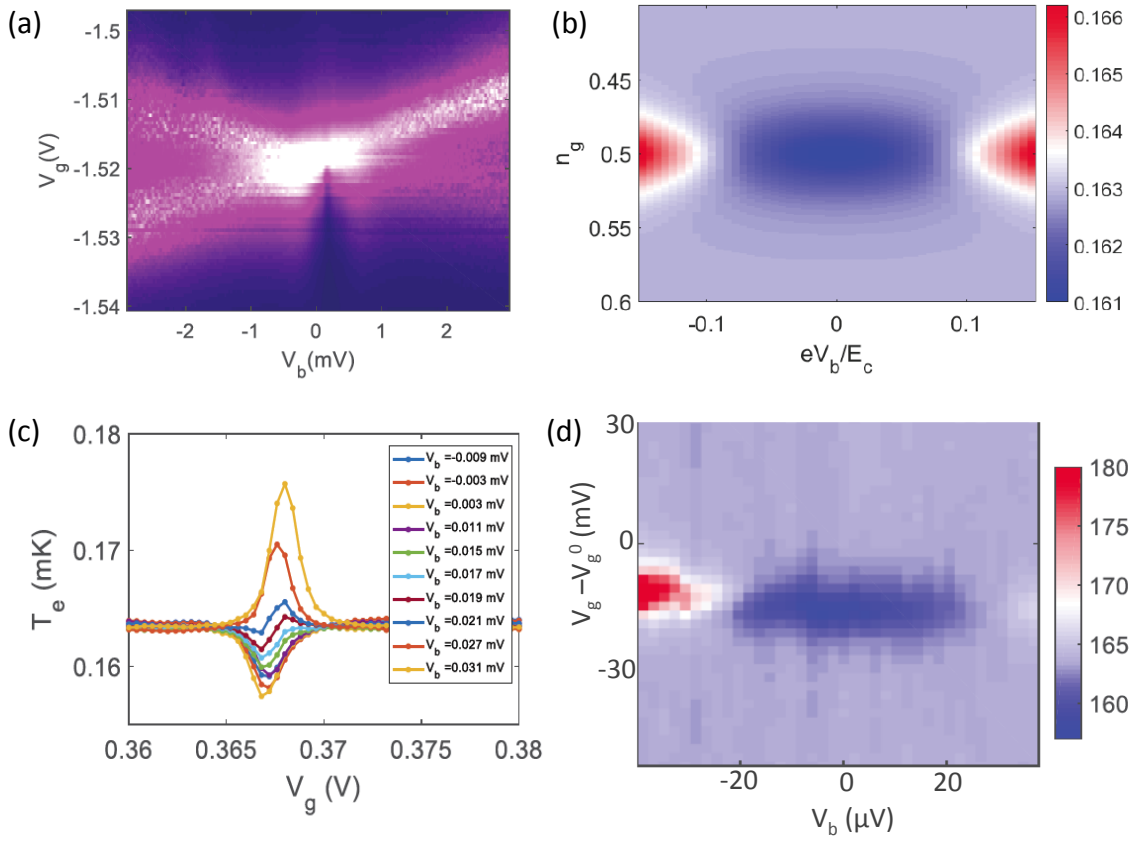

Figure 4.10: (a) Differential conductance of a QD junction around one of its degeneracy points, with charging energy 4 meV and $\gamma = 350\,\mu$eV. (b) Calculation of the temperature inside the *source* island as a function of the gate and bias voltages, applied to a single-electron transistor (continuous density of states), assuming an applied heating power of 5 fW, a resistance at high energies of 300 kΩ and $T_{\rm drain} = T_{\rm bath}$ =70 mK. The scale bar displays $T(V_b, V_g)$ in K. (c) Experimentally measured electron temperature in the source island as a function of gate at different biases applied to the QD junction. (d) Experimental temperature map of the source island $T(V_b, V_g)$ in units of mK.

should eventually allow extending our experiments on the Wiedemann-Franz law from a SET to a single quantum level junction, in which cotunneling plays a crucial role.

From the charge transport experiments on the same device (Fig. 4.10a), we can determine the tunnel coupling, which we find from the widths of the Coulomb diamond edges to be on the order of 350 μeV. This energy scale is larger than both the bias voltage energy and k_BT. At large biases we can quantitatively determine the Joule heat released to the lead formed by the island, by monitoring its temperature (Fig. 4.10d). This is perhaps the first *Coulomb diamond plot* of a QD junction based on a temperature measurement rather than a charge conductance. A rather striking feature in this temperature map is the small region near a constant bias $V_b = +25\mu$V (Fig. 4.10c), at which a temperature inversion with respect to the background temperature is observed as the QD chemical potential crossed both leads' Fermi levels. Such a behavior cannot be understood using an SET picture, which leads to the calculation in Fig. 4.10b. The understanding of how a QD with such a large tunnel coupling can still provide the energy selectivity required for the above-described scenario is still under investigation and analysis.

4.3 Scanning probe microscopy approach to subgap physics in superconductors

As discussed in chapter 3, most of the scanning probe experiments performed so far in the sionludi at Institut Néel were conducted on graphene, taking advantage of the inert surface of graphene which does not necessarily require *in situ* surface preparation. However, in order to move to the physics related to superconductivity and develop the full potential offered by dilution-refrigerated experiments, such a UHV preparation chamber is key. The integration of such a chamber to a dilution-refrigerated scanning probe microscope at Institut Néel is the fruit of a collaboration with Katharina Franke at FU Berlin. In the following are described a few instrumental and physical aspects of this collaboration.

4.3.1 STM with a gate

One drawback of STM is that the current through a particular junction can be controlled only by essentially two control knobs: the applied bias voltage and the tip height. My proposal is to go one step further, to insert a third electrode and to actually create a device, by gating a single molecule or quantum dot STM experiment. The gate can then be utilized to tune the quantum dot into a particular energy level or quantum state, such as discussed in chapter 1. By making STM and device physics meet, we will study the competition of diverse quantum many-body effects at play here, such as electron interactions, Kondo correlations and superconductivity.

Recently, remote gating of molecules or atoms adsorbed on graphene has been reported in an STM experiment [214,215]. Adsorbates usually couple only weakly to graphene and an overall backgate potential can be applied through the graphene. The achievable gate modulation remained however weak, with a gate coupling $\alpha = dE/d(eV_g) < 0.004$, insufficient for changing the charge state at equilibrium. Further, the choice of a graphene substrate strongly restricts the engineering possibilities of the molecule-substrate interactions. Finally, a graphene substrate is not suited for our study, which ultimately targets inducing superconducting correlations from the substrate to the molecule.

Introducing a gate electrode on a conductive surface implies some electrical isolation, a condition that is not easily compatible with the requirements of STM. Using clean-room nanofabrication techniques, we will fabricate *ex situ* bilayer structures on an insulating substrate, similar to the one shown in Fig. 4.11a, that is, with an undercut. If a thin metallic film is then evaporated on the sample *in situ*, the lower layer is still electrically isolated from the one on top of the bilayer thanks to the shadowing provided by the undercut. The two isolated metallic structures provide the gate electrode and the substrate, respectively.

The adsorption of a molecule on a metallic surface usually leads to a fixed energy level alignment of the molecular states with respect to the metal's Fermi level. Only in the weak coupling regime, with a sizable tunnel barrier and a smaller capacitive coupling to the substrate C_s, the external modulation of the molecular levels by a gate potential is possible. One key requirement for realizing gated STM on adsorbed molecules/QDs is thus to ensure sufficient QD-substrate capacitive decoupling as to allow for efficient gate modulation of the molecule's chemical potential (large gate capacitive level arm α). The suitable coupling with the substrate can be either tuned by ligand-design or the use of insulating thin film barriers, such as CuN or NaCl. These barriers can be grown in situ with epitaxial quality, before molecule deposition. It is however essential for the investigation of quantum coherent effects, that a sufficient tunnel coupling is also maintained. It is thus planned to systematically and quantitatively characterize achievable (γ_s, C_s) parameters in different QD-barrier-substrate systems. In each system, we will extract both quantities from tunnel spectroscopies at different gate voltages.

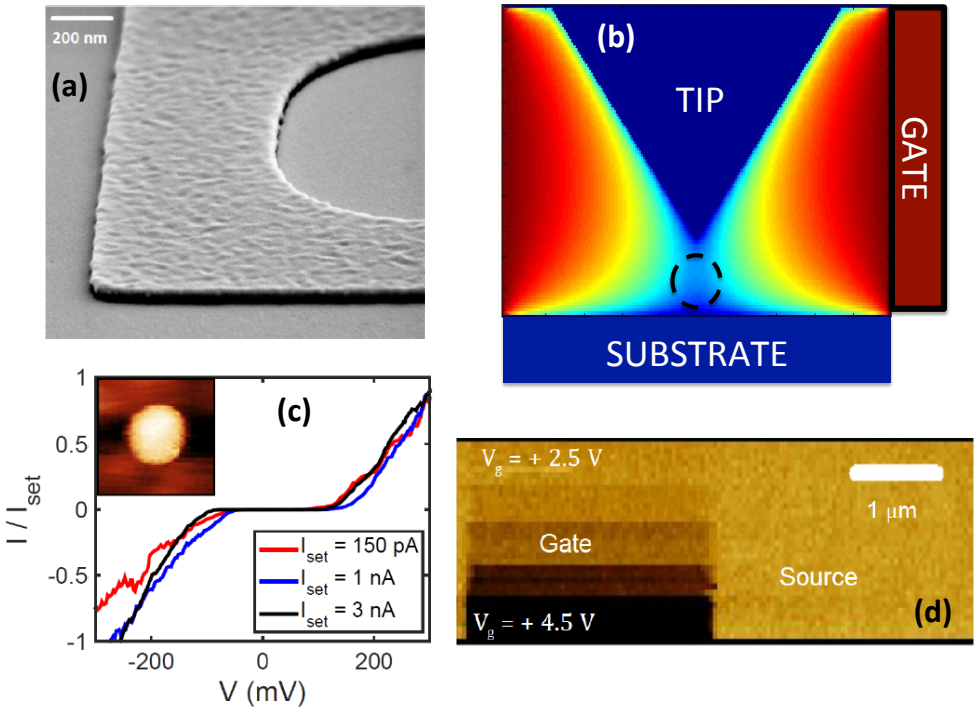

Figure 4.11: (a) Scanning electron micrograph of nanostructured STM gate. The entire surface is metal covered, yet both structures are galvanically isolated from each other. (b) 2D simulation of the achievable electrostatic gating in such a configuration, assuming a pyramidal tip. The lever arm α depends on the size of the QD, and can reach between $\sim 10^{-4}$ for a fullerene and 2×10^{-2} for a 10 nm nanoparticle. A more realistic 3D simulation of the screening by the tip would lead to larger values of α. (c) Preliminary scanning tunneling spectroscopy experiments by Alessandro De Cecco on functionalized Au nanoparticles, showing Coulomb blockade. The inset shows the topography of the 8 nm Au nanoparticle on which the spectra are taken. (d) Electrostatic force microscopy (EFM) image taken at the interface between the gate and the substrate layers in a device as shown in (a). As the gate voltage is cranked up (the source is grounded), the EFM contrast increases, demonstrating the electrical continuity of the gate electrode and its galvanic isolation from the source.

4.3.2 Ultra-high vacuum preparation chamber

In the frame of the project described with more details in the next section, we have started designing a UHV preparation chamber, which will be coupled to the existing inverted dilution cryostat used for the scanning probe microscopy experiments described in chapter 3. In order to ensure reliable tip and sample handling under UHV conditions, we will use a commercial cryogenic AFM-STM head, the Tribus Ultra from from Sigma Surface Science.

Many (although not all, as for example the setup in AG Wulfhekel at KIT) dilution-refrigerated UHV STM experiments use a vertical (top- or bottom-) loading geometry. This implies severe technical complications, associated to the long mechanical path to the heart of the experiment and difficulties with handling the successive thermal radiation screens. The situation is much simpler for the lateral loading mechanisms used in virtually all commercially available UHV-STM setups operating in the 1-10 K range, in which the sample exchange is handled by a short wobble stick and the opening of the radiation shields is well mastered, under comfortable optical supervision. We will take advantage of the peculiar and compact geometry of the Grenoble inverted dilution cryostat (*sionludi*), which is not surrounded by a helium bath, to transpose the principle of the lateral UHV loading mechanism to a dilution-refrigerated experiment. The

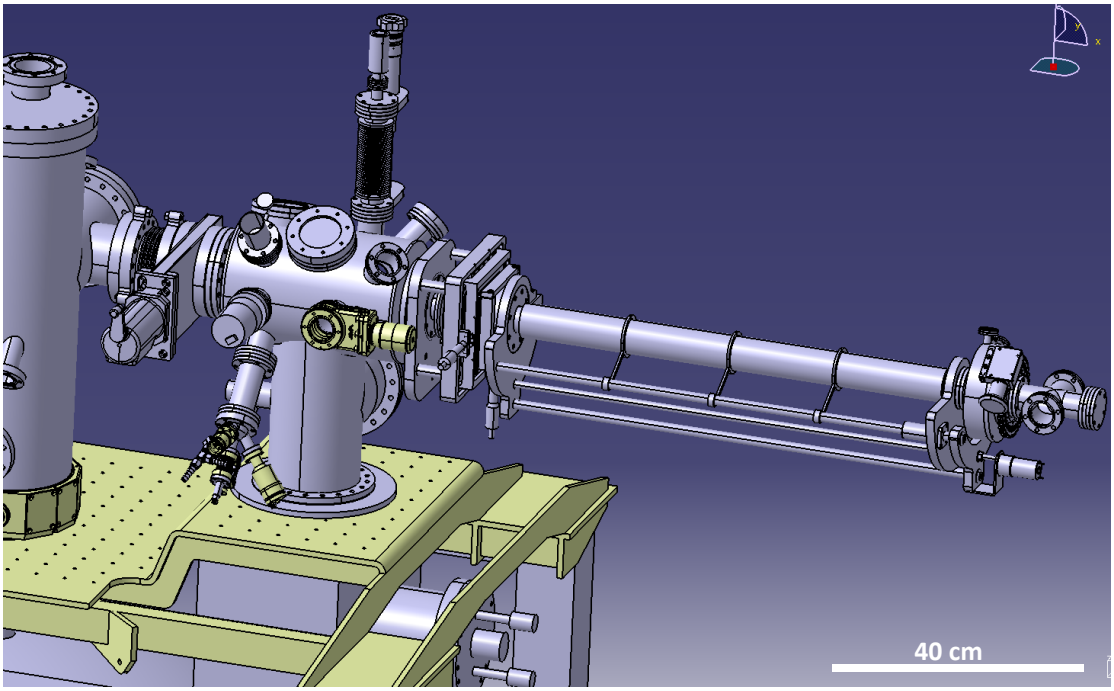

Figure 4.12: Preliminary drawing of the UHV chamber, connected to the *sionludi* (left-hand side) and an anti-vibration table, which will be realized by Axesstech (drawing courtesy Cyril Bruyère and Valentin Dargaud).

thermal screens will be handled as in 4K experiments, with the only difference of an extra shield at lower temperatures. Thus, we also target full compatibility with the higher-temperature standards, including standard tip and sample holders.

The UHV surface preparation chamber (Fig. 4.12) will operate in the low 10^{-10} mbar range. It will include an ion gun for in situ surface oxide removal, an electron-beam evaporator for depositing thin films of metals and molecules, and a heating stage for annealing the sample. More involved surface elaboration processes are not planned; however, the chamber can be connected to a UHV suitcase, which can be coupled to other UHV facilities in Grenoble. We foresee the delivery of all elements by the end of 2018.

4.3.3 Scanning Josephson tunneling spectroscopy

From a two-months research visit to the group of K. Franke at FU Berlin in 2016 began a collaboration which led to a joint ANR-DFG project (JoSpec), started in 2018. The project target is to gain an understanding of the superconducting state in the vicinity of magnetic nanostructures and to develop a broader toolbox for experimental checks of the topological nature of the subgap states, based on combining scanning tunneling spectroscopies, local Josephson current measurements, and their microwave responses. The main questions that will be addressed are:

- **How do Shiba states affect the Josephson current?** In typical Scanning Tunneling Spectroscopy (STS) experiments, the tunnelling current is measured in the low-conductance regime, where single-electron tunnelling dominates. When the tip is brought into closer distance, Andreev reflections can give rise to a Josephson current at zero voltage. The insertion of mesoscopic magnetic structures into the Josephson junction leads to a modification of the Josephson current due to a shift in the quantum phase difference through the junction. We foresee revealing experimentally the role of Shiba states arising from atomic-scale magnetic structures, such as single atoms and ferromagnetic nanostructures, in the dc Josephson transport.

- **How large is the superconducting order parameter Δ near a single magnetic impurity?** The strength of the Josephson coupling carries the signature of the magnitude of the local superconducting order parameter Δ. Theory predicts a local renormalization of Δ when Shiba states are present [16,216]. Δ is also predicted to undergo an abrupt change, when crossing the quantum phase transition between a screened and non-screened impurity. STS is not well suited to determine the size of the superconducting gap, because the spectrum is always dominated by the density of states of the final state of the tunnelling process, which is the bulk superconductor. In contrast, the Josephson current is expected to be a local property and therefore suited for an accurate determination of local changes in Δ. Hence, we aim at mapping the Josephson current around single atoms and around designed magnetic nanostructures.

- **Can one-dimensional magnetic chains or two-dimensional islands on a superconducting surface bear a non-trivial topological character?** There is a very active research field on the topological nature of induced superconductivity in magnetic nanostructures [217–219]. One-dimensional magnetic chains on the strongly spin-orbit coupled superconductor Pb are the prime example of many theoretical considerations predicting topological superconductivity and Majorana zero-modes [220]. Although many indications point to the existence of Majorana modes, complete evidence cannot be obtained from conventional STS. More conclusive evidence is expected from the supercurrent and its response to a microwave excitation. Such signatures would be directly accessible in transport experiments along the chains [221]. However, this is not possible for the atomic-scale chains on Pb(110). Therefore, the plan is to investigate whether the microwave response of the Josephson current between the tip and the chain transport is affected by zero-energy modes.

Josephson spectroscopy

The first proposals [21,222] and experimental attempts [223] to establish a Josephson current in a STM appeared around 2000. Because tunneling spectroscopies in high-T_c materials are rather smeared and because the Josephson coupling depends on the superconducting gap Δ, measuring the critical current provides a more sensitive tool for measuring local variations of the pairing amplitude [224]. Type-I superconducting tip and substrate combinations have been used only very recently in experiments going beyond the pioneering work by Naaman *et al.* [223]. The Princeton group compared the sub-gap density of states produced by Fe adatoms on Pb(110) with maps of the Josephson current amplitude in the same region, showing a 50% decrease of the latter in the vicinity of the impurity [225]. The Stuttgart group has recently made use of Josephson current measurements to gain information about the electromagnetic admittance of the tunnel junction environment [226]. This knowledge could then be used to explain and model the finite resolution of tunnel spectroscopies, obtained in the same environment but at larger junction normal state resistance R_n.

Concerning the above-cited works, it is essential to stress that all have been performed using the well-established STM technique of voltage-biased tunnel junctions. In case of a voltage bias, the Josephson coupling manifests as an anomaly in the $I(V)$ curves at zero energy, that is well described by the Ivanchenko-Zilberman formalism [227], or $P(E)$ theory in more modern words. However, the amplitude of the current anomaly near zero bias voltage represents only a vanishing fraction of the true Josephson critical current I_c, a quantity that can only be assessed using a current bias. Applying a current bias to a high impedance junction is however a true challenge. The situation is even worse when the same impedance has to be constantly monitored and adjusted using a feedback loop, as is typically the case in STM. A single, very recent publication [228] has demonstrated actual current bias in a superconducting STM junction. Notably, even in this work the observed switching current is more than two orders of magnitude smaller than I_c, an effect that is attributed to the coexistence of strong fluctuations and strong damping in the quantum phase dynamics.

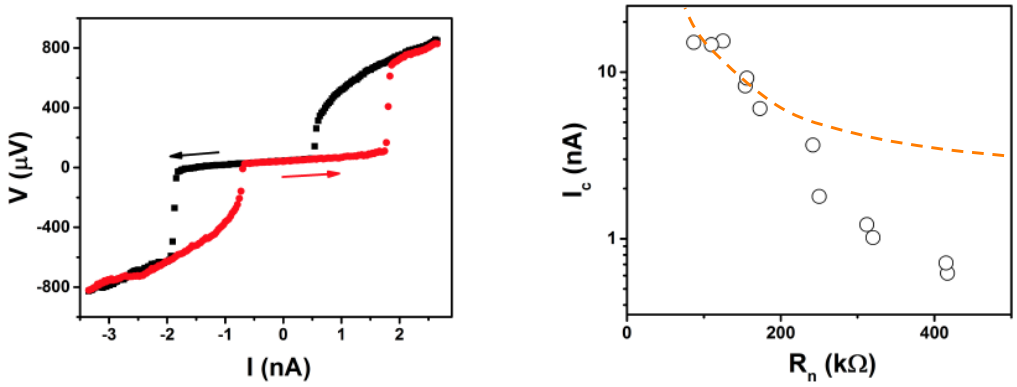

Figure 4.13: **(Left):** Josephson current measurement in 250 kΩ Pb-Pb tunnel junction in the STM at FU Berlin, displaying a switching current of nearly 2 nA at 1.5 K. **(Right):** Switching current versus normal state tunneling resistance. The dashed line shows the Ambegaokar-Baratoff limit.

Microwave response of superconducting junctions

As discussed in section 2.1.2, adding a microwave component at frequency f to the current bias in a Josephson junction can lead to a phase locking of the dynamics of quantum phase φ across the junction to multiples n of f, such that the quantum phase φ hops between n minima of the Josephson potential per drive cycle. Through the second Josephson relation, this produces a quantized non-zero dc voltage drop, $V = nhf/2e$, with h the Planck constant and $2e$ the charge of a Cooper pair, called Shapiro steps. Beyond metrological applications in voltage standards, the microwave response of a Josephson junction contains valuable information about the phase and quasi-particle dynamics in the junction [94, 100]. It was proposed that the presence of a 4π-periodic component in the $E(\varphi)$ dispersion relation of a junction could be detectable in the microwave response, through to the disappearance of the odd-n Shapiro steps [221, 229]. The microwave properties of Josephson junctions have thus received strong renewed attention in recent years, for the quest of signatures of Majorana particles in topological superconducting junctions [108, 230].

First results

In the frame of my visits to Berlin, we have jointly implemented a true current (rather than voltage) bias to the STM junction in an CreaTec STM with base temperature 1.5 K in Berlin. This technique is at the very opposite of the traditional STM approach, in which the voltage-biased tunnel junction itself is always the part of the circuit with the highest impedance. We have measured the voltage drop across the tunnel junction and observed the characteristic features of a Josephson supercurrent flow (Fig. 4.13, left). This is to our knowledge a premiere, except for one very recent publication in the field [228]. As opposed to that work however, our junctions display hysteretic features and the amplitude of the switching current I_s is close to the Ambegaokar-Baratoff limit [231], $R_n I_c = (\pi/3)\Delta/\mathrm{e}$ (Fig. 4.13, right), demonstrating that the dynamics of the quantum phase φ across the junction is not dominated by environmental noise. Note that due to the small critical currents, the relatively elevated temperatures and the bulk geometry of both the tip and the sample, thermal runaway is negligible here and the hysteresis is of capacitive origin.

The Berlin team has further recently implemented a microwave line to the STM, acting as an antenna to the tunnel junction. We have performed tunneling spectroscopies in the voltage bias mode on the bulk Pb surface in the presence of a 40 GHz microwave excitation, both in the sequential tunneling regime and at low tunneling resistances (Fig. 4.14). The results can be interpreted in the frame of the Tien-Gordon model [232] of photon-assisted tunneling of electrons and Cooper pairs in superconducting tunnel junctions, and can be related to experiments both in mechanical break junctions [233] and, more recently, STM experiments [234] with superconducting contacts.

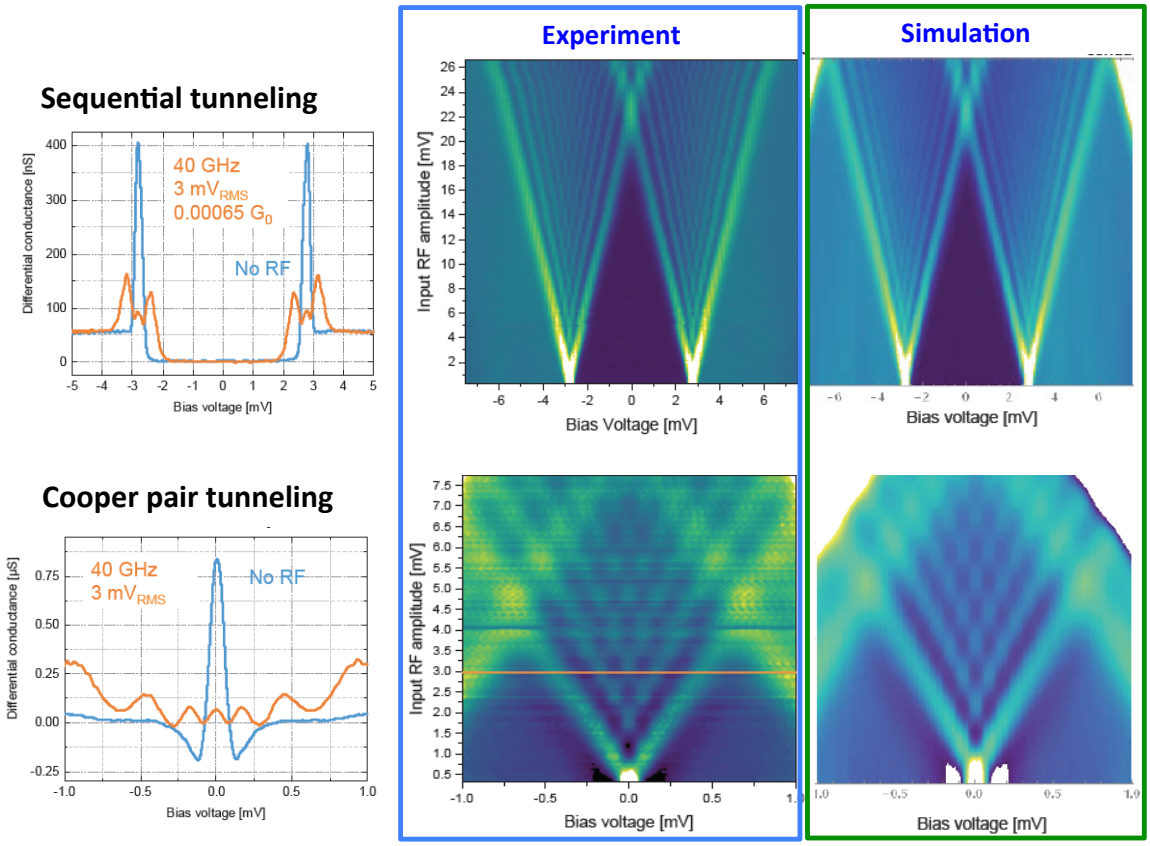

Figure 4.14: Experimental data and associated Tien-Gordon model-based calculation of the differential tunneling conductance as a function of dc bias and ac drive amplitude, between a superconducting tip and surface. The calculation of the top line assumes sequential tunneling processes only, and yields good agreement with the data taken with $R_n = 20$ MΩ. The calculation of the bottom line assumes Andreev transport only, yielding also good agreement with the data taken at small bias voltages and $R_n = 200$ kΩ. The plots on the left show horizontal line cuts through the respective experimental maps. $T = 1.5$ K, $f = 40$ GHz.

Photon-assisted tunneling

Consider a superconducting tunnel junction with a dc voltage bias V_b. The current is the sum of two contributions, $I^{(1)}(V_b) + I^{(2)}(V_b)$, which stem from the tunneling of single electrons and of Cooper pairs, respectively. In the presence of an additional microwave voltage drive of amplitude A and angular frequency ω, the Tien-Gordon model predicts the time-averaged current to be also the sum of two contributions $\mathcal{I}^{(p)}(V_b, A)$ (with $p = 1, 2$):

$$\mathcal{I}^{(p)}(V_b, A) = \sum_{\ell=-\infty}^{\infty} J_\ell^2 \left(\frac{peA}{\hbar\omega} \right) I^{(p)} \left(V_b - \frac{\ell\hbar\omega}{pe} \right). \tag{4.3.1}$$

Here, J_ℓ is again the Bessel function of order ℓ and the corresponding term in the sum corresponds to the absorption of ℓ photons. The tunnel conductance with applied ac drive calculated from Eq. (4.3.1) leads to the two plots shown in the right-hand columns in Fig. 4.14. The only input to the calculation are the experimentally measured dc currents $I^{(p)}(V_b)$. In the high resistance tunnel junction case (top line), we assume the only dc contribution to be sequential ($p = 1$), whereas in the low tunnel resistance case and at energies well below the gap, the only dc contribution is taken to stem from Cooper pairs ($p = 2$).

The results can be interpreted both from a semi-classical or a or quantum-mechanical point of view.

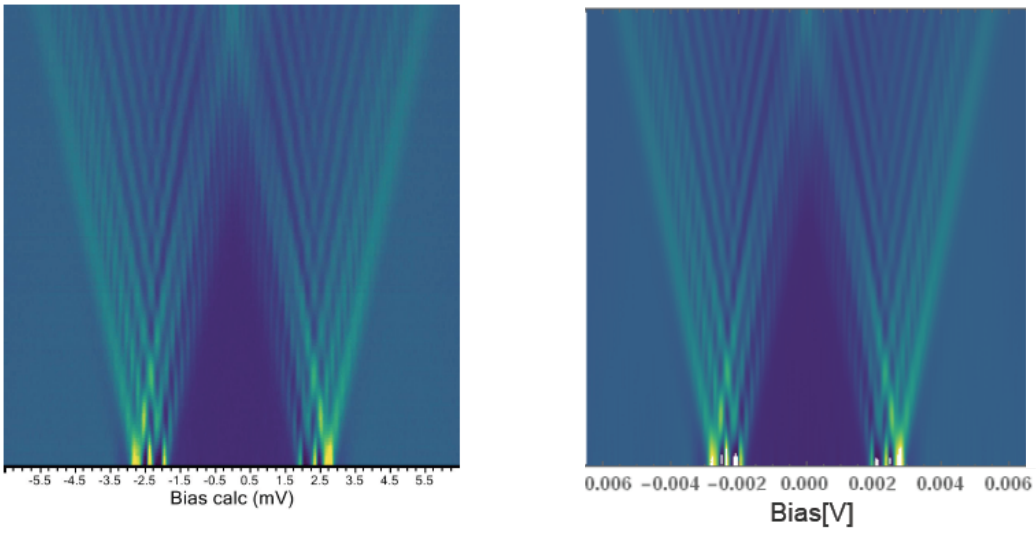

Figure 4.15: Experimental data (left) and associated Tien-Gordon model-based calculation (right) of the differential tunneling conductance as a function of dc bias and ac drive amplitude, on a magnetic impurity on Pb(111). The calculation assumes sequential tunneling processes only, and yields good agreement with the data, implying that Andreev processes play a negligible role in the transport through the subgap states ($T = 1.5$ K, $R_n = 20$ MΩ, $f = 40$ GHz).

Consider the convergent set of bright lines in the high-impedance experiment of Fig. 4.14. They simply correspond to the lowering of the tunneling threshold in V_b from $2\Delta/e$ to $2\Delta/e - A$ as an ac drive of amplitude A is added. All other bright lines (resonances) in this plot can also be drawn back to similar semi-classical arguments.

A closer inspection (better visible in Fig. 4.15 for a simple question of scale) reveals that these tilted lines are in reality composed of a set of vertical segments. Each of these segments is spaced along the bias voltage axis by $\hbar\omega/e$. The nth resonance thus corresponds to a process in which n photons of energy $\hbar\omega$ are absorbed, which provides the quantum picture of the photon-assisted charge transfer processes. Interestingly, in the case of Cooper pair transport (bottom line of Fig. 4.14), the resonances are vertically spaced by $\hbar\omega/(2e)$ rather than $\hbar\omega/e$, which confirms that the elementary charge at play is $2e$ here.

It is worth noting that similar findings have already been reported in dilution-refrigerated experiments with break junctions [233] and an STM [234]. One technical novelty here is that the experiments could be performed at 1.5 K, owing to the extremely high-bandwidth microwave capabilities (40 GHz, generator-limited) of the setup in Berlin. Further, Fig. 4.15 shows the same method applied to a tunneling spectroscopy on a magnetic impurity displaying two Shiba states, visible as tunneling resonances at voltages 1.7 and 2.3 mV. The Berlin group has recently investigated the relative contribution of sequential and Andreev processes in transport through subgap states in dc STM-SQS experiments [38]. The experimental data in Fig. 4.15 are very well reproduced assuming a sequential contribution only, but we expect to find significant deviations from this, either by increasing the tunnel conductance (work in progress) or by working at lower temperatures.

Feasibility of coherent Cooper pair transfer in an STM junction

There is again a fundamental difference between the above microwave experiments and e.g. the transport experiments described in section 2.1.2, which is the bias: voltage in one case, current in the other. Because of the voltage bias, the above described STM microwave experiments call for incoherent transfer processes, both of single electrons and of Cooper pairs. For the planned experiments and the (non-)observation of

Shapiro steps, we need not only a current bias but also the Josephson energy $E_J = \hbar I_c/(2e)$, that is, the depth of the Josephson potential well to be larger than the temperature fluctuations $\sim k_B T$. Therefore, even in the experiment shown in Fig. 4.13a there is a finite voltage slope below the critical current, due to phase diffusion. As opposed to the SNS experiments, in which R_n is on the order of Ωs, here, a single quantum channel is involved and $R_n > h/(2e^2)$ is 4 orders of magnitude larger.

Aassuming $\Delta = 1.3$ meV, as for Pb, and a tunneling resistance $R_n = 50$ kΩ, which is about the smallest tunneling resistance at which a point-like Pb-Pb junction can be stabilized without atoms at the apex reconfiguring, the maximum achievable I_c is then 26 nA and the associated $E_J \approx 50\,\mu$eV. This is less than $k_B T \sim 100\,\mu$eV in the best case in a pumped-helium STM, meaning that preserving quantum coherence in a Josephson weak link made of a single quantum transport channel at 1.3 K is rather challenging, if not impossible. For this reason, we have not yet succeeded in observing clear Shapiro steps in current-biased STM experiments in Berlin.[1] Eventually, working in a dilution-refrigerated experiment will be the more viable solution on the long run for studying Josephson physics in single quantum conduction channels.

[1] Because E_J is not so much smaller than $k_B T$, there is a chance that using NbN tips, which are much harder than Pb (allowing for smaller R_n) and have a gap in excess of 2.5 meV, this might be achieved even at relatively high temperatures. We have tested NbN-coated tips in Grenoble (collaboration with Max Hofheinz, previously at INAC/Grenoble, now in Sherbrooke) and indeed observed a well-developed, sharp tunneling gap with the expected amplitude.

Conclusion

The last few years have allowed improving our ability to integrate single quantum dots into quantum circuits. Lately, it has been possible in our team to consider combining such junctions with more elaborate structures, such as SINIS or SNS junctions. This allows nowadays performing thermometry in the vicinity of the QD junction, but it could also be extended to other device types, such as spin valves or interference experiments. The other experimental technique at hand in our laboratory, cryogenic scanning tunneling microscopy, has so far remained mainly focussed on graphene studies. However, the ongoing implementation of a preparation chamber will allow studying a much bigger diversity of systems in a near future. Finally, to the above dc transport probes came recently the investigations of quantum devices using a radiofrequency or microwave drive.

Many exciting developments could be imagined for the coming years by combining the above experimental techniques. The Josephson spectroscopy project on magnetic nanostructures on superconducting substrates goes towards that direction, and so is the gated-STM project, but many other "marriages" can be imagined. For example, the recent development in the group of Eli Zeldov of scanning SQUIDs as a tool to map dissipation in quantum circuits is one really fascinating application, combining the physics of scanning probe microscopy, nanothermics and Josephson junctions [235]. Why not imagine for example performing an electron turnstile experiment using an STM tip as a contact? Or using a mobile tip for the QD thermoelectricity experiments would also present significant advantages. The list is long... but the time is short.

References

[1] S De Franceschi, L Kouwenhoven, C Schönenberger, and W Wernsdorfer. Hybrid superconductor–quantum dot devices. *Nature Nanotechnol.*, 5:703–711, 2010.

[2] H Park, A K L Lim, A P Alivisatos, J Park, and P L McEuen. Fabrication of metallic electrodes with nanometer separation by electromigration. *Appl. Phys. Lett.*, 75:301–303, 1999.

[3] H Park and P L McEuen. Nano-mechanical oscillations in a single-C_{60} transistor. *Nature*, 407:57–60, 2000.

[4] N Roch. *Transistors à molécule unique : des effets Kondo exotiques à la spintronique moléculaire.* PhD thesis, Université Joseph Fourier, 2009.

[5] D M T van Zanten. *Quantum dynamics revealed in weakly coupled quantum dot - superconductor turnstiles.* PhD thesis, Université Grenoble Alpes, 2015.

[6] N Roch, S Florens, V Bouchiat, W Wernsdorfer, and F Balestro. Quantum phase transition in a single-molecule quantum dot. *Nature*, 453:633–637, 2008.

[7] Roch, N and Winkelmann, C B and Florens, S and Bouchiat, V and Wernsdorfer, W and Balestro, F. Kondo effects in a C_{60} single-molecule transistor. *physica status solidi (b)*, 245:1994–1997, 2008.

[8] J O Island, R Gaudenzi, J de Bruijckere, E Burzurí, C Franco, M Mas-Torrent, C Rovira, J Veciana, T M Klapwijk, R Aguado, et al. Proximity-induced Shiba states in a molecular junction. *Phys. Rev. Lett.*, 118:117001, 2017.

[9] F Kuemmeth, K I Bolotin, S-F Shi, and D C Ralph. Measurement of Discrete Energy-Level Spectra in Individual Chemically Synthesized Gold Nanoparticles. *Nano Lett.*, 8:4506–4512, 2008.

[10] L Bernard, M Calame, S J van der Molen, J Liao, and C Schönenberger. Controlled formation of metallic nanowires via Au nanoparticle ac trapping. *Nanotechnology*, 18:235202, 2007.

[11] K I Bolotin, F Kuemmeth, A N Pasupathy, and D C Ralph. Metal-nanoparticle single-electron transistors fabricated using electromigration. *Appl. Phys. Lett.*, 84:3154, 2004.

[12] M Buitelaar, T Nussbaumer, and C Schönenberger. Quantum Dot in the Kondo Regime Coupled to Superconductors. *Phys. Rev. Lett.*, 89:256801, 2002.

[13] E Bonet, M Deshmukh, and D C Ralph. Solving rate equations for electron tunneling via discrete quantum states. *Phys. Rev. B*, 65:045317, 2002.

[14] M-S Choi, M Lee, K Kang, and W Belzig. Kondo effect and Josephson current through a quantum dot between two superconductors. *Phys. Rev. B*, 70:020502(R), 2004.

[15] J Bauer, A Oguri, and A C Hewson. Spectral properties of locally correlated electrons in a Bardeen–Cooper–Schrieffer superconductor. *Journal of Phys.: Condensed Matter*, 19:486211, 2007.

[16] T Meng, S Florens, and P Simon. Self-consistent description of Andreev bound states in Josephson quantum dot devices. *Phys. Rev. B*, 79:224521, 2009.

[17] D C Ralph, C T Black, and M Tinkham. Spectroscopic measurements of discrete electronic states in single metal particles. *Phys. Rev. Lett.*, 74:3241, 1995.

[18] Winkelmann, C B and Roch, N and Wernsdorfer, W and Bouchiat, V and Balestro, F. Superconductivity in a single-C_{60} transistor. *Nature Phys.*, 5:876, 2009.

[19] C T Black, D C Ralph, and M Tinkham. Spectroscopy of the Superconducting Gap in Individual Nanometer-Scale Aluminum Particles. *Phys. Rev. Lett.*, 76:688, 1996.

[20] L Solymar. *Superconducting Tunneling and Applications*. Chapman and Hall, London, 1972.

[21] S H Pan, E W Hudson, and J C Davis. Vacuum tunneling of superconducting quasiparticles from atomically sharp scanning tunneling microscope tips. *Appl. Phys. Lett.*, 73:2992, 1998.

[22] S-H Ji, T Zhang, Y-S Fu, X Chen, X-C Ma, J Li, W-H Duan, J-F Jia, and Q-K Xue. High-resolution scanning tunneling spectroscopy of magnetic impurity induced bound states in the superconducting gap of Pb thin films. *Phys. Rev. Lett.*, 100:226801, 2008.

[23] K J Franke, G Schulze, and J I Pascual. Competition of superconducting phenomena and Kondo screening at the nanoscale. *Science*, 332:940–944, 2011.

[24] J D Pillet, C H L Quay, P Morfin, C Bena, A Levy Yeyati, and P Joyez. Andreev bound states in supercurrent-carrying carbon nanotubes revealed. *Nature Phys.*, 6:965–969, 2010.

[25] A Levy Yeyati, J C Cuevas, A López-Dávalos, and A. Martín-Rodero. Resonant tunneling through a small quantum dot coupled to superconducting leads. *Phys. Rev. B*, 55:R6137, 1997.

[26] K Kang. Transport through an interacting quantum dot coupled to two superconducting leads. *Phys. Rev. B*, 57:11891, 1998.

[27] D M Basko. Landau-Zener-Stückelberg physics with a singular continuum of states. *Phys. Rev. Lett.*, 118:016805, 2017.

[28] J Pekola, V Maisi, S Kafanov, N Chekurov, A Kemppinen, Y Pashkin, O P Saira, M Möttönen, and J Tsai. Environment-Assisted Tunneling as an Origin of the Dynes Density of States. *Phys. Rev. Lett.*, 105:026803, 2010.

[29] P Jarillo-Herrero, J Kong, H S J Van Der Zant, C Dekker, L P Kouwenhoven, and S De Franceschi. Orbital Kondo effect in carbon nanotubes. *Nature*, 434:484–488, 2005.

[30] Z Iftikhar, S Jezouin, A Anthore, U Gennser, F D Parmentier, A Cavanna, and F Pierre. Two-channel Kondo effect and renormalization flow with macroscopic quantum charge states. *Nature*, 526:233–236, 2015.

[31] D Goldhaber-Gordon, H Shtrikman, D Mahalu, D Abusch-Magder, U Meirav, and M A Kastner. Kondo effect in a single-electron transistor. *Nature*, 391:156–159, 1998.

[32] S M Cronenwett, T H Oosterkamp, and L P Kouwenhoven. A tunable Kondo effect in quantum dots. *Science*, 281:540–544, 1998.

[33] T Yoshioka and Y Ohashi. Numerical renormalization group studies on single impurity Anderson model in superconductivity: A unified treatment of magnetic, nonmagnetic impurities, and resonance scattering. *Jour. Phys. Soc. Japan*, 69:1812–1823, 2000.

[34] R Maurand, T Meng, E Bonet, S Florens, L Marty, and W Wernsdorfer. First-Order 0-π Quantum Phase Transition in the Kondo Regime of a Superconducting Carbon-Nanotube Quantum Dot. *Phys. Rev. X*, 2:011009, 2012.

[35] J A van Dam, Y V Nazarov, E P A M Bakkers, S De Franceschi, and L P Kouwenhoven. Supercurrent reversal in quantum dots. *Nature*, 442:667–670, 2006.

[36] J-P Cleuziou, W Wernsdorfer, V Bouchiat, Th Ondarçuhu, and M Monthioux. Carbon nanotube superconducting quantum interference device. *Nature Nanotech.*, 1:53–59, 2006.

[37] R S Deacon, Y Tanaka, A Oiwa, R Sakano, K Yoshida, K Shibata, K Hirakawa, and S Tarucha. Tunneling Spectroscopy of Andreev Energy Levels in a Quantum Dot Coupled to a Superconductor. *Phys. Rev. Lett.*, 104:076805, 2010.

[38] F Ruby, Mand Pientka, Y Peng, F von Oppen, B W Heinrich, and K J Franke. Tunneling Processes into Localized Subgap States in Superconductors. *Phys. Rev. Lett.*, 115:087001, 2015.

[39] L G Aslamazov and M V Fistul. Resonant tunneling in superconductor-semiconductor-superconductor junctions. *Sov. Phys.-JETP*, 56:681, 1982.

[40] C W J Beenakker and H van Houten. Josephson current through a superconducting quantum point contact shorter than the coherence length. *Phys. Rev. Lett.*, 66:3056, 1991.

[41] M Tinkham. *Introduction to Superconductivity*. Dover Publications, 2004.

[42] P Joyez, P Lafarge, A Filipe, D Estève, and M H Devoret. Observation of parity-induced suppression of Josephson tunneling in the superconducting single electron transistor. *Phys. Rev. Lett.*, 72:2458, 1994.

[43] P Jarillo-Herrero, J A Van Dam, and L P Kouwenhoven. Quantum supercurrent transistors in carbon nanotubes. *Nature*, 439:953–956, 2006.

[44] H I Jørgensen, T Novotnỳ, K Grove-Rasmussen, K Flensberg, and P E Lindelof. Critical current 0-π transition in designed Josephson quantum dot junctions. *Nano Lett.*, 7:2441–2445, 2007.

[45] L J Geerligs, V F Anderegg, P A M Holweg, J E Mooij, H Pothier, D Estève, C Urbina, and M H Devoret. Frequency-locked turnstile device for single electrons. *Phys. Rev. Lett.*, 64:2691–2694, 1990.

[46] L P Kouwenhoven, A T Jason, N C van der Vaart, C J P M Harmans, and C T Foxon. Quantized current in a quantum-dot turnstile using oscillating tunnel barriers. *Phys. Rev. Lett.*, 67:1626–1629, 1991.

[47] H Pothier, P Lafarge, C Urbina, D Estève, and M H Devoret. Single-Electron Pump Based on Charging Effects. *Europhys. Lett.*, 17:249–254, 1992.

[48] J M Martinis, M Nahum, and H D Jensen. Metrological accuracy of the electron pump. *Phys. Rev. Lett.*, 72:904–907, 1994.

[49] Y Ono and Y Takahashi. Electron pump by a combined single-electron/field-effect- transistor structure. *Appl. Phys. Lett.*, 82:1221, 2003.

[50] M D Blumenthal, B Kaestner, L Li, S Giblin, T J B M Janssen, M Pepper, D Anderson, G Jones, and D A Ritchie. Gigahertz quantized charge pumping. *Nature Phys.*, 3:343–347, 2007.

[51] J P Pekola, J J Vartiainen, M Möttönen, O-P Saira, M Meschke, and D V Averin. Hybrid single-electron transistor as a source of quantized electric current. *Nature Phys.*, 4:120–124, 2008.

[52] B Kaestner, V Kashcheyevs, S Amakawa, M D Blumenthal, L Li, T J B M Janssen, G Hein, K Pierz, T Weimann, U Siegner, and H W Schumacher. Single-parameter nonadiabatic quantized charge pumping. *Phys. Rev. B*, 77:153301, 2008.

[53] V Siegle, C-W Liang, B Kaestner, H W Schumacher, F Jessen, D Koelle, R Kleiner, and S Roth. A molecular quantized charge pump. *Nano Lett.*, 10:3841–5, 2010.

[54] F Giazotto, P Spathis, S Roddaro, S Biswas, F Taddei, M Governale, and L Sorba. A Josephson quantum electron pump. *Nature Phys.*, 7:857–861, 2011.

[55] S P Giblin, M Kataoka, J D Fletcher, P See, T J B M Janssen, J P Griffiths, G A C Jones, I Farrer, and D A Ritchie. Towards a quantum representation of the ampere using single electron pumps. *Nature Commun.*, 3:930, 2012.

[56] B Roche, R-P Riwar, B Voisin, E Dupont-Ferrier, R Wacquez, M Vinet, M Sanquer, J Splettstoesser, and X Jehl. A two-atom electron pump. *Nature Commun.*, 4:1581, 2013.

[57] M R Connolly, K L Chiu, S P Giblin, M Kataoka, J D Fletcher, C Chua, J P Griffiths, G A C Jones, V I Fal'ko, C G Smith, and T J B M Janssen. Gigahertz quantized charge pumping in graphene quantum dots. *Nature Nanotechnol.*, 8:417–20, 2013.

[58] J P Pekola, O-P Saira, V F Maisi, A Kemppinen, M Möttönen, Y A Pashkin, and D V Averin. Single-electron current sources: Toward a refined definition of the ampere. *Rev. Mod. Phys.*, 85:1421–1472, 2013.

[59] G Yamahata, K Nishiguchi, and A Fujiwara. Gigahertz single-trap electron pumps in silicon. *Nature Commun.*, 5:1–7, 2014.

[60] A Rossi, T Tanttu, K Y Tan, I Iisakka, R Zhao, K W Chan, G C Tettamanzi, S Rogge, A S Dzurak, and M Möttönen. An accurate single-electron pump based on a highly tunable silicon quantum dot. *Nano Lett.*, 14:3405–11, 2014.

[61] F Stein, D Drung, L Fricke, H Scherer, F Hohls, C Leicht, M Götz, C Krause, R Behr, E Pesel, K Pierz, U Siegner, F J Ahlers, and H W Schumacher. Validation of a quantized-current source with 0.2 ppm uncertainty. *Appl. Phys. Lett.*, 107:103501, 2015.

[62] G Fève, A Mahe, J-M Berroir, T Kontos, B Plaçais, D C Glattli, A Cavanna, B Etienne, and Y Jin. An on-demand coherent single-electron source. *Science*, 316:1169–1172, 2007.

[63] R P G McNeil, M Kataoka, C J B Ford, C H W Barnes, D Anderson, G A C Jones, I Farrer, and D A Ritchie. On-demand single-electron transfer between distant quantum dots. *Nature*, 477:439–442, 2011.

[64] S Hermelin, S Takada, M Yamamoto, S Tarucha, A D Wieck, L Saminadayar, C Bäuerle, and T Meunier. Electrons surfing on a sound wave as a platform for quantum optics with flying electrons. *Nature*, 477:435–438, 2011.

[65] J Dubois, T Jullien, F Portier, P Roche, A Cavanna, Y Jin, W Wegscheider, P Roulleau, and D C Glattli. Minimal-excitation states for electron quantum optics using levitons. *Nature*, 502:659–663, 2013.

[66] V Freulon, A Marguerite, J-M Berroir, B Plaçais, A Cavanna, Y Jin, and G Fève. Hong-Ou-Mandel experiment for temporal investigation of single-electron fractionalization. *Nature Commun.*, 6, 2015.

[67] Dmitri V Averin and J P. Pekola. Nonadiabatic Charge Pumping in a Hybrid Single-Electron Transistor. *Phys. Rev. Lett.*, 101:066801, 2008.

[68] van Zanten, D M T and Basko, D M and Khaymovich, I M and Pekola, J P and Courtois, H and Winkelmann, C B. Single Quantum Level Electron Turnstile. *Phys. Rev. Lett.*, 116:166801, 2016.

[69] van Zanten, D M T and Balestro, F and Courtois, H and Winkelmann, C B. Probing hybridization of a single energy level coupled to superconducting leads. *Phys. Rev. B*, 92:184501, 2015.

[70] F Giazotto, T Heikkilä, A Luukanen, A Savin, and J Pekola. Opportunities for mesoscopics in thermometry and refrigeration: Physics and applications. *Rev. Mod. Phys.*, 78:217–274, 2006.

[71] A Kemppinen, S Kafanov, Y A Pashkin, J S Tsai, D V Averin, and J P Pekola. Experimental investigation of hybrid single-electron turnstiles with high charging energy. *Appl. Phys. Lett.*, 94:172108, 2009.

[72] H S Knowles, V F Maisi, and J P Pekola. Probing quasiparticle excitations in a hybrid single electron transistor. *Appl. Phys. Lett.*, 100:262601, 2012.

[73] S Nakamura, Y A Pashkin, J Tsai, and N Kaneko. Temperature dependence of single-electron pumping using a SINIS turnstile. *Physica C*, 504:93–96, 2014.

[74] O-P Saira, A Kemppinen, V F Maisi, and J P Pekola. Vanishing quasiparticle density in a hybrid Al/Cu/Al single-electron transistor. *Phys. Rev. B*, 85:012504, 2012.

[75] B Sothmann, R Sanchez, and Andrew N Jordan. Thermoelectric energy harvesting with quantum dots. *Nanotechnology*, 26:032001, 2015.

[76] Y Dubi and M Di Ventra. Heat flow and thermoelectricity in atomic and molecular junctions. *Rev. Mod. Phys.*, 83:131–155, 2011.

[77] O Chiatti, J T Nicholls, Y Y Proskuryakov, N Lumpkin, I Farrer, and D A Ritchie. Quantum thermal conductance of electrons in a one-dimensional wire. *Phys. Rev. Lett.*, 97:056601, 2006.

[78] M Banerjee, M Heiblum, A Rosenblatt, Y Oreg, D E Feldman, A Stern, and V Umansky. Observed quantization of anyonic heat flow. *Nature*, 545:75, 2017.

[79] K Schwab, E A Henriksen, J M Worlock, and M L Roukes. Measurement of the quantum of thermal conductance. *Nature*, 404:974, 2000.

[80] M Meschke, W Guichard, and J P Pekola. Single-mode heat conduction by photons. *Nature*, 444:187, 2006.

[81] L W Molenkamp, Th Gravier, H van Houten, O J A Buijk, M A A Mabesoone, and C T Foxon. Peltier coefficient and thermal conductance of a quantum point contact. *Phys. Rev. Lett.*, 68:3765–3768, 1992.

[82] E A Hoffmann, H A Nilsson, J E Matthews, N Nakpathomkun, A I Persson, L Samuelson, and H Linke. Measuring temperature gradients over nanometer length scales. *Nano Lett.*, 9:779–783, 2009.

[83] S Jezouin, F D Parmentier, A Anthore, U Gennser, A Cavanna, Y Jin, and F Pierre. Quantum limit of heat flow across a single electronic channel. *Science*, 342:601–604, 2013.

[84] L Cui, W Jeong, S Hur, M Matt, J C Klöckner, F Pauly, P Nielaba, J-C Cuevas, E Meyhofer, and P Reddy. Quantized thermal transport in single-atom junctions. *Science*, 355:1192–1195, 2017.

[85] N Mosso, U Drechsler, F Menges, P Nirmalraj, S Karg, H Riel, and B Gotsmann. Heat transport through atomic contacts. *Nature Nanotechnology*, 12:430, 2017.

[86] Pascal, L M A and Fay, A and Winkelmann, C B and Courtois, H. Existence of an independent phonon bath in a quantum device. *Phys. Rev. B*, 88:100502, 2013.

[87] Dutta, B and Peltonen, J T and Antonenko, D S and Meschke, M and Skvortsov, M A and Kubala, B and König, J and Winkelmann, C B and Courtois, H and Pekola, J P. Thermal conductance of a single-electron transistor. *Phys. Rev. Lett.*, 119:077701, 2017.

[88] W Wernsdorfer. From micro-to nano-squids: applications to nanomagnetism. *Superconductor Science and Technology*, 22:064013, 2009.

[89] Kumar, N and Fournier, T and Courtois, H and Winkelmann, C B and Gupta, A K. Reversibility of superconducting Nb weak links driven by the proximity effect in a quantum interference device. *Phys. Rev. Lett.*, 114:157003, 2015.

[90] Kumar, N and Winkelmann, C B and Biswas, S and Courtois, H and Gupta, A K. Controlling hysteresis in superconducting constrictions with a resistive shunt. *Superconductor Science and Technology*, 28:072003, 2015.

[91] Biswas, S and Winkelmann, C B and Courtois, H and Gupta, A K. Josephson Coupling in the Dissipative State of a Thermally Hysteretic μ-SQUID. *arXiv:1709.02569*, 2017.

[92] H Courtois, M Meschke, J T Peltonen, and J P Pekola. Origin of hysteresis in a proximity Josephson junction. *Phys. Rev. Lett.*, 101:067002, 2008.

[93] Samaddar, S and van Zanten, D M T and Fay, A and Sacépé, B and Courtois, H and Winkelmann, C B. Niobium-based superconducting nano-device fabrication using all-metal suspended masks. *Nanotechnology*, 24:375304, 2013.

[94] De Cecco, A and Le Calvez, K and Sacépé, B and Winkelmann, C B and Courtois, H. Interplay between electron overheating and ac Josephson effect. *Phys. Rev. B*, 93:180505, 2016.

[95] K K Likharev. *Dynamics of Josephson Junctions and Circuits*. Gordon and Breach, Philadelphia, 1991.

[96] H Courtois, P Gandit, B Pannetier, and D Mailly. Long-range coherence and mesoscopic transport in N–S metallic structures. *Superlattices and microstructures*, 25:721–732, 1999.

[97] L Angers, F Chiodi, G Montambaux, M Ferrier, S Guéron, H Bouchiat, and J C Cuevas. Proximity dc SQUIDs in the long-junction limit. *Phys. Rev. B*, 77:165408, 2008.

[98] S Shapiro. Josephson currents in superconducting tunneling: The effect of microwaves and other observations. *Phys. Rev. Lett.*, 11:80, 1963.

[99] K W Lehnert, N Argaman, H-R Blank, K C Wong, S J Allen, E L Hu, and H Kroemer. Nonequilibrium ac Josephson effect in mesoscopic Nb-InAs-Nb junctions. *Phys. Rev. Lett.*, 82:1265, 1999.

[100] P Dubos, H Courtois, O Buisson, and B Pannetier. Coherent low-energy charge transport in a diffusive SNS junction. *Phys. Rev. Lett.*, 87:206801, 2001.

[101] H le Sueur, P Joyez, H Pothier, C Urbina, and D Estève. Phase Controlled Superconducting Proximity Effect Probed by Tunneling Spectroscopy. *Phys. Rev. Lett.*, 100:197002, 2008.

[102] F Chiodi, M Aprili, and B Reulet. Evidence for two time scales in long SNS junctions. *Phys. Rev. Lett.*, 103:177002, 2009.

[103] B Dassonneville, M Ferrier, S Guéron, and H Bouchiat. Dissipation and supercurrent fluctuations in a diffusive normal-metal–superconductor ring. *Phys. Rev. Lett.*, 110:217001, 2013.

[104] Y-J Doh, J A van Dam, A L Roest, E P A M Bakkers, L P Kouwenhoven, and S De Franceschi. Tunable supercurrent through semiconductor nanowires. *Science*, 309:272–275, 2005.

[105] J-P Cleuziou, W Wernsdorfer, S Andergassen, S Florens, V Bouchiat, Th Ondarçuhu, and M Monthioux. Gate-tuned high frequency response of carbon nanotube Josephson junctions. *Phys. Rev. Lett.*, 99:117001, 2007.

[106] L Fu, C L Kane, and E J Mele. Topological insulators in three dimensions. *Phys. Rev. Lett.*, 98:106803, 2007.

[107] L Jiang, D Pekker, J Alicea, G Refael, Y Oreg, and F von Oppen. Unconventional Josephson signatures of Majorana bound states. *Phys. Rev. Lett.*, 107:236401, 2011.

[108] L P Rokhinson, X Liu, and J K Furdyna. The fractional ac Josephson effect in a semiconductor–superconductor nanowire as a signature of Majorana particles. *Nature Phys.*, 8:795, 2012.

[109] D M Badiane, L I Glazman, M Houzet, and J S Meyer. Ac Josephson effect in topological Josephson junctions. *Comptes Rendus Physique*, 14:840–856, 2013.

[110] V S Pribiag, A JA Beukman, F Qu, M C Cassidy, C Charpentier, W Wegscheider, and L P Kouwenhoven. Edge-mode superconductivity in a two-dimensional topological insulator. *Nature Nanotechnol.*, 10:593, 2015.

[111] J Wiedenmann, E Bocquillon, R S Deacon, S Hartinger, O Herrmann, T M Klapwijk, L Maier, C Ames, C Brüne, C Gould, et al. 4π-periodic Josephson supercurrent in HgTe-based topological Josephson junctions. *Nature Commun.*, 7:10303, 2016.

[112] P Dubos, H Courtois, B Pannetier, F K Wilhelm, A D Zaikin, and G Schön. Josephson critical current in a long mesoscopic SNS junction. *Phys. Rev. B*, 63:064502, 2001.

[113] J C Cuevas and F S Bergeret. Magnetic interference patterns and vortices in diffusive SNS junctions. *Phys. Rev. Lett.*, 99:217002, 2007.

[114] F Chiodi, M Ferrier, S Guéron, J C Cuevas, G Montambaux, F Fortuna, A Kasumov, and H Bouchiat. Geometry-related magnetic interference patterns in long SNS Josephson junctions. *Phys. Rev. B*, 86:064510, 2012.

[115] P M Echternach, M R Thoman, C M Gould, and H M Bozler. Electron-phonon scattering rates in disordered metallic films below 1 K. *Phys. Rev. B*, 46:10339, 1992.

[116] Le Calvez, K and Veyrat, L and Gay, F and Plaindoux, P and Winkelmann, C and Courtois, H and Sacépé, B. Joule overheating poisons the fractional ac Josephson effect in topological Josephson junctions. *arXiv:1803.07674*, 2018.

[117] D V Averin and K K Likharev. Coulomb blockade of single-electron tunneling, and coherent oscillations in small tunnel junctions. *Journal of Low Temperature Phys.*, 62:345–373, 1986.

[118] C W J Beenakker and A A M Staring. Theory of the thermopower of a quantum dot. *Phys. Rev. B*, 46:9667–9676, 1992.

[119] D Boese and R Fazio. Thermoelectric effects in Kondo-correlated quantum dots. *Europhys. Lett.*, 56:576, 2001.

[120] M Turek and K A Matveev. Cotunneling thermopower of single electron transistors. *Phys. Rev. B*, 65:115332, 2002.

[121] B Kubala and J König. Quantum-fluctuation effects on the thermopower of a single-electron transistor. *Phys. Rev. B*, 73:195316, 2006.

[122] M Tsaousidou and G Triberis. Thermal conductance of a weakly coupled quantum dot. *AIP Conference Proceedings*, 893:801–802, 2007.

[123] X Zianni. Coulomb oscillations in the electron thermal conductance of a dot in the linear regime. *Phys. Rev. B*, 75:045344, 2007.

[124] B Kubala, J König, and J Pekola. Violation of the Wiedemann-Franz law in a single-electron transistor. *Phys. Rev. Lett.*, 100:066801, 2008.

[125] Y I Rodionov, I S Burmistrov, and N M Chtchelkatchev. Relaxation dynamics of the electron distribution in the Coulomb-blockade problem. *Phys. Rev. B*, 82:155317, 2010.

[126] J V Koski, J T Peltonen, M Meschke, and J P Pekola. Laterally proximized aluminum tunnel junctions. *Appl. Phys. Lett.*, 98:203501, 2011.

[127] H Pothier, S Guéron, N O Birge, D Estéve, and M H Devoret. Energy distribution function of quasiparticles in mesoscopic wires. *Phys. Rev. Lett.*, 79:3490–3493, 1997.

[128] M Nahum and J M Martinis. Ultrasensitive hot electron microbolometer. *Appl. Phys. Lett.*, 63:3075–3077, 1993.

[129] A V Feshchenko, L Casparis, I M Khaymovich, D Maradan, O-P Saira, M Palma, M Meschke, J P Pekola, and D M Zumbühl. Tunnel-junction thermometry down to millikelvin temperatures. *Phys. Rev. Appl.*, 4:034001, 2015.

[130] M Nahum, T M Eiles, and J M Martinis. Electronic microrefrigerator based on a normal-insulator-superconductor tunnel junction. *Appl. Phys. Lett.*, 65:3123–3125, 1994.

[131] J T Muhonen, M Meschke, and J P Pekola. Micrometre-scale refrigerators. *Rep. Prog. Phys.*, 75:046501, 2012.

[132] J Senzier, P S Luo, and H Courtois. Combined scanning force microscopy and scanning tunneling spectroscopy of an electronic nanocircuit at very low temperature. *Appl. Phys. Lett.*, 90:043114, 2007.

[133] Quaglio, T and Dahlem, F and Martin, S and Gérardin, A and Winkelmann, C B and Courtois, H. A subKelvin scanning probe microscope for the electronic spectroscopy of an individual nano-device. *Rev. Sci. Instr.*, 83:123702, 2012.

[134] Martin, S C and Samaddar, S and Sacépé, B and Kimouche, A and Coraux, J and Fuchs, F and Grévin, B and Courtois, H and Winkelmann, C B. Disorder and screening in decoupled graphene on a metallic substrate. *Phys. Rev. B*, 91:041406(R), 2015.

[135] Samaddar, S and Yudhistira, I and Adam, S and Courtois, H and Winkelmann, C B. Charge puddles in graphene near the Dirac point. *Phys. Rev. Lett.*, 116:126804, 2016.

[136] Samaddar, S and Coraux, J and Martin, S C and Grévin, B and Courtois, H and Winkelmann, C B. Equal variations of the Fermi level and work function in graphene at the nanoscale. *Nanoscale*, 8:15162–15166, 2016.

[137] S Heike and T Hashizume. Atomic resolution noncontact atomic force/scanning tunneling microscopy using a 1 MHz quartz resonator. *Appl. Phys. Lett.*, 83:3620, 2003.

[138] T An, T Nishio, T Eguchi, M Ono, A Nomura, K Akiyama, and Y Hasegawa. Atomically resolved imaging by low-temperature frequency-modulation atomic force microscopy using a quartz length-extension resonator. *Rev. Sci. Instr.*, 79:033703, 2008.

[139] F J Giessibl, F Pielmeier, T Eguchi, T An, and Y Hasegawa. Comparison of force sensors for atomic force microscopy based on quartz tuning forks and length-extensional resonators. *Phys. Rev. B*, 84:125409, 2011.

[140] N Moussy, H Courtois, and B Pannetier. A very low temperature scanning tunneling microscope for the local spectroscopy of mesoscopic structures. *Rev. Sci. Instrum.*, 72:128–131, 2001.

[141] M Vinet, C Chapelier, and F Lefloch. Spatially resolved spectroscopy on superconducting proximity nanostructures. *Phys. Rev. B*, 63:165420, 2001.

[142] S C Martin. *Systèmes nanoélectroniques hybrides : Cartographies de la densité d'états locale.* PhD thesis, Université Joseph Fourier, 2012.

[143] Kimouche, A and Renault, O and Samaddar, S and Winkelmann, C and Courtois, H and Fruchart, O and Coraux, J. Modulating charge density and inelastic optical response in graphene by atmospheric pressure localized intercalation through wrinkles. *Carbon*, 68:73–79, 2014.

[144] Y Zhang, V W Brar, C Girit, A Zettl, and M F Crommie. Origin of spatial charge inhomogeneity in graphene. *Nature Phys.*, 5:722–726, 2009.

[145] S Adam, E H Hwang, V M Galitski, and S Das Sarma. A self-consistent theory for graphene transport. *Proc. Nat. Acad. Sci*, 104:18392–18397, 2007.

[146] A Deshpande, W Bao, F Miao, C N Lau, and B J LeRoy. Spatially resolved spectroscopy of monolayer graphene on Sio_2. *Phys. Rev. B*, 79:205411, 2009.

[147] D Gazit. Correlation between charge inhomogeneities and structure in graphene and other electronic crystalline membranes. *Phys. Rev. B*, 80:161406(R), 2009.

[148] M Gibertini, A Tomadin, F Guinea, M I Katsnelson, and M Polini. Electron-hole puddles in the absence of charged impurities. *Phys. Rev. B*, 85:201405(R), 2012.

[149] C Vo-Van, A Kimouche, A Reserbat-Plantey, O Fruchart, P Bayle-Guillemaud, N Bendiab, and J Coraux. Epitaxial graphene prepared by chemical vapor deposition on single crystal thin iridium films on sapphire. *Appl. Phys. Lett.*, 98:181903, 2011.

[150] S Jung, G M Rutter, N N Klimov, D B Newell, I Calizo, A R Hight-Walker, N B Zhitenev, and J A Stroscio. Evolution of microscopic localization in graphene in a magnetic field from scattering resonances to quantum dots. *Nature Phys.*, 7:245–251, 2011.

[151] A Luican, G Li, and E Y Andrei. Quantized landau level spectrum and its density dependence in graphene. *Phys. Rev. B*, 83:041405(R), 2011.

[152] Y Zhang, V W Brar, F Wang, C Girit, Y Yayon, M Panlasigui, A Zettl, and M F Crommie. Giant phonon-induced conductance in scanning tunnelling spectroscopy of gate-tunable graphene. *Nature Phys.*, 4:627, 2008.

[153] I Pletikosić, M Kralj, P Pervan, R Brako, J Coraux, A T Ndiaye, C Busse, and T Michely. Dirac cones and minigaps for graphene on Ir (111). *Phys. Rev. Lett.*, 102:056808, 2009.

[154] R Larciprete, S Ulstrup, P Lacovig, M Dalmiglio, M Bianchi, F Mazzola, L Hornekær, F Orlando, A Baraldi, P Hofmann, et al. Oxygen switching of the epitaxial graphene–metal interaction. *ACS Nano*, 6:9551–9558, 2012.

[155] S Das Sarma, S Adam, E H Hwang, and E Rossi. Electronic transport in two-dimensional graphene. *Rev. Mod. Phys.*, 83:407–470, 2011.

[156] E-A Kim and A H Castro Neto. Graphene as an electronic membrane. *Europhys. Lett.*, 84:57007, 2008.

[157] G Giovannetti, P A Khomyakov, G Brocks, V M Karpan, J Van den Brink, and P J Kelly. Doping graphene with metal contacts. *Phys. Rev. Lett.*, 101:026803, 2008.

[158] G M Rutter, J N Crain, N P Guisinger, T Li, P N First, and J A Stroscio. Scattering and interference in epitaxial graphene. *Science*, 317:219–222, 2007.

[159] M I Katsnelson, K S Novoselov, and A K Geim. Chiral tunnelling and the Klein paradox in graphene. *Nature Phys.*, 2:620, 2006.

[160] A H Castro Neto, F Guinea, M R Nuno Peres, K S Novoselov, and A K Geim. The electronic properties of graphene. *Rev. Mod. Phys.*, 81:109, 2009.

[161] C Hwang, D A Siegel, S-K Mo, W Regan, A Ismach, Y Zhang, A Zettl, and A Lanzara. Fermi velocity engineering in graphene by substrate modification. *Scientific Reports*, 2:590, 2012.

[162] C Faugéras, S Berciaud, P Leszczynski, Y Henni, K Nogajewski, M Orlita, T Taniguchi, K Watanabe, C Forsythe, P Kim, et al. Landau level spectroscopy of electron-electron interactions in graphene. *Phys. Rev. Lett.*, 114:126804, 2015.

[163] J Martin, N Akerman, G Ulbricht, T Lohmann, J H Smet, K von Klitzing, and A Yacoby. Observation of electron-hole puddles in graphene using a scanning single-electron transistor. *Nature Phys.*, 4:144–148, 2007.

[164] A Deshpande, W Bao, Z Zhao, C N Lau, and B J LeRoy. Imaging charge density fluctuations in graphene using Coulomb blockade spectroscopy. *Phys. Rev. B*, 83:155409, 2011.

[165] J.-H Chen, C Jang, S Adam, M S Fuhrer, E D Williams, and M Ishigami. Charged-impurity scattering in graphene. *Nature Phys.*, 4:377–381, 2008.

[166] Y-W Tan, Y Zhang, K Bolotin, Y Zhao, S Adam, E H Hwang, S Das Sarma, H L Stormer, and P Kim. Measurement of scattering rate and minimum conductivity in graphene. *Phys. Rev. Lett.*, 99:246803, 2007.

[167] K S Novoselov, A K Geim, S V Morozov, D Jiang, Y Zhang, S V Dubonos, I V Grigorieva, and A A Firsov. Electric field effect in atomically thin carbon films. *Science*, 306:666–669, 2004.

[168] S K Choudhary and A K Gupta. Effects of tip induced carrier density in local tunnel spectra of graphene. *Appl. Phys. Lett.*, 98:102109, 2011.

[169] Y Zhao, J Wyrick, F D Natterer, J F Rodriguez-Nieva, C Lewandowski, K Watanabe, T Taniguchi, L S Levitov, N B Zhitenev, and J A Stroscio. Creating and probing electron whispering-gallery modes in graphene. *Science*, 348:672–675, 2015.

[170] J Chae, S Jung, A F Young, C R Dean, L Wang, Y Gao, K Watanabe, T Taniguchi, J Hone, K L Shepard, et al. Renormalization of the graphene dispersion velocity determined from scanning tunneling spectroscopy. *Phys. Rev. Lett.*, 109:116802, 2012.

[171] R Wiesendanger. *Scanning Probe Microscopy and Spectroscopy*. Cambridge University Press, 1994. Cambridge Books Online.

[172] N W Ashcroft and N.D. Mermin. *Solid State Physics*. Saunders College, 1976.

[173] S Adam, S Jung, N N Klimov, N B Zhitenev, J A Stroscio, and M D Stiles. Mechanism for puddle formation in graphene. *Phys. Rev. B*, 84:235421, 2011.

[174] J Bardeen. Surface states and rectification at a metal semi-conductor contact. *Phys. Rev.*, 71:717, 1947.

[175] J Tersoff. Schottky barrier heights and the continuum of gap states. *Phys. Rev. Lett.*, 52:465, 1984.

[176] W Mönch. *Semiconductor Surfaces and Interfaces*. Springer, Berlin, Heidelberg, 1993.

[177] D Cahen and A Kahn. Electron energetics at surfaces and interfaces: concepts and experiments. *Advanced Materials*, 15:271–277, 2003.

[178] A Kahn. Fermi level, work function and vacuum level. *Materials Horizons*, 3:7–10, 2016.

[179] Y-J Yu, Y Zhao, S Ryu, L E Brus, K S Kim, and P Kim. Tuning the graphene work function by electric field effect. *Nano Lett.*, 9:3430–3434, 2009.

[180] H Yuan, S Chang, I Bargatin, N C Wang, D C Riley, H Wang, J W Schwede, J Provine, E Pop, Z-X Shen, et al. Engineering ultra-low work function of graphene. *Nano Lett.*, 15:6475–6480, 2015.

[181] S Sadewasser. *Kelvin Probe Force Microscopy,*. Springer, Berlin, Heidelberg, 2012.

[182] W Melitz, J Shen, A C Kummel, and S Lee. Kelvin probe force microscopy and its application. *Surface Science Reports*, 66:1–27, 2011.

[183] S-J Liang and L K Ang. Electron thermionic emission from graphene and a thermionic energy converter. *Phys. Rev. Appl.*, 3:014002, 2015.

[184] R Van Gastel et al. In situ observation of stress relaxation in epitaxial graphene. *New J. Phys.*, 11:113056, 2009.

[185] L D Landau. Zur Theorie der Energieübertragung. *Physics J. of the Soviet Union*, 2:46, 1932.

[186] C Zener. Non-adiabatic crossing of energy levels. *Proc. R. Soc. Lond. A*, 137:696–702, 1932.

[187] E C G Stückelberg. Theorie der unelastischen Stösse zwischen Atomen. *Helv. Phys. Acta*, 5:369, 1932.

[188] E Majorana. Atomi orientati in campo magnetico variabile. *Il Nuovo Cimento*, 9:43–50, 1932.

[189] S N Shevchenko, S Ashhab, and F Nori. Landau–Zener–Stückelberg interferometry. *Phys. Reports*, 492:1–30, 2010.

[190] W Wernsdorfer and R Sessoli. Quantum phase interference and parity effects in magnetic molecular clusters. *Science*, 284:133–135, 1999.

[191] Yu N Demkov and V Osherov. Stationary and nonstationary problems in quantum mechanics that can be solved by means of contour integration. *Sov. Phys. JETP*, 26:1, 1968.

[192] R C Dynes, V Narayanamurti, and J P Garno. Direct measurement of quasiparticle-lifetime broadening in a strong-coupled superconductor. *Phys. Rev. Lett.*, 41:1509–1512, 1978.

[193] J P Pekola, V F Maisi, S Kafanov, N Chekurov, A Kemppinen, Yu A Pashkin, O-P Saira, M Möttönen, and J S Tsai. Environment-assisted tunneling as an origin of the dynes density of states. *Phys. Rev. Lett.*, 105:026803, 2010.

[194] R Meservey and P M Tedrow. Spin-polarized electron tunneling. *Physics Reports*, 238:173–243, 1994.

[195] G Katsaros, P Spathis, M Stoffel, F Fournel, M Mongillo, V Bouchiat, F Lefloch, A Rastelli, O G Schmidt, and S De Franceschi. Hybrid superconductor–semiconductor devices made from self-assembled SiGe nanocrystals on silicon. *Nature Nanotechnol.*, 5:458, 2010.

[196] S Gasparinetti, K L Viisanen, O-P Saira, T Faivre, M Arzeo, M Meschke, and J P Pekola. Fast electron thermometry for ultrasensitive calorimetric detection. *Phys. Rev. Appl.*, 3:014007, 2015.

[197] J P Pekola. Towards quantum thermodynamics in electronic circuits. *Nature Phys.*, 11:118, 2015.

[198] A Bérut, A Arakelyan, A Petrosyan, S Ciliberto, R Dillenschneider, and E Lutz. Experimental verification of Landauer's principle linking information and thermodynamics. *Nature*, 483:187, 2012.

[199] J V Koski, V F Maisi, T Sagawa, and J P Pekola. Experimental observation of the role of mutual information in the nonequilibrium dynamics of a Maxwell demon. *Physical review letters*, 113:030601, 2014.

[200] K L Viisanen, S Suomela, S Gasparinetti, O-P Saira, J Ankerhold, and J P Pekola. Incomplete measurement of work in a dissipative two level system. *New J. Phys.*, 17:055014, 2015.

[201] P A Erdman, F Mazza, R Bosisio, G Benenti, R Fazio, and F Taddei. Thermoelectric properties of an interacting quantum dot based heat engine. *Phys. Rev. B*, 95:245432, 2017.

[202] M Josefsson, A Svilans, A M Burke, E A Hoffmann, S Fahlvik, C Thelander, M Leijnse, and H Linke. A quantum-dot heat engine operated close to thermodynamic efficiency limits. *arXiv preprint arXiv:1710.00742*, 2017.

[203] T A Costi and V Zlatić. Thermoelectric transport through strongly correlated quantum dots. *Phys. Rev. B*, 81:235127, 2010.

[204] R Scheibner, H Buhmann, D Reuter, M N Kiselev, and L W Molenkamp. Thermopower of a Kondo spin-correlated quantum dot. *Phys. Rev. Lett.*, 95:176602, 2005.

[205] S Rajauria, P S Luo, T Fournier, F W J Hekking, H Courtois, and B Pannetier. Electron and phonon cooling in a superconductor–normal-metal–superconductor tunnel junction. *Phys. Rev. Lett.*, 99:047004, 2007.

[206] H Courtois, S Rajauria, P Gandit, and et al. Inherent thermometry in a hybrid superconducting tunnel junction. *J. Low Temp. Phys.*, 153:325, 2008.

[207] Nguyen, H Q and Pascal, L M A and Peng, Z H and Buisson, O and Gilles, B and Winkelmann, C B and Courtois, H. Etching suspended superconducting tunnel junctions from a multilayer. *Appl. Phys. Lett.*, 100:252602, 2012.

[208] Nguyen, H Q and Aref, T and Kauppila, V J and Meschke, M and Winkelmann, C B and Courtois, H and Pekola, J P . Trapping hot quasi-particles in a high-power superconducting electronic cooler. *New Jour. Phys.*, 15:085013, 2013.

[209] Camarasa-Gomez, M and Di Marco, A and Hekking, F W J and Winkelmann, C B and Courtois, H and Giazotto, F. Superconducting cascade electron refrigerator. *Appl. Phys. Lett.*, 104:192601, 2014.

[210] Courtois, H and Hekking, F W J and Nguyen, H Q and Winkelmann, C B. Electronic coolers based on superconducting tunnel junctions: fundamentals and applications. *J. Low Temp. Phys.*, 175:799, 2014.

[211] Courtois, H and Nguyen, H Q and Winkelmann, C B and Pekola, J P. High-performance electronic cooling with superconducting tunnel junctions. *Comptes Rendus Phys.*, 17:1139, 2016.

[212] H L Edwards, Q Niu, and A L De Lozanne. A quantum-dot refrigerator. *Appl. Phys. Lett.*, 63:1815, 1993.

[213] J R Prance, C G Smith, J P Griffiths, S J Chorley, D Anderson, G A C Jones, I Farrer, and D A Ritchie. Electronic refrigeration of a two-dimensional electron gas. *Phys. Rev. Lett.*, 102:146602, 2009.

[214] V W Brar, R Decker, H-M Solowan, Y Wang, L Maserati, K T Chan, H Lee, C O Girit, A Zettl, S G Louie, et al. Gate-controlled ionization and screening of cobalt adatoms on a graphene surface. *Nature Phys.*, 7:43, 2010.

[215] A Riss, S Wickenburg, L Z Tan, H-Z Tsai, Y Kim, Ji Lu, A J Bradley, M M Ugeda, K L Meaker, K Watanabe, et al. Imaging and tuning molecular levels at the surface of a gated graphene device. *ACS Nano*, 8:5395–5401, 2014.

[216] P Schlottmann. Spatial variations of the order parameter in superconductors containing a magnetic impurity. *Phys. Rev. B*, 13:1, 1976.

[217] S Nadj-Perge, I K Drozdov, J Li, H Chen, S Jeon, J Seo, A H MacDonald, B A Bernevig, and A Yazdani. Observation of Majorana fermions in ferromagnetic atomic chains on a superconductor. *Science*, 346:602–607, 2014.

[218] R Pawlak, M Kisiel, J Klinovaja, T Meier, S Kawai, T Glatzel, D Loss, and E Meyer. Probing atomic structure and Majorana wavefunctions in mono-atomic Fe chains on superconducting Pb surface. *NPJ Quantum Information*, 2:16035, 2016.

[219] G C Ménard, S Guissart, C Brun, R T Leriche, M Trif, F Debontridder, D Demaille, D Roditchev, P Simon, and T Cren. Two-dimensional topological superconductivity in Pb/Co/Si(111). *Nature Commun.*, 8:2040, 2017.

[220] J Li, H Chen, I K Drozdov, A Yazdani, B A Bernevig, and A H MacDonald. Topological superconductivity induced by ferromagnetic metal chains. *Phys. Rev. B*, 90:235433, 2014.

[221] H-J Kwon, K Sengupta, and V M Yakovenko. Fractional ac Josephson effect in p-and d-wave superconductors. *Euro. Phys. J. B*, 37:349–361, 2004.

[222] J Šmakov, I Martin, and A V Balatsky. Josephson scanning tunneling microscopy. *Phys. Rev. B*, 64:212506, 2001.

[223] O Naaman, W Teizer, and R C Dynes. Fluctuation dominated Josephson tunneling with a scanning tunneling microscope. *Phys. Rev. Lett.*, 87:097004, 2001.

[224] M H Hamidian, S D Edkins, S H Joo, A Kostin, H Eisaki, S Uchida, M J Lawler, E-A Kim, A P Mackenzie, K Fujita, et al. Detection of a Cooper-pair density wave in $Bi_2Sr_2CaCu_2O_{8+x}$. *Nature*, 532:343, 2016.

[225] M T Randeria, B E Feldman, I K Drozdov, and A Yazdani. Scanning Josephson spectroscopy on the atomic scale. *Phys. Rev. B*, 93:161115, 2016.

[226] C R Ast, B Jäck, J Senkpiel, M Eltschka, M Etzkorn, J Ankerhold, and K Kern. Sensing the quantum limit in scanning tunnelling spectroscopy. *Nature Commun.*, 7:13009, 2016.

[227] Y M I Ivanchenko and L A Zilberman. The Josephson effect in small tunnel contacts. *Sov. Phys. JETP*, 28:113, 1969.

[228] B Jäck, J Senkpiel, M Etzkorn, J Ankerhold, C R Ast, and K Kern. Quantum brownian motion at strong dissipation probed by superconducting tunnel junctions. *Phys. Rev. Lett.*, 119:147702, 2017.

[229] L Fu and C L Kane. Superconducting proximity effect and Majorana fermions at the surface of a topological insulator. *Phys. Rev. Lett.*, 100:096407, 2008.

[230] E Bocquillon, R S Deacon, J Wiedenmann, P Leubner, T M Klapwijk, C Brüne, K Ishibashi, H Buhmann, and L W Molenkamp. Gapless Andreev bound states in the quantum spin hall insulator HgTe. *Nature Nanotechnol.*, 12:137, 2017.

[231] V Ambegaokar and A Baratoff. Tunneling between superconductors. *Phys. Rev. Lett.*, 10:486, 1963.

[232] P K Tien and J P Gordon. Multiphoton process observed in the interaction of microwave fields with the tunneling between superconductor films. *Phys. Rev.*, 129:647, 1963.

[233] M Chauvin, P Vom Stein, H Pothier, P Joyez, M E Huber, D Estève, and C Urbina. Superconducting atomic contacts under microwave irradiation. *Phys. Rev. Lett.*, 97:067006, 2006.

[234] A Roychowdhury, M Dreyer, J R Anderson, C J Lobb, and F C Wellstood. Microwave photon-assisted incoherent Cooper-pair tunneling in a Josephson STM. *Phys. Rev. Appl.*, 4:034011, 2015.

[235] D Halbertal, J Cuppens, M B Shalom, L Embon, N Shadmi, Y Anahory, H R Naren, J Sarkar, A Uri, Y Ronen, A Yacobi, and E Zeldov. Nanoscale thermal imaging of dissipation in quantum systems. *Nature*, 539:407, 2016.